

# Monte Carlo Simulation of stacked Quantum Dot Arrays

von Diplom-Physiker  
Roland Kunert  
aus Halle/Saale

der Fakultät II – Mathematik und Naturwissenschaften  
der Technischen Universität Berlin  
zur Erlangung des akademischen Grades

Doktor der Naturwissenschaften,  
Doctor rerum naturalium,

genehmigte Dissertation.

Promotionsausschuß:

Vorsitzender: Prof. Dr. C. Thomsen  
Berichter/Gutachter: Prof. Dr. E. Schöll, PhD.  
Berichter/Gutachter: Prof. Dr. S. Hess

Tag der wissenschaftlichen Aussprache: 14. Juli 2006



# Abstract

In the field of solid-state physics the research on nanostructures in general, and semi-conducting quantum dot heterostructures in particular, attracted reasonable attention in the last decades. The properties of quantum dots offer a broad field of possible applications and already led to novel opto-electronic devices. But also the investigations concerned with this topic contributed to a better understanding of important issues in fundamental research.

The challenging task of growing such structures with well defined structural properties on the atomic length scale is of great technological importance. The use of self-organization effects in the fabrication process of nanostructures turned out to be a promising concept.

This thesis aims to contribute to a better understanding of the growth properties of arrays of quantum dot stacks, which consist of several layers of self-organized semi-conducting quantum dots.

In our investigation we have applied a kinetic Monte Carlo scheme modeling the diffusion of relevant particles and incorporated self-consistently the strain which occurs due to the different lattice parameters of the source materials in the heteroepitaxial growth. Our major focus was the development of a realistic strain field model which is the main ingredient for spatial and structural properties of the simulated quantum dot arrays. In the framework of elasticity theory we derived a three-dimensional strain field taking fully into account the anisotropic material character. This computationally efficient method is capable to calculate the three-dimensional strain field of arbitrarily shaped islands.

Extensive investigations concerned with the vertical strain field propagation of various structures are carried out. They give results explaining experimentally observed features of vertically aligned quantum dots. Using the kinetic Monte Carlo routine with incorporated strain field, growth simulations were performed. The combination of both methods proved to form a powerful tool capable of giving insight in some aspects of the self-organized growth of quantum dot stacks.



# Zusammenfassung

Die wissenschaftliche Untersuchung von Nanostrukturen gewann in den letzten Jahrzehnten in vielen Fachgebieten an immenser Bedeutung. Im Bereich der Festkörperphysik erwiesen sich insbesondere sogenannte Quantenpunkte, hergestellt aus halbleitenden Heterostrukturen, als Forschungsobjekte von herausragender Wichtigkeit. Die Eigenschaften von Quantenpunkten bieten ein breites Spektrum potenzieller Anwendungen und führten bereits jetzt zu neuen opto-elektronischen Bauteilen. Die mit diesem Themengebiet zusammenhängenden experimentellen und theoretischen Untersuchungen trugen nicht zuletzt auch zu bedeutenden Erkenntnissen in der Grundlagenforschung bei.

Die Herstellung von solchen Strukturen mit der Genauigkeit auf der atomaren Längenskala ist eine große Herausforderung und von großer technologischer Bedeutung. Dabei hat sich das Ausnutzen von Selbstorganisationseffekten im Herstellungsprozeß als vielversprechender Ansatz herausgestellt.

Ziel der vorliegenden Arbeit ist es, einen Beitrag zum besseren Verständnis der Wachstumsprozesse von Quantenpunktstapeln, die sich aus mehreren Lagen selbstorganisiert gewachsener Quantenpunkte zusammensetzen, zu leisten.

In unseren Untersuchungen verwendeten wir eine kinetische Monte-Carlo-Routine, um die Diffusion relevanter Partikel zu modellieren. Das Spannungsfeld, hervorgerufen durch die unterschiedlichen Gitterkonstanten der bei der Heteroepitaxie verwendeten Ausgangsmaterialien, wurde dabei selbstkonsistent einbezogen. Unser besonderes Augenmerk galt der Entwicklung eines realistischen Modells für das Spannungsfeld, das die räumlichen und strukturellen Eigenschaften der Quantenpunkte maßgeblich beeinflusst. Im Rahmen der Elastizitätstheorie entwickelten wir ein dreidimensionales Spannungsfeldmodell, welches den anisotropen Materialcharakter vollständig einbezieht. Mit Hilfe dieser rechentechnisch äußerst effizienten Methode kann das Spannungsfeld beliebig geformter Inseln berechnet werden.

Die vertikale Ausbreitung des Spannungsfeldes zahlreicher Strukturen wurde detailliert für verschiedene Materialsysteme untersucht. Dabei konnten experimentell beobachtete Positionen vertikal korrelierter Quantenpunktsysteme erklärt werden. Mit Hilfe der kinetische Monte-Carlo-Routine unter Einbeziehung des Spannungsfeldes sind umfangreiche Wachstumssimulationen durchgeführt worden. Die Kombinationen beider Methoden erwies sich als mächtiges Werkzeug, das Einblicke in viele Aspekte des selbstorganisierten Wachstums von Quantenpunktstapeln liefert.



# Acknowledgments

The writing of a PhD thesis in general is a long term process and its completion also may be understood as the finish of a period of life. Many people have contributed in many ways to the present form of the thesis and I feel a great relieve having the possibility to express my deepest gratitude to all of them at this place. I awfully regret, however, not being able to explicitly list all the names that are worth mentioning. All persons that do not appear should be ensured that this is only due to space limitations.

First of all, it is a pleasure to thank Prof. Dr. E. Schöll not only for providing the challenging, interesting, and exciting topic of this thesis. Now I have been a member of his group for more than seven years. It was of great value to me, being guided into, and through the world of scientific research by him.

Cooperation plays a vital role in scientific research. Very fruitful and stimulating discussions with the members of the theoretical department of the Fritz-Haber-Institut are acknowledged. In particular I would like to thank Thomas Hammerschmidt, Dr. Peter Kratzer, Dr. Lorenzo Mandreoli, Prof. Dr. Jörg Neugebauer, and Dr. Evgeni Penev (in alphabetical order). The development and implementation of a complex theoretical method is arbitrarily complicated. The issue of elasticity theory, having an important, outstanding role in this thesis, at least to me was at least complex. It was of inestimable value to be able to discuss these topics with an experienced specialist: Best thanks for that to Dr. Vitali Shchukin. Furthermore I would like to thank Dr. Udo Pohl for stimulating discussions.

The connection to my friends and colleagues Dr. Christian Kristukat and Grischa Stegemann is not limited to physics only. Many years and many beers have been shared from the start of our days in Berlin and while studying physics.

For the nice and inspiring working atmosphere in the group of Prof. Dr. E. Schöll I would like to thank all the members, in particular Michael Block, Dr. Frank Elsholz, and Dr. Gerold Kiesslich. The Language support by Johanne Hizanidis and Dr. Sophie Gledhill is gratefully acknowledged. Hopefully it is not too obvious that this section was written without their help, even if the value of their work would be illustrated more vividly by that.

Also I would like to thank my son Carl Wilhelm Günther for not being upset, although I could not manage to be at home, as often as I wished to, during the last time. My wife Bettina Günther has always been at my side and gave me strong support—I am deeply grateful for that. Last, but not least I would like to express warmest thanks to my parents Dr. sc. Reinhard Kunert and Helga Kunert, I do not try to list the countless reasons.



# List of publications

Parts of this work were already published as

- M. Meixner, R. Kunert, S. Bose, E. Schöll, V. A. Shchukin, D. Bimberg, E. Penev, and P. Kratzer: “*Monte Carlo simulation of the self-organized growth of quantum dots with anisotropic surface diffusion*”. In: *Proceedings of the 25th International Conference on the Physics of Semiconductors (ICPS-25)*, Osaka 2000, ed. by N. Miura (Springer, Berlin 2001).
- M. Meixner, R. Kunert, E. Schöll, V. A. Shchukin, and D. Bimberg: “*Monte-Carlo simulation of self-organized quantum dot structures: crossover from kinetics to thermodynamics*”. In: *Proceedings of the 10th International Symposium on Nanostructures: Physics and Technology*, St. Petersburg, Ioffe Institute (2002).
- L. Mandreoli, J. Neugebauer, R. Kunert, and E. Schöll: “*Simulation of island and nanostructure growth using adatom–density kinetic Monte Carlo*”. In: *Proceedings of the 26th International Conference on the Physics of Semiconductors (ICPS-26)*, Edinburgh (2002).
- M. Meixner, R. Kunert, and E. Schöll: “*Control of strain-mediated growth kinetics of self-assembled semiconductor quantum dots*”, *Phys. Rev. B* **67**, 195301 (2003).
- L. Mandreoli, J. Neugebauer, R. Kunert, and E. Schöll: “*Adatom density kinetic Monte Carlo method: A hybrid approach to perform epitaxial growth simulations*”. *Phys. Rev. B* **68**, 155429 (2003).
- R. Wetzler, R. Kunert, A. Wacker, and E. Schöll: “*Inhomogeneous charging and screening effects in semiconductor quantum dot arrays*”. *New Journal of Physics* **6**, 81 (2004).
- M. Block, R. Kunert, E. Schöll, T. Boeck, and Th. Teubner: “*Kinetic Monte Carlo simulation of formation of microstructures in liquid droplet*”. *New Journal of Physics* **6**, 166 (2004).
- R. Kunert and E. Schöll: “*Strain-controlled correlation effects in self-assembled quantum dot stacks*”. *Appl. Phys. Lett.* (2006), (in print).

- R. Kunert, E. Schöll, T. Hammerschmidt, and P. Kratzer: *Strain field calculations of quantum dots—a comparison study of two methods*. In: *Proceedings of the 28th International Conference on the Physics of Semiconductors (ICPS-28)*, Vienna (2006), (in print).

# Preface

In the world there are several committees which every year come together to elect the *word of the year*. In 2005 in Germany the word ‘Bundeskanzlerin’ was chosen by the ‘Gesellschaft für deutsche Sprache’. In America the ‘American Dialect Society’ awarded the term ‘truthiness’. For most of the physicists the buzz word of the last decades, beyond doubt, is ‘*nano*’.

The general trend seems to be the miniaturization of all things one can think of and the reinvention of the macroscopic world on a very small scale. This manifests itself in the media, where more and more often this term appears. Often the impression arises that every scientific invention without the prefix ‘nano’ simply can not be astonishing. Shopping channels offer ‘nano-coatings’ for various purposes and even clothing made by the famous nano-technology, of course mostly of dubious value. Nevertheless this indicates that nano-technology has entered our daily lives.

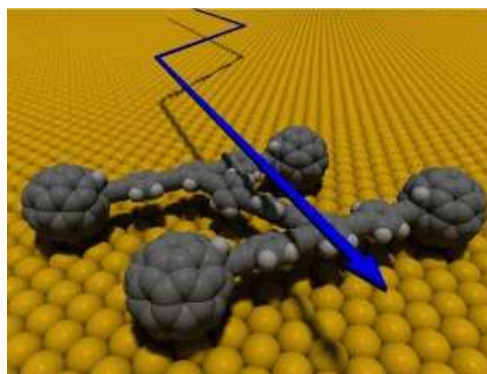


**Figure 1:** Illustration of a nanocar consisting of molecules with dimensions of  $4 \times 3$  nm [Shi05c].

Scientific researchers present activities to the audience to specifically generate media attention. This is of course necessary to promote their ideas and probably to assure the financial basis. Some of the visions sound as if they come from science fiction novels of the seventies. Examples for this include nerve cells connected to electronic devices [Fro05] or tiny self-organizing and replicating medical roboters in the bloodstream [Fre05]. To the best of the authors knowledge these roboters do not exist until now. It is possible to build gears and mechanisms on astonishing small length scales (Fig. 2). Recently Shirai *et al.* reported light driven nanocars<sup>1</sup> consisting of single molecules which measure  $4 \times 3$  nm (Fig. 1, [Shi05c]). Nanomotors have already been constructed [Reg05] and to mention only one more, a nano-sized battery for medical

---

<sup>1</sup>See also <http://www.rice.edu/media/nanocar.html>.

uses was introduced recently<sup>2</sup>. Bearing in mind all the inventions achieved already, even the previously mentioned medical roboters in the bloodstream seem to be realizable. Another aspect, which also might indicate the furious progress of this technique, is the growing concern about the risks coming with it. In *Science* the question was formulated: “Is the field moving so fast that it’s destined to repeat the mistakes of earlier technological revolutions?” [Ser04].

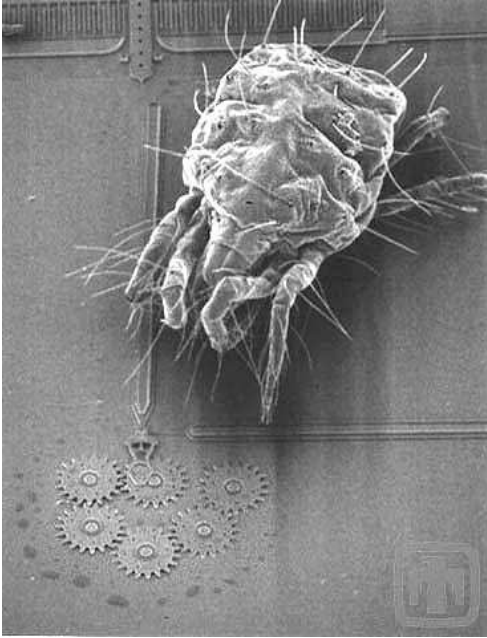


**Figure 2:** A gear chain with a mite approaching. Courtesy of Sandia National Laboratories, SUMMiTTM Technologies, <http://www.mems.sandia.gov>

Existing techniques are either not applicable on this nanometer scale or are too expensive for the industrial fabrication processes. The concept of self-organization therefore offers a chance to produce the desired structures efficiently. It has been shown that under certain conditions it is sufficient to let the ingredients simply evolve themselves, which is referred to as self-organization. Well, of course the story is a bit more complicated, as will be clear by further reading...

In this thesis the reader will find an investigation about one very specific aspect of the nano-world, which not only is about processes and effects on nano or micro scales, but also involves the challenging concept of ‘self-organization’. The focus of this work is set on the formation and growth of so-called quantum dots. These are objects consisting of only some hundreds of atoms which exhibit interesting physical properties. One of the striking features is their energy spectrum. Although they are built of many atoms, quantum dots behave as if they consist of only one single atom showing only discrete values. Many suggestions have been made for possible applications of quantum dots. The single photon detector or quantum dot lasers already exist and many more fascinating suggestions have been proposed. To realize these concepts we must be able to fabricate such tiny structures. Exist-

---

<sup>2</sup><http://sandia.gov/news-center/news-releases/2006/comp-soft-math/eye.htm>

# Contents

<b>Abstract</b>	<b>iii</b>
<b>Zusammenfassung</b>	<b>v</b>
<b>Acknowledgments</b>	<b>vii</b>
<b>List of publications</b>	<b>ix</b>
<b>Preface</b>	<b>xi</b>
<b>1 Introduction</b>	<b>1</b>
1.1 Semiconductor quantum dots . . . . .	2
1.2 Experimental methods in thin film growth . . . . .	5
1.3 Structure of this work . . . . .	6
<b>2 Growth simulations</b>	<b>9</b>
2.1 Overview . . . . .	9
2.2 Monte Carlo methods . . . . .	12
2.3 Hybrid Monte Carlo methods . . . . .	15
2.3.1 Adatom-probability kinetic Monte Carlo method . . . . .	15
2.3.2 Adatom-density kinetic Monte Carlo method . . . . .	17
2.3.3 Simulation results . . . . .	19
2.4 The kinetic Monte Carlo routine in this work . . . . .	21
2.4.1 Schwöbel barrier . . . . .	24
2.4.2 Energy intervals . . . . .	25
2.4.3 Growth parameters . . . . .	26
2.4.4 Simulation of Quantum Dot stacks . . . . .	27
2.4.5 Sensitivity of the KMC simulation . . . . .	29
<b>3 Strain field from elasticity theory</b>	<b>31</b>
3.1 Linear elasticity theory—basic equations . . . . .	31
3.2 Elastic energy of interacting inclusions . . . . .	33
3.3 Elastic energy in terms of the Green’s tensor . . . . .	37
3.3.1 The interaction term . . . . .	41

3.3.2	The originating plane: $(z_0 - z') = 0$ . . . . .	44
3.3.3	The best fitting scheme . . . . .	46
3.4	Final set of equations . . . . .	48
3.5	Isotropic approximation . . . . .	50
3.6	Summary . . . . .	53
<b>4</b>	<b>Elastic strain field of sample structures and patterns</b>	<b>55</b>
4.1	Strain field in a single layer . . . . .	55
4.2	Strain field of buried structures . . . . .	56
4.2.1	Interaction energy of single point defects . . . . .	56
4.2.2	Shape and height dependence—one single inclusion . . . . .	60
4.2.3	Periodic arrays of point-like inclusions . . . . .	64
4.2.4	Periodic arrays of islands . . . . .	69
4.2.5	Stripe shaped array of islands . . . . .	71
4.3	Summary . . . . .	72
<b>5</b>	<b>Growth kinetics of quantum dot arrays</b>	<b>75</b>
5.1	Early stages of growth . . . . .	75
5.2	Strain effects . . . . .	76
5.3	Variation of growth parameters . . . . .	78
5.3.1	Temperature and flux . . . . .	78
5.3.2	Coverage . . . . .	81
5.3.3	Growth interruption . . . . .	82
5.4	Summary . . . . .	84
<b>6</b>	<b>Growth of stacked structures</b>	<b>85</b>
6.1	Growth on prepatterned substrate . . . . .	87
6.1.1	Vertical correlated growth . . . . .	88
6.1.2	Vertical anticorrelated growth . . . . .	92
6.1.3	2D to 3D transition . . . . .	95
6.2	Growth on flat surfaces . . . . .	95
6.3	Summary . . . . .	98
<b>7</b>	<b>Conclusions and Outlook</b>	<b>103</b>
<b>A</b>	<b>Equivalence of strain field models</b>	<b>107</b>
<b>B</b>	<b>Data analysis</b>	<b>109</b>
B.1	Cross-correlation function . . . . .	109
B.2	Pairing probability . . . . .	111
<b>C</b>	<b>Numerical solution of the Green's tensor in <math>k</math>-space</b>	<b>113</b>

---

<b>D</b>	<b>Material parameters</b>	<b>117</b>
D.1	Fit parameters of strain field calculations . . . . .	117
D.2	Elastic parameters and lattice constants of selected materials . . . . .	121
<b>E</b>	<b>Event selection in the kinetic Monte Carlo routine</b>	<b>123</b>
	<b>List of Figures</b>	<b>125</b>
	<b>Bibliography</b>	<b>129</b>



# Chapter 1

## Introduction

The evolution of electronic and opto-electronic devices is not only stamped by the trend to minimize their spatial dimensions. The miniaturization, which is vividly illustrated and quantified by Moore's law, goes hand in hand with reducing the dimensions of carrier confinement. In the beginning of the last century the development started with 'normal' three-dimensional (bulk) devices. Two-dimensional electronic systems—quantum wells—became of scientific relevance in the late 1960s. In contrast to bulk properties, where Bloch's theory predicts a continuous density of states, the density of states becomes discontinuous. The carriers in these structures are no longer free and quantization effects begin to play an important role.

The investigations of quantum wells yield important novel applications and contribute to fundamental physical understanding. The first realization of semiconductor lasers, nowadays to be found in nearly every household, was based on this. As examples of success in fundamental research related to these structures, the quantum Hall effect should be mentioned. Two Nobel Prizes were connected to this topic. First, in 1985, K. von Klitzing was awarded for discovering the quantized quantum Hall effect [[Kli90](#)], and in 1998 H. L. Störmer gained the Prize for refined studies of the quantum Hall effect [[Tsu82](#); [Sto99](#)].

Another interesting application of quantum wells are tunneling diodes. They were invented by L. Esaki, another Nobel Prize winner [[Esa74](#)]. One very specific tunnel diode, the so-called 'double barrier resonant tunneling diode', which still, roughly forty years after invention of the tunnel diode, is of physical interest [[Sch01](#); [Ste06](#)].

Later on, in the 1980s research shifted its focus to the one-dimensional quantum wires. These structures in the last decades again attained much attention with the exploration of the carbon nanotube [[Rei04](#)].

The end of reducing the dimensionality finally was reached with the zero-dimensional quantum dots (QDs), which will be addressed in the following introductory section. The investigation of growth properties of QDs, as implied by its title, is the central topic of this thesis.

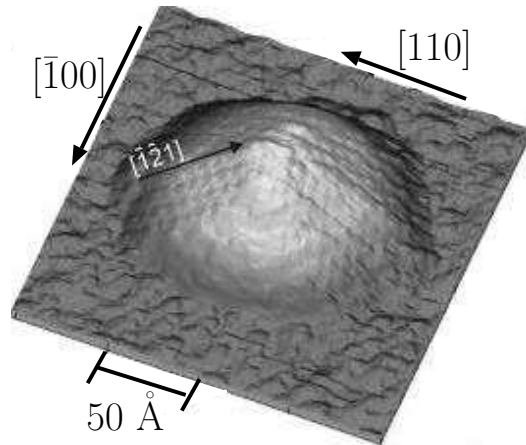


**Figure 1.1:** Three-dimensional scanning tunneling microscopy (STM) image of an uncovered InAs QD grown on GaAs(001). [Már01]

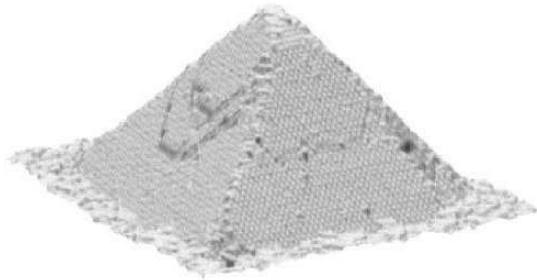


**Figure 1.2:** Scanning tunneling microscopy topograph of a Ge island during Si capping. Image scale is  $85 \times 85 \times 7 \text{ nm}^3$ . [Ras01]

## 1.1 Semiconductor quantum dots

Firstly possible applications and the practical reasons for building and studying quantum dots (QDs) should be mentioned. From the theoretician's point of view it may be reasonable to argue that zero-dimensional objects are of interest by definition. But this does not justify the broad interest in this topic. The physical properties, such as the electron confinement, and the effects coming from that are the key. Despite the fact that QDs are built of several hundreds of atoms their energy spectrum is a discrete, delta-like function. Therefore QDs are also referred to as artificial atoms. The tiny size itself gives rise to a large degree of temperature stability. Meanwhile it is possible to produce dislocation free high density QD arrays.

As one of the first applications the quantum dot laser became popular. It was experimentally realized in 1994 at the Technische Universität Berlin in collaboration with Ioffe Physico-Technical Institute St. Petersburg [Led95]. Nowadays it is found in commercial products like DVD players or the popular Playstation 3. In general QDs are proposed to have a wide range of potential applications in information and communication technology.

The quantum computer as one application, first traded as the one major goal on the road of QD development is accepted to be merely an exciting fictitious experiment and is far away from being a promising practical device [Dya02]. Instead the trend goes to

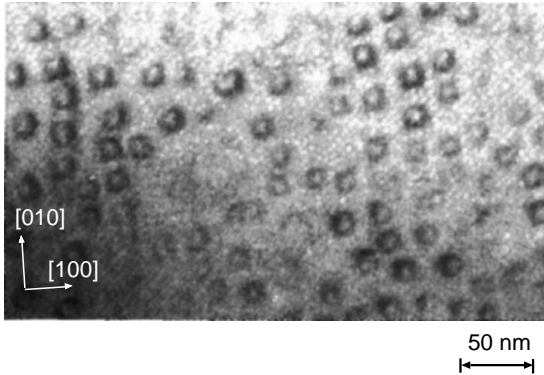


**Figure 1.3:** Plan-view transmission electron microscopy image of InAs/GaAs quantum dots. [Bim96]

the development of single photon emitters and detectors [Shi01; Yus97].

Probably the first time self-organized island formation in a semiconductor material system, namely InAs/GaAs, was observed was in 1985 by Goldstein *et al.* [Gol85]. At that time the instability causing island growth was seen as a *disturbing* factor in the preparation of quantum wells. Later in 1990 the importance of these zero-dimensional structures—the quantum dots (QD)—was realized [e.g. Mo90; Eag90].

In general in the heteroepitaxial growth of semiconductors three major growth modes may occur [Bim99; Shc04; Sta04]

- Frank-van der Merve (FvdM), also in a self-explanatory way referred to as layer-by-layer growth [Fra49],
- Volmer-Weber (VW), meaning three-dimensional island growth [Vol26], and
- Stranski-Krastanov (SK), being an intermediate growth mode, where after the formation of a two-dimensional wetting layer a transition to three-dimensional island growth occurs [Str39].

The interfacial free-energy and the lattice mismatch determines the mode in which growth will proceed. In lattice matched systems only FvdM or VW growth may occur, whereas in lattice mismatched material systems due to strain relaxations the growth in the SK growth mode is favorable [Eag90, and references therein]. Moreover the SK growth mode offers a challenging concept for producing semiconductor QDs. Since for instance with etching techniques it is not possible to manipulate atom positions on that tiny length scales necessary for QDs, the nanostructures can be fabricated ‘manually’ by setting each atom to the desired place. This can be done by scanning probe microscopy, using the tip as a write pen [Eig90]. Despite all efforts that were made to accelerate the writing speed this method remains very time consuming and therefore only of limited industrial interest. A method which is much more elegant is the *self-organized* growth of nanostructures.

The SK growth mode has been proven to provide the possibility for producing laterally ordered arrays of semiconductor quantum dots, exhibiting small size fluctuations, and high density. This method enables the fabrication of  $10^{10} - 10^{12}$  QDs per  $\text{cm}^2$  per second.

**Figure 1.4:** Cross-sectional transmission electron microscopy images of (In,Ga)As/GaAs quantum dot stack. The whole structure is shown in (a) and the initial seven periods in (b). [Ma04]

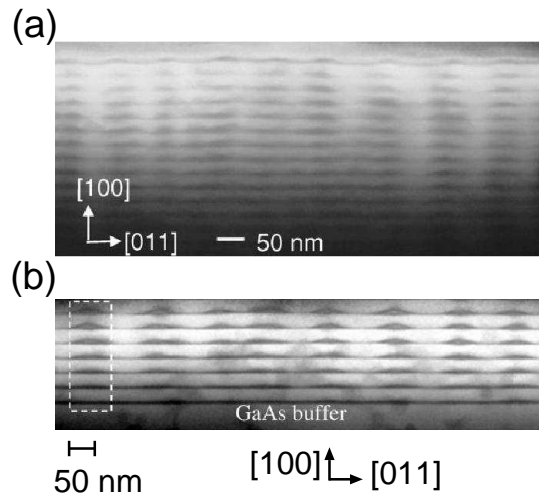
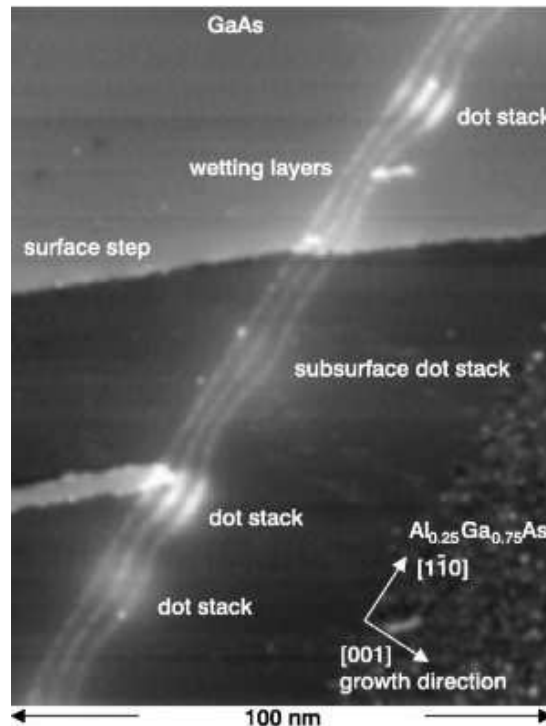


**Figure 1.5:** Overview cross-sectional scanning-tunneling microscopy image of a InAs/GaAs dot-stack layer and the surrounding buffer layers. [Fle99]



The materials selected for the preparation of QDs mainly depend on their energy gap and their lattice mismatch. To give a short, but not comprehensive, list of the most frequently used compounds: GaAs/InAs [Moi94; Hei97a], i.e., GaAs QDs on InAs substrate, GaInAs/AlGaAs [Nöt94], Ge/Si [Eag90; Abs96], SiGe/Si [Tei96], (GaSb,InSb,AlSb)/GaAs [Ben96], InP/InGaP [Kur95], or CdSe/ZnSe [Fla96] should be mentioned. Other rather ‘exotic’ material systems such as PbSe/PbEuTe [Spr00] are also studied.

The strain effects induced by the lattice mismatch, play a crucial role during

growth. They are not only responsible for selecting the desired SK growth mode. Moreover they improve (narrow down) the size distribution of the islands and can mediate an enhanced lateral ordering. Not only two-dimensional in-plane, but also vertical island correlations are attributed to strain effects. In the preparation of stacked quantum dot arrays this feature can be utilized, e.g., for achieving a desired island island distance [Spr00] or for switching between different vertical stacking modes [Wan04].

The step from one layer of quantum dot arrays to a multilayer quantum dot system indeed again seems to be an intuitive evolution. But, of course, it was not purely academic interest in stacking one thing above the other. The necessity came from the requirement of a high density of quantum dots in a given volume to improve gain and threshold of quantum dot lasers [Bim96]. In the experiments it could be observed that the growth of several quantum dot layers, one on another, has an impact on the lateral arrangement and the size distribution of the islands, both could be improved. Several reasons for this behavior are theoretically discussed, one of the main points is the influence of strain on the island positions.

From the time the topic of the self-organized growth of nanostructures moved into the spotlight of interest, a large amount of theoretical and experimental work was done and already many aspects of the growth properties of quantum dots in general, and of quantum dot stacks in particular were better understood [see e.g. Bim99; Shc04; Sta04]. This thesis aims to be a part of the theoretical contributions towards a better understanding of the properties governing the growth process of stacked quantum dot arrays.

## 1.2 Experimental methods in thin film growth

The possibility for producing and studying the samples and structures described before, having spatial dimensions in the order of the DeBroglie wavelength and smaller, was strongly related to newly developed methods of thin film growth. To give a short overview, only three popular examples of epitaxial growth techniques will be mentioned in this section briefly. Detailed information can be found elsewhere [Her04].

### Molecular Beam Epitaxy

Molecular Beam Epitaxy (MBE) offers the possibility of growing structures under well defined conditions [Fra03; Shc04]. The atomic source beams are coming from the material, which is heated in evaporation cells. Mechanical shutters can interrupt the atomic beam efficiently, such that the control of depositing less than one atomic layer is possible. Ultra High Vacuum (UHV,  $\approx 10^{-11}$  torr) conditions prevent the incorporation of impurities and ensure that atoms and molecules cover a collision free path towards the substrate. Mostly MBE systems are equipped with several in-situ

monitoring and analysis devices. This could be mass analyzer, Reflection High Energy Electron Diffraction (RHEED), Auger Electron Spectroscopy (AES) and/or others.

### **Metalorganic Chemical Vapor Deposition**

From the view point of the industrial preparation process Metalorganic Chemical Vapor Deposition (MOCVD) or Metalorganic Vapor Phase Epitaxy (MOVPE) has the advantage that the source material can be provided continuously [Moo96]. The disadvantage on the other hand are the complicated chemical processes and reactions before and during deposition in the gas phase. While UHV monitoring techniques can not be applied due to the moderate pressure used in MOVPE systems other in-situ techniques, such as reflectance anisotropy spectroscopy or spectroscopic ellipsometry [Ste96], are commonly used.

### **Liquid Phase Epitaxy**

In contrast to the previously introduced methods the growth in the Liquid Phase Epitaxy (LPE) proceeds usually at low temperatures, near thermodynamic equilibrium [Han04]. Due to the low density of point defects of the samples prepared by this technique, the epitaxial layers exhibit very good opto-electronic properties.

## **1.3 Structure of this work**

This thesis can be seen as a direct outcome and further development of the research on growth of strained semiconductor QDs in our group. Everything started in 1998, when Schöll and Bose introduced the kinetic Monte Carlo routine with a phenomenological term accounting for the strain field [Sch98b]. Within this model the formation of regular arrays of equally sized, spatially ordered quantum dots could be explained. Until now, still parts of the source code of this program, mainly the Monte Carlo simulation routine, are used.

The main focus of our research was to model the strain field, which was refined step by step. A first improvement related to that was the implementation of strain field computations coming from elasticity theory. The first approach was presented using an isotropic approximation [Kun00; Mei02a], being of course more realistic than the preceding phenomenological approach. Within this description interesting results could be achieved. The crossover from kinetically to thermodynamically controlled growth could be shown [Mei01c]. While in the first case, immediately after deposition and some time after that, the island size increases with increasing temperatures in the latter case—for longer simulation times—the opposite effect occurs. The islands grown with high temperature are smaller than the ones grown with lower temperature. Later the optimization of growth parameters such as temperature, deposition rate, coverage, and growth interruption time, and the influence of anisotropic diffusion was investigated and discussed in detail in [Mei03a].

During that time two other extensions of the model were made. Using an anisotropic strain field, the growth of dimers, trimers, and island chains along the elastically soft [100]-direction occurring in the LPE of SiGe/Si could be explained [Mei01b]. In parallel, the isotropic model was used in simulations attributed to the growth of stacked QD arrays, explaining the sharp transition from vertically correlated to anticorrelated island growth as a function of the spacer layer thickness [Mei03b].

The kinetic Monte Carlo simulation was not only used in the field of semiconductor QD growth. Other investigations in our group used this efficient tool, for example, for studying the surface roughness of different amorphous materials [Els04; Els05a] and for simulating growth processes related to LPE [Blo04].

In this thesis the kinetic Monte Carlo simulation is used as a tool for growth simulations. Simulation methods in crystal growth in general are introduced in Ch. 2. This chapter shows the advantages and disadvantages of Monte Carlo methods in the context of theoretical growth models, with an introductory section of kinetic Monte Carlo simulations in general (Sec. 2.2, p. 12) and with a detailed explanation of the routine used in this work (Sec. 2.4, p. 21).

The main ingredient as already mentioned before—the strain field—and its deviation in the framework of elasticity theory is shown in Ch. 3, pp. 31. The newly developed three-dimensional anisotropic strain field model and its deviation is discussed in detail. It offers a fast tool for calculating the elastic interaction energy of arbitrarily shaped islands, where only the material dependent elastic constants enter. The results of such calculations (shown in Ch. 4, p. 55) already can enlighten some aspects of theoretical and experimental questions, such as predictions of island positions in the growth of QD stacks (Sec. 4.2.3, p. 64).

Combining both powerful techniques: the kinetic Monte Carlo simulation (Ch. 2) and the elastic strain field (Ch. 3), gives a tool offering the possibility not only to study growth properties of one layer of QDs (Ch. 5, p. 75) but any desired number of stacked QD layers can be simulated in a self-consistent way. This is presented in Ch. 6 on pp. 85.

The appendices contain some technical material.



# Chapter 2

## Growth simulations

### 2.1 Overview

Although in the field of crystal growth computer simulations have been widely used for several decades, at the same speed as the computational power is exploding, the number of simulation methods and applications spreads [Ohn99]. A challenge to perform ‘realistic’ growth simulations is the wide range of relevant length and time scales. The features interesting for device design are of the order of  $10^2 - 10^3$  nm and the time to grow such structures is of the order of seconds. In contrast to these ranges are the scales which are necessary to resolve the microscopic origin of these effects, namely  $\approx 10^{-1}$  nm and  $\approx 10^{-13}$  s.

However, there exists a zoo of simulation methods, each limited by a certain length and time scale. Roughly one distinguishes the following three major classes

#### **Microscopic methods** ( $\approx 1 \text{ \AA}$ , $\lesssim 1 \text{ ms}$ )

This is the realm of the so called *first principles*, or *ab initio* methods, having the big advantage of not needing any a priori information.

Density Functional Theory (DFT) is a parameter free approach to describe the electronic structure of solids, not only used in the field of crystal growth. It is based on works of Walter Kohn and John Pople for which they were awarded the Noble Price in chemistry in 1998 [Koh99; Pop99]. For a nice overview and introduction in this method the reader is referred to the PhD thesis of E. Penev [Pen02], which makes use of this approach for investigations concerned with surface diffusion in the InAs/GaAs heteroepitaxy. In particular this method can be used to calculate an accurate potential energy surface (PES), giving information about pathways of single atoms, stability of certain reconstructions, and in combination with growth simulations is capable to enlighten complex growth mechanisms. Further information can be found in [Par94; Rug97; Sta05].

Molecular Dynamics (MD) provides insights into the full atomistic structure. Besides ab initio MD simulations, which usually incorporate PES calculated

with DFT, also semi-empirical methods exists. In ab initio MD simulations no *a priori* information is needed and they provide detailed insight into microscopic processes. To mention only two interesting effects which were investigated using this method, funneling [Eva90] and steering processes [Mon01] which are known to have an immense impact on surface morphology should be addressed in short. The first describes the effect of a newly arriving adatom impinging at the surface at the top or a side facet of a hill. Instead of sticking at the position where the first surface atom is met, the adatom may glide down the hill until it is adsorbed at some place, which is not necessarily the very bottom. The latter process is connected to the fact that arriving adatoms are attracted by the outermost surface atoms. Thus if the surface contains a large three-dimensional structure the way of the arriving adatom is deviated towards it. On the other hand, if there is a hole on the surface the adatoms are attracted to the sides of it and only seldom reach the bottom.

An example of an extension of this method is the so called *temperature accelerated dynamics* [Vot02], based on the idea to separate different time scales [Hen03] and under the use of heavy brute force techniques, which from the computational point of view are comparable to the famous SETI@home<sup>1</sup> or the very recent Stardust@home project<sup>2</sup>, among other interesting effects complex multi-atom diffusion mechanisms were found. However, so far it has not been possible to describe large systems consisting of  $10^4 - 10^5$  atoms.

### Mesoscopic methods ( $\approx 1$ nm, $\approx 1000$ ms)

Continuum Equations (CE) describe the surface morphology and its evolution in terms of the height profile  $h(\mathbf{r}, t)$ , which is connected to some mass flux  $\mathbf{j}(\mathbf{r}, t)$  of impinging particles on the surface by the evolution equation  $\partial_t h(\mathbf{r}, t) = \nabla \cdot \mathbf{j}(\mathbf{r}, t)$ . The current itself can be modeled in different ways, depending on the point of interest.

Important examples for CEs are Stochastic Differential Equations (SDE). In the framework of SDEs one of the first descriptions was developed by Edwards and Wilkinson [Edw82]. Taking into account a contribution coming from changes in the local chemical potential which on overall tends to smooth the surface and a second term attributed to fluctuations, the evolution of the surface height profile  $h(\mathbf{r}, t)$  is described by the linear equation

$$\partial_t h(\mathbf{r}, t) = \nu \nabla^2 h(\mathbf{r}, t) + \eta(\mathbf{r}, t), \quad (2.1)$$

<sup>1</sup><http://eon.cm.utexas.edu/>; the SETI@home project meanwhile is obsolete, it was replaced by the new Berkeley Open Infrastructure for Network Computing <http://boinc.berkeley.edu/>.

<sup>2</sup>For searching interstellar dust in the Stardust Interstellar Dust Collector (SIDS), which came back to earth in January 2006, the project Stardust@home was founded (see <http://stardustathome.ssl.berkeley.edu/background.html>).

with  $\nu$  being a positive constant referred to as surface tension and  $\eta(\mathbf{r}, t)$  denoting fluctuations, e.g., in the impinging flux, described by Gaussian white noise.

Adding a contribution  $(\nabla h)^2$  responsible for lateral growth we gain the non-linear Kardar-Parisi-Zhang (KPZ) equation [Kar86]

$$\partial_t h(\mathbf{r}, t) = \nu \nabla^2 h(\mathbf{r}, t) + \lambda (\nabla h(\mathbf{r}, t))^2 + \eta(\mathbf{r}, t). \quad (2.2)$$

Both equations are representing different descriptions of the growth process and hence different universality classes. This can be quantified by three exponents derived from scaling concepts: the growth exponent  $\beta$ , the roughness exponent  $\alpha$ , and the dynamic exponent  $z$ . For a detailed derivation and further discussion see for example [Bar95].

While CEs can be treated analytically and without large computational effort, on the other hand connecting some of the included variables directly to certain atomistic processes happens to be not quite easy. For further information the reader is referred to [Vil91; Kru93; Gyu98; Šmi99].

Kinetic Monte Carlo (KMC) simulations are able to cover experimentally relevant growth times and system sizes, while having access to the full atomistic structure. The price one has to pay for this: all relevant processes have to be known beforehand. And, of course, if the model keeps track of too much (unessential) information the advantage melts again. By slightly tuning the model it is possible to extend the KMC method into both directions: examining multi-atom interactions while restricting oneself to small time and length scales [Kra02b; Gro02]—or having the view on larger systems and longer (growth-) times and neglecting processes which are less important for explaining the investigated properties. The latter is done in this work.

Reducing the computation time in KMC simulations by using parallingizing techniques is anything but easy. Simply using as much as possible CPU's on a cluster does not help. Since with the incorporation of each additional processor an overhead of communication is necessary, the efficiency *decreases* exponentially as the number of processors increases and does strongly depend on the geometrical domain decomposition and growth parameters like the flux rate or the diffusivity of adatoms [Shi05b].

An example for a model that bridges the gap between the different categories of methods allowing fast growth simulations such as Rate Equations (see below) and CEs but using as input atomic processes such as KMC simulations is the adatom-density KMC (AD-KMC) method (see Sec. 2.3), which was suggested by Mandreoli *et al.* [Man03]. In simulations concerned with high temperature regimes close to thermodynamic equilibrium the conventional KMC method becomes numerically exceedingly expensive since the characteristic time step is that of an adatom jump. In contrast to that the characteristic time step for the

AD-KMC method is that of a growth event. Thus, particularly at high growth temperatures the number of simulation steps is reduced by orders of magnitude compared to the KMC method.

### **Macroscopic methods** ( $\approx 1$ cm, $\approx 1$ s)

One example of a macroscopic method are Rate Equations (RE), which in general can be applied to diffusion-mediated processes and are based on solving a set of coupled ordinary differential equations. Applied to crystal growth, this method is designed to give global information without spatial resolution. The differential equations in this field are solved for the island densities involving parameters like deposition rate, monomer diffusion rate and rates for the attachment (detachment) of adatoms to (from) islands. Information about the time evolution of the adatom and island densities can be deduced for large systems and long time scales [Ven84; Kru03; Mic04].

Even though it is mostly homoepitaxial processes in the submonolayer regime that are investigated [Rat94; Ama95; Vve00; Ama02], this theory also gives insights into properties of the heteroepitaxial growth [Che04; Krz02] and even of the three-dimensional heteroepitaxial growth [Cao03].

One disadvantage, however, is that at least some of the input parameters can not be directly connected to atomic processes.

## **2.2 Monte Carlo methods**

In general, Monte Carlo Methods are utilities for numerically solving various problems under the use of random numbers. It is well known that S. Ulam introduced the term ‘Monte Carlo’ named after the famous city in Monaco. It was called such because of the huge number of random number generators, i.e., the roulette tables, located there, which were ‘misused’ there for gambling. Even though this name became popular around 1944, lots of analogous methods were used a long time before. Probably one of the first problems examined with this method is the quest for the number  $\pi$  using Buffon’s needle experiment (A. Hall, 1873). Simulations of this category, in particular, are computer experiments for examining real processes, which obey random behavior and are analytically not, or only barely solvable.

Even though this method is described in a large number of textbooks [Bin79; Ohn99; New99] and some overview articles [e.g. Ala02; Fic91] a short introductory section focusing on the application in this work will be presented here.

The state of a dynamic system is described by dynamic variables. For example to describe molecules in the gas phase, the variables could be the positions and momenta. The basis of the method is now that the dynamic variables change at each time step stochastically and moreover, the system has no memory, meaning that the change is Markovian and does not depend on the history. The state at the next time step is determined via random numbers.

Having the system in the state  $\mathbf{n}$  one can define a transition probability  $p_{\mathbf{n} \rightarrow \mathbf{n}'}$  for finding the system after the time  $t$  in the state  $\mathbf{n}'$ . Transition rates  $w$  and probabilities  $p$  can be transferred via  $w_{\mathbf{n} \rightarrow \mathbf{n}'} = p_{\mathbf{n} \rightarrow \mathbf{n}'} / \tau_0$ , with  $\tau_0$  being an elementary time unit.

If we know the initial distribution, lets say  $\Omega$ , such that the process is defined that the probability distribution of state  $\mathbf{n}$  at  $t = 0$  is  $\Omega(\mathbf{n})$ , then these two ingredients already give a so called *Markov chain*. Since the process being in state  $\mathbf{n}$  should be able to generate a new state, the condition

$$\sum_{\mathbf{n}'} p_{\mathbf{n} \rightarrow \mathbf{n}'} = 1$$

has to be fulfilled, which does not exclude self-scattering.

Defining the weight  $P_{\mathbf{n}}(t)$  representing the probability that the process is in the state  $\mathbf{n}$  at time  $t$  we are able to describe the time evolution of the process with the following *Master equation*

$$\partial_t P_{\mathbf{n}}(t) = \sum_{\mathbf{n}'} P_{\mathbf{n}'}(t) w_{\mathbf{n}' \rightarrow \mathbf{n}} - P_{\mathbf{n}}(t) w_{\mathbf{n} \rightarrow \mathbf{n}'} . \quad (2.3)$$

An detailed example on how to deal with the above given Eq. (2.3) is given in the next section (Sec. 2.3).

To ensure that the process indeed tends to equilibrium *detailed balance*

$$P_{\mathbf{n}} p_{\mathbf{n} \rightarrow \mathbf{n}'} = P_{\mathbf{n}'} p_{\mathbf{n}' \rightarrow \mathbf{n}} \quad (2.4)$$

is required. This is a sufficient but not necessary condition and does not determine the transition rates uniquely.

The next requirement for Monte Carlo algorithms is *ergodicity*. This means, from every state  $\mathbf{n}$  every other state  $\mathbf{n}'$  is reachable via a Markov chain (nothing is being said about the time needed for this, so this probably could take a really long time).

Having in mind the previous constraints one can go on and construct transition probabilities, which give Markov chains.

The two most famous choices are

### Metropolis algorithm

$$p_{\mathbf{n} \rightarrow \mathbf{n}'} = \begin{cases} 1 & \text{if } E(\mathbf{n}') - E(\mathbf{n}) < 0 \\ \exp(-\beta(E(\mathbf{n}') - E(\mathbf{n}))) & \text{otherwise} \end{cases}$$

### Kawasaki algorithm

$$p_{\mathbf{n} \rightarrow \mathbf{n}'} = \frac{1}{1 + \exp(\beta(E(\mathbf{n}') - E(\mathbf{n})))} ,$$

with  $\beta = 1/(k_B T)$  where  $k_B$  is Boltzmann's constant and  $T$  the temperature.

In the simplest form of a Monte Carlo algorithm for simulating lattice dynamics, a particle is chosen randomly and a jump direction is chosen randomly again. If the arrival site is empty the probability  $p_{\mathbf{n} \rightarrow \mathbf{n}'}$  is computed and compared with a random number  $0 < r_{\text{rand}} \leq 1$ . In the case that the final site is occupied or  $r_{\text{rand}} > p_{\mathbf{n} \rightarrow \mathbf{n}'}$  the move is rejected. Now, the described cycle starts from the beginning.

The essential drawback is clear. There is always a certain number of cycles which do not produce new states since they are rejected, yet consume computing time. In low temperature systems, where transition probabilities are low too, this effect becomes dominant.

To overcome this problem, an event (transition) should be chosen according to its *a priori* probability, and *every* step should be accepted. Methods based on this idea are so-called *time dependent* Monte Carlo methods (as the method used in this work), sometimes referred to as *event based* Monte Carlo, *continuous time* Monte Carlo or *BKL algorithm* after Bortz, Kalos and Lebowitz [Bor75].

Consider a system with a total number of states of  $N$  being in the state  $\mathbf{n}$ . Labeling all states  $\mathbf{n}'$  which may be reached from  $\mathbf{n}$  with  $k \in \{1, \dots, K\}$ , then the total transition rate is given by

$$W(\mathbf{n}) = \sum_{\mathbf{n}'} w_{\mathbf{n} \rightarrow \mathbf{n}'} = \sum_{k=1}^K w(\mathbf{n}; k).$$

Here, the rate  $w_{\mathbf{n} \rightarrow \mathbf{n}'}$  to the final state  $\mathbf{n}'$  being labeled by the number  $k$  is described by  $w(\mathbf{n}; k)$ . The partial sums can be written as

$$W(\mathbf{n}; k) = \sum_{l=1}^k w(\mathbf{n}; l).$$

Now one specific event  $k$  can be selected by a uniformly distributed random number  $0 < \tilde{r}_{\text{rand}} \leq W(\mathbf{n})$ , for which the condition

$$W(\mathbf{n}; (k-1)) < \tilde{r}_{\text{rand}} \leq W(\mathbf{n}; k) \quad (2.5)$$

must be met. Under the constraint that the time is incremented proportional to the lifetime  $\tau(\mathbf{n}) = \tau_0/W(\mathbf{n})$ , detailed balance is ensured always. And therefore one can model the transition probabilities with respect to the physical needs of the specific problem rather than being restricted to the constraints mentioned above.

The time step  $\Delta t$  in the event based Monte Carlo simulation is calculated as follows [Fig91]: it can be shown that the mean time step is connected to the inverse of the transition probabilities  $p_i$  via a uniform random number by

$$\langle t \rangle = -\frac{\langle r_{\text{rand}} \rangle}{p_i} = -\frac{\int_0^1 \ln r_{\text{rand}} dr_{\text{rand}}}{p_i} = \frac{1}{p_i}. \quad (2.6)$$

Treating the processes quasi-simultaneously and assuming their independence from each other the sum of all processes enters as

$$\Delta t = \frac{1}{\sum_i p_i}. \quad (2.7)$$

Now instead of wasting computation time for unnecessary rejections, which do not contribute to a change of the configuration, the main part of computing time is spent for calculating total and partial transition rates. However, implementing the time-dependent Monte Carlo algorithm thoughtfully, under the use of some computational tricks, e.g., the incorporation of some very well organized lists, this effect can be minimized and this method is much faster.

Finally, as a last comment of this section the difference of kinetic Monte Carlo (KMC) to classical Monte Carlo should be underlined. While the latter is used for the calculation of a quantity in the thermodynamical equilibrium state of the system the first describes a *path* of the system towards the equilibrium state.

## 2.3 Hybrid Monte Carlo methods

To bridge the gap between the length and time scales of Monte Carlo methods and macroscopic methods using densities a number of hybrid methods have been proposed. Here we review a particularly efficient method for simulating growth processes suggested by Mandreoli *et al.* [Man03].

### 2.3.1 Adatom-probability kinetic Monte Carlo method

For the evaluation it is necessary to solve the master equation (Eq. (2.3)), aiming first to separate the fast from the slow processes. These are diffusion and attachment/detachment events. Instead of following the trajectory of each individual adatom rather the probability  $\rho_\alpha(i, t)$  for finding the adatom  $\alpha$  at the site  $i$  at the time  $t$  will be calculated, yielding a method referred to as adatom-probability KMC (AP-KMC). Later on, the computational efficiency is further increased by taking into account only the *total* adatom density  $\rho(i, t) = \sum_\alpha \rho_\alpha(i, t)$ , which gives a method we will call adatom-density KMC (AD-KMC).

First, the configuration  $\mathbf{n}$  is separated into a part denoting the surface morphology  $S$  and a second part describing the positions of the  $N$  adatoms  $(i_1, i_2, \dots, i_N)$ . The probability function therefore splits into a part  $P_{ad}$ , including fast events related to the adatom positions, and another part  $P_S$  dedicated to the slow events

$$P_n(t) = P_{ad}(i_1, i_2, \dots, i_N, t) P_S. \quad (2.8)$$

Since on a typical time scale for growth  $\Delta t_{\text{growth}}$  the surface does not change we set  $P_S = 1$  and, under the condition of non-interacting adatoms, can factorize the probability function

$$P_n \rightarrow P^{\text{nonint}}(i_1, i_2, \dots, i_N, t) = \rho_1(i_1, t) \rho_2(i_2, t) \cdots \rho_N(i_N, t), \quad (2.9)$$

such that the master equation decomposes into a set of single adatom equations

$$\partial_t \rho_\alpha(i, t) = \sum_{\delta} [w_{(i+\delta) \rightarrow i} \rho_\alpha(i + \delta, t) - w_{i \rightarrow (i+\delta)} \rho_\alpha(i, t)], \quad (2.10)$$

with  $\delta$  being an index for all neighboring sites. The time evolution of each single adatom probability can be calculated using the following rules

- (1)  $\partial_t \rho_\alpha(i, t) = 0$  before adsorption of adatom  $\alpha$  at time  $t_\alpha^{\text{des}}$
- (2)  $\partial_t \rho_\alpha(i, t_\alpha^{\text{ads}}) = \delta_{i, i_{\text{ads}}}$  with  $\delta$  being the Kronecker symbol and  $i_{\text{ads}}$  the adsorption site.
- (3) it is computed by Eq. (2.10)
- (4)  $\partial_t \rho_\alpha(i, t) = 0$  after desorption or attachment

With the deterministic choice of the adsorption time  $t_\alpha^{\text{des}} = \alpha \Delta t_{\text{growth}}$  where  $\Delta t_{\text{growth}} = 1/L^2 F$ , the total number of adsorption sites is  $L^2$  and  $F$  the flux of the impinging particles, all ingredients for the method are given. The solution of Eq. (2.10) can be obtained by applying the finite difference scheme

$$\partial_t \rho_\alpha(i, t) = \frac{\rho_\alpha(i, t + \Delta t) - \rho_\alpha(i, t)}{\Delta t} \quad (2.11)$$

with the choice of  $\Delta t = \Delta t_{\text{growth}}$ .

To evaluate the detailed position of an adatom the single-particle density has to be collapsed on a single site. This is done similarly to the event selection of a KMC described by Eq. (2.5) by choosing a random number  $r_{\text{rand}} \in [0, 1]$  and selecting a site  $l \in [0, L^2]$  such that

$$\sum_{i=0}^l \rho_\alpha(i, t) \leq r_{\text{rand}} \leq \sum_{i=0}^{l+1} \rho_\alpha(i, t) \quad (2.12)$$

is fulfilled. Note that  $\sum_{i=0}^{L^2} \rho_\alpha(i, t) = 1$ .

As one example for the computational efficiency Fig. 2.1 shows an adatom approaching a step edge. Already after *three* collapses/simulation steps each with  $\Delta t = 0.01$  s the adatom attaches to the step. In contrast to that, standard KMC following the trajectory in detail would need a number of simulation steps being orders of magnitude larger, in this particular case in the KMC approach approximately 800 adatom jumps would be carried out.

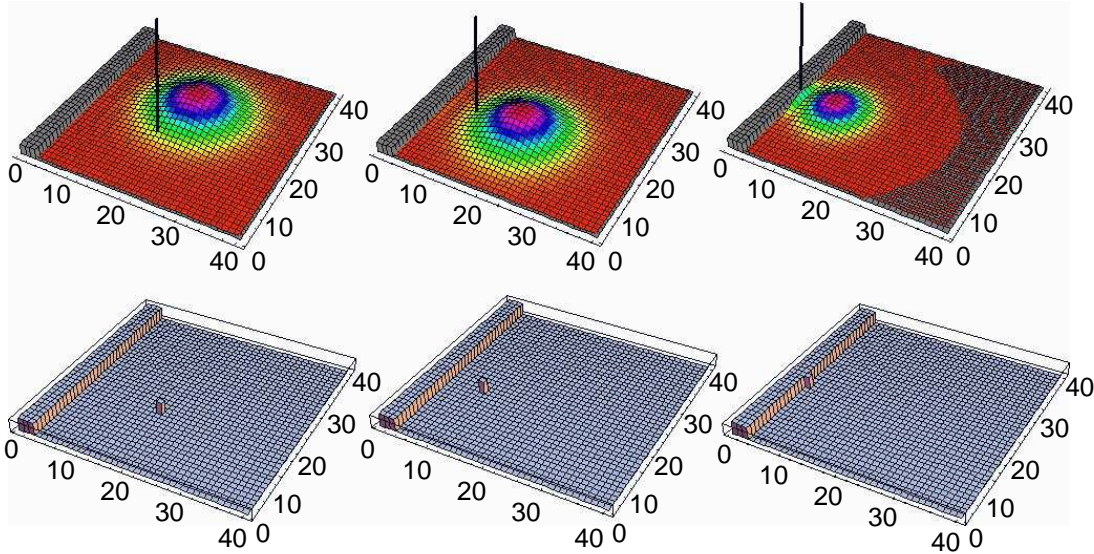


**Figure 2.1:** Adatom-probability-KMC method. Surface before (top panel) and after (lower panel) a collapse of the adatom density. The collapse is performed at equal time intervals of  $\Delta t = 0.01$  s. The simulation has been performed at a temperature of  $T = 500$  K. The adatom density has been scaled for ease of viewing. [Man03]

The inclusion of adatom-adatom interaction can be derived straightforward from Eq. (2.10). Since it does not offer new insights we will not discuss it here. While the fast and slow time scales already are decoupled, still numerically expensive computations have to be carried out. These are the calculation of the single-particle density and the nucleation probability. The latter is a two-particle density and scales thus with the square of the total number of adatoms.

### 2.3.2 Adatom-density kinetic Monte Carlo method

In order to discuss further optimizations let us consider the case of high growth temperatures, which is particularly relevant for realistic growth simulations. Since the diffusivity (the jump probability) of an adatom increases exponentially with temperature at high temperatures an adatom quickly explores a large part of the surface and gets quickly trapped on energetically favorable sites (such as surface steps or kinks). Under these conditions the total adatom density and thus the nucleation rate will be small. In other words, the one particle density will be rather delocalized and will quickly “lose” the information about the initial adsorption site. In the limit of infinite diffusivity each adatom can explore the entire surface, i.e., the single particle density will be infinite and describe the *thermodynamic* probability to find an adatom on a certain site. This probability function is of course identical for all adatoms. For conditions close to thermodynamic equilibrium the densities are not identical but similar.

If the one particle densities are (at least in a local region) similar to each other and largely delocalized the adatoms can be described by the *total adatom density*

$$\rho(i, t) = \sum_{\alpha} \rho_{\alpha}(i, t) \quad (2.13)$$

rather than by the complete set of single particle densities. Therefore the method will be referred to as adatom-density KMC (AD-KMC). Assuming aggregated growth, meaning once an adatom has been incorporated it becomes and remains immobile, the time evolution is described by

$$\begin{aligned} \partial_t \rho(i, t) = & \sum_{\delta} [w_{(i+\delta) \rightarrow i} \rho(i + \delta, t) - w_{i \rightarrow (i+\delta)} \rho(i, t)] - \\ & n_{\text{nuc}}(i, t) - n_{\text{att}}(i, t) + F(i, t), \end{aligned} \quad (2.14)$$

an equation similar to Eq. (2.10), except that nucleation  $n_{\text{nuc}}(i, t)$ , attachment  $n_{\text{att}}(i, t)$  and homogeneous adsorption  $F(i, t) = F$  are explicitly included. Attachment is described by a deterministic event, i.e., it occurs once the adatom density at site  $i_0$  and at time  $t_0$  is unity ( $\rho(i_0, t_0) = 1$ ). If such an event occurs,  $n_{\text{att}}(i, t) = \delta_{i, i_0} \delta_{t, t_0}$ , i.e., the density on this site is reset to zero. Also, the surface and thus the transition probabilities  $w_{(i+\delta) \rightarrow i}$  around the attached atom are modified:

$$S = (\dots h_i \dots) \Rightarrow S' = (\dots h_i + 1 \dots). \quad (2.15)$$

On a free terrace all transition rates are identical and given by the surface diffusion constant  $D$  by

$$w_{i+(\delta_i) \rightarrow i} = D/l_0^2. \quad (2.16)$$

Here,  $l_0$  is the distance between two nearest neighbor sites. If we further assume that the adatom density around the nucleation site is approximately constant, we get the probability that a nucleation event takes place on site  $i$  at time  $t$  as

$$p_{\text{nuc}}(i, t) \approx D l_0^2 \rho^2(i, t), \quad (2.17)$$

which is a well known relation often applied in rate equations [Pim98]. To calculate the nucleation rate  $n_{\text{nuc}}(i, t)$  needed to solve Eq. (2.14) we assume

$$n_{\text{nuc}}(i, t) \equiv \bar{p}_{\text{nuc}}(t) = \int_{t-\Delta t_{\text{growth}}}^t \sum_i p_{\text{nuc}}(i, t) dt. \quad (2.18)$$

The replacement of a localized nucleation term by a delocalized term is well justified for the high temperature conditions assumed here and avoids the formation of localized regions with negative adatom density. For the modification of the surface and the transition states the non-averaged nucleation term according to Eq. (2.17) is used. As can be seen from the above equations all quantities entering Eq. (2.14) are either explicitly given (like the flux  $F$ ) or can be directly calculated from the total adatom

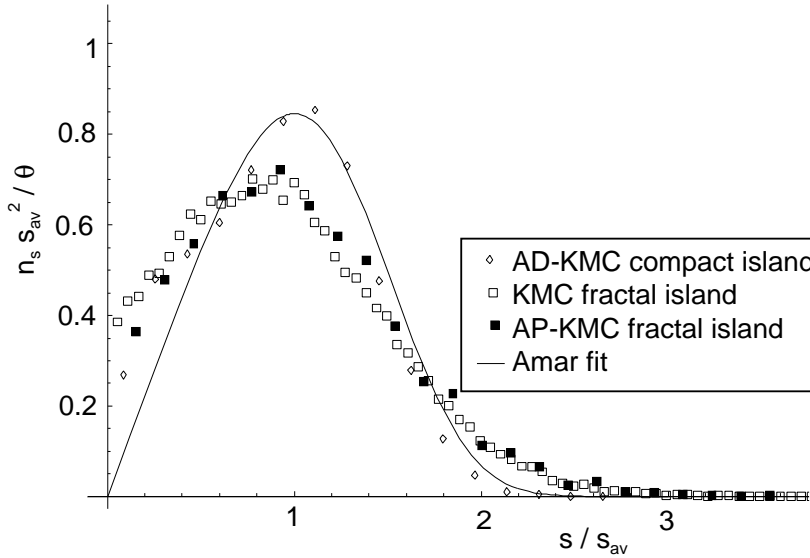


**Figure 2.2:** Island size distribution as obtained by KMC (empty squares), AP-KMC (filled squares) and AD-KMC (diamonds) for  $T = 630$  K and a ratio  $D/F = 10^6$ . The solid line is the universal scaling relation, as given in Ref. [Ama95].  $n_s$  is the density of islands of the size  $s$ ,  $s_{av}$  the average island size and  $\theta$  is the fractal coverage. [Man03]

density  $\rho(i, t)$ . Thus, in contrast to AP-KMC the explicit calculation of single particle densities and two particle nucleation terms is avoided making AD-KMC computationally much more efficient. Only for high temperature we expect the number of adatoms on the surface to be low, so the number of equations to solve (one for each adatom) will be small and AP-KMC can be almost as fast as AD-KMC.

### 2.3.3 Simulation results

To check the validity of the single and total adatom density based approaches we performed an extensive comparison with KMC. For all three approaches identical simulation parameters have been chosen. The simulations have been performed on a square lattice (mesh size  $80 \times 80$ ), and the transition rates are calculated according to the procedure described in detail later (Sec. 2.4) with energies of  $E_S = E_b = 1.0$  eV. The coupling between adjacent sites is neglected ( $c = 0$ ). The flux of incoming adatoms is  $F = 1$  Monolayer (ML)/s. The total simulation time is 0.1 s, i.e., a total of 0.1 ML is deposited on the surface. Further it is assumed that already a dimer forms a stable nucleus. This is explicitly enforced in the KMC calculations and allows to approximate the nucleation in AD-KMC by Eq. (2.17). The growth temperature has been varied over a large range of temperatures (from 500 to 1000 K). In order to analyze the results various statistical quantities such as island nucleation density, island size dis-

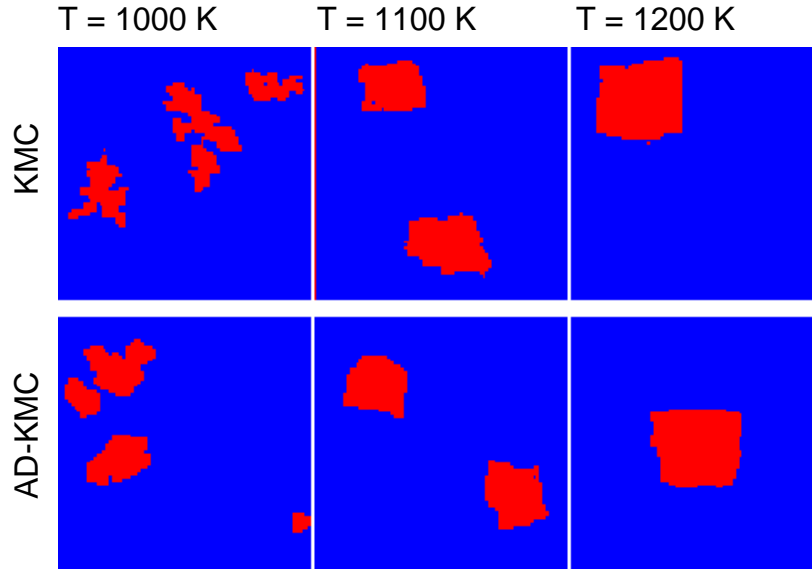


**Figure 2.3:** Comparison of the island shape in KMC (top panel) and AD-KMC (lower panel) simulations for temperatures  $T$  ranging from 1000 K to 1200 K. Simulations have been performed on a  $80 \times 80$  matrix. [Man03]

tribution and island shape were calculated and compared. However, here only a subset of the results which are shown in [Man03] are discussed.

One measure giving access to the spatial information is the island size distribution. Previous studies [Bar95] addressing this quantity showed that over a large range of fluxes, temperature, and diffusion barriers the island size distribution approximately follows a universal scaling law [Ama95].

Fig. 2.2 shows the island size distribution for all three approaches: AD-KMC, AP-KMC and the KMC method. A total of 45 runs on a  $300 \times 300$  matrix has been performed to obtain a reliable statistics. As can be seen the island size distribution as calculated by KMC and AP-KMC are identical within the statistical error bars. However, AD-KMC exhibits rather large deviations. The maximum is larger and shifted towards larger island sizes. Also, the distribution function is narrower than for KMC and AP-KMC. An interesting behavior is that the universal scaling law [Ama95] describes the KMC and AP-KMC results only rather poorly, indicating the limits of this model. Interestingly, however, it correctly reproduces the AD-KMC results.

It turns out that the island morphology is responsible for that behavior (not shown). KMC and AP-KMC exhibit fractal growth, indicating that the flux ratio chosen here corresponds to rather low temperatures. AD-KMC shows a very different shape, islands are not fractal but more compact. The obvious failing of AD-KMC is related to the fact that to derive this scheme we assumed that the system is close to thermodynamic equilibrium, i.e., temperatures are high enough to realize delocalized adatom densities. Based on the discrepancy in the island size distribution, and also in the island

shapes the temperature chosen here is much too low.

To focus on a comparison of the different growth simulations at high temperatures Fig. 2.3 shows characteristic surfaces as obtained from KMC and AD-KMC simulations for temperatures between 1000 and 1200 K. For temperatures above 1100 K the agreement is excellent: Both methods show compact islands with similar features such as density of kinks. Also, both methods show that with increasing temperature the deviations from the equilibrium shape (which is a square for the parameters and lattice chosen here) become smaller. Only for the lowest temperature, where KMC shows the formation of fractal like structures AD-KMC gives too compact islands as already found for the low temperature case.

We can therefore conclude that for high temperatures (where KMC becomes exceedingly expensive) AD-KMC is an efficient and accurate tool. For conditions far away from thermodynamic equilibrium (fractal growth) the adatom density for each adatom AP-KMC has to be calculated. From a numerical point of view the density-based approach has a number of advantages. Numerically, the main effort is in solving a diffusion equation, which has been extensively studied and for which efficient tools exist, e.g., multigrid schemes [Pre92]. Also in contrast to the KMC method where domain decomposition poses a severe problem for parallelization, the latter is straightforward for a diffusion problem.

## 2.4 The kinetic Monte Carlo routine in this work

The aim of this work is modeling epitaxial crystal growth. Processes like desorption and bulk diffusion, which are not likely to occur, are not included. Therefore the dynamics is governed by two processes only:

**Deposition events** which have a given probability, directly connected to physically accessible parameters. Strictly speaking, having an experiment, e.g., with a flux rate of 0.01 ML/s and a system size of  $100 \times 100$  atoms, then every 1/100 second an adatom will be deposited randomly onto the surface.

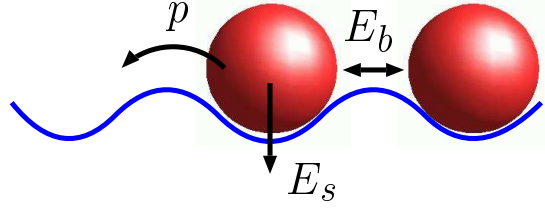
**Surface diffusion events** are modeled via an Arrhenius factor, described in more detail below.

The Arrhenius rate in general reads

$$p = \nu_0 \exp\left(-\frac{E}{k_B T}\right), \quad (2.19)$$

with  $\nu_0$  being the attempt frequency,  $k_B$  Boltzmann's constant,  $T$  the temperature and  $E$  the total energy consisting of several contributions. A choice for the attempt frequency which includes the temperature dependence is  $\nu_0 = 2k_B T/h$ , with  $h$  being Planck's constant [Šmi93]. Using this expression leads to values of  $\nu_0 \approx 3 \times 10^{13} \text{ s}^{-1}$  with temperatures of about 700 K. Here, however, the temperature dependence of  $\nu_0$

**Figure 2.4:** Illustration of the binding energies in the kinetic Monte Carlo (KMC) simulation.



is neglected [Boi98] and a value of  $\nu_0 = 10^{13} \text{ s}^{-1}$ , typical for describing group III diffusion processes [e.g. Gro02; Lar04], is used in this work [Kra99; Kle97]. The idea to model activated diffusion by Eq. (2.19) is rather old and comes from arguments of the transition state theory [Hän90].

The energy contributions come from the binding energy  $E_s$  of the adatom to the surface and the binding energies to the neighboring atoms  $E_n$ . The strength of a single nearest neighbor bond is chosen to be  $E_b$ . To evaluate the diffusion barrier, both, the binding energies at the initial and the final site of the adatom are calculated in dependence of the number of nearest neighbors  $n \leq 4$  and  $n'$  respectively. Describing the coupling to final sites with a coupling constant  $c_f = 0.2$  the total binding energy can be expressed as  $E_n = (n - c_f n')E_b$ . Now the total energy as used in Eq. (2.19) reads

$$E = E_s + E_n - E_{str} , \quad (2.20)$$

with  $E_{str}$  being an additional (strain-) energy, which is needed since in this work we are aiming to model heteroepitaxial growth. In particular we focus to the widely used InAs/GaAs material system. The lattice mismatch between InAs and GaAs of 7% leads to a strain field coming from the islands on the surface. An intuitive explanation is that the (InAs) adatoms are hindered to sit on their favorite positions, instead of their natural distance they are forced to find a position in a compressed lattice due to the influence of the underlying GaAs (Fig. 2.5). This is true only for the two-dimensional growth. Later, while studying stacked QD structures also the opposite case, where the adatoms move under the influence of a stretched lattice constant (tensile strain) plays a crucial role. During growth, however, strain relaxation mechanisms are responsible for the growth mode of the system—first a wetting layer up to a critical thickness is formed and after that a transition from the two-dimensional layer growth towards the three-dimensional islands growth occurs. This growth mode is referred to as Stranski-Krastanov (SK) growth mode. Details of the calculation of this contribution are to be found in Ch. 3.

Taking into account the flux  $F$  in monolayer (ML) per second of particles impinging onto the surface of the size  $L_x \times L_y$  (in dimensionless units, i.e., the number of grid points) the time step  $\Delta t$  of Eq. (2.7) becomes

$$\Delta t = \frac{1}{\sum_i p_i + L_x L_y F} . \quad (2.21)$$

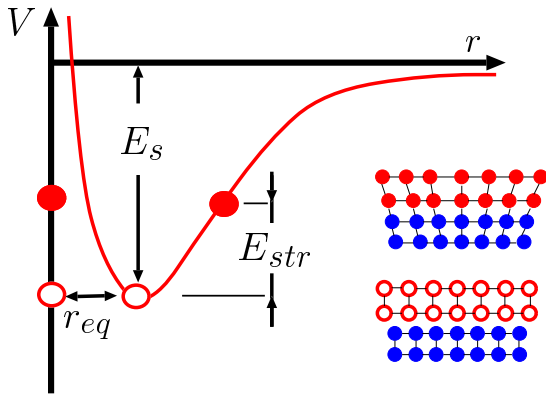


**Figure 2.5:** Illustration of the effect of compressive strain on the equilibrium distance  $r_{eq}$  of the adatoms (red) in heteroepitaxial systems with different lattice constant.

For the binding energy to the surface and the energy of one neighbor bond, here we use the following values which are typical for a variety of semiconducting materials:  $E_s = 1.3$  eV,  $E_b = 0.3$  eV. (A complete list of all relevant simulation parameters follows in Tab. 2.1, p. 27.)

The choice of the values for the energies is not easy. For simplicity we simulate effective atoms (in particular InAs atoms) which do not exist in reality, so strictly speaking energies which are needed as input parameter for the simulation routine also do not exist in reality. One of the rare articles which directly connect experimental observations with numerical experiments to clarify this question was published by Shitara *et al.* [Shi92]. The material system examined there is homoepitaxial grown GaAs. Shitara *et al.* propose values of  $E_s = 1.58$  eV and  $E_b = 0.2$  eV. This, and the whole range of other publications [e.g. Rat94; Hey01], which are using similar binding energies and come to results which have good agreement to experiments, justifies the use of the above energy values.

As mesh for our simulations we use a simple cubic lattice structure within the so-called solid-on-solid (SOS) model (Fig. 2.6). Periodic boundary conditions are applied in both lateral directions. Voids and overhangs are not allowed.

It should be noted that dealing with effective atoms hopping on a square lattice and the usage of effective energies has to be understood as a mean-field approach. Implicitly properties which lead to local fluctuations of the binding energies, are taken into account. Such properties are for example the surface reconstruction and/or changes in the As/Ga ratio, which might occur in both, time and space. As long as these fluctuations are small compared to the time scale of the fastest process modeled explicitly, there is no influence to the validity of our model to be expected.

Two further simplifications are used in the KMC simulations. Firstly evaporation events are not included. Adatoms which are deposited on the surface remain there. This treatment is justified since we assume the flux  $F$  to be an effective net flux including both processes, attachment and detachment. While working at comparatively low temperatures we can assume the error to be sufficiently small. Further we assume that adatoms having four next neighbors are immobile. This seems a reasonable assump-

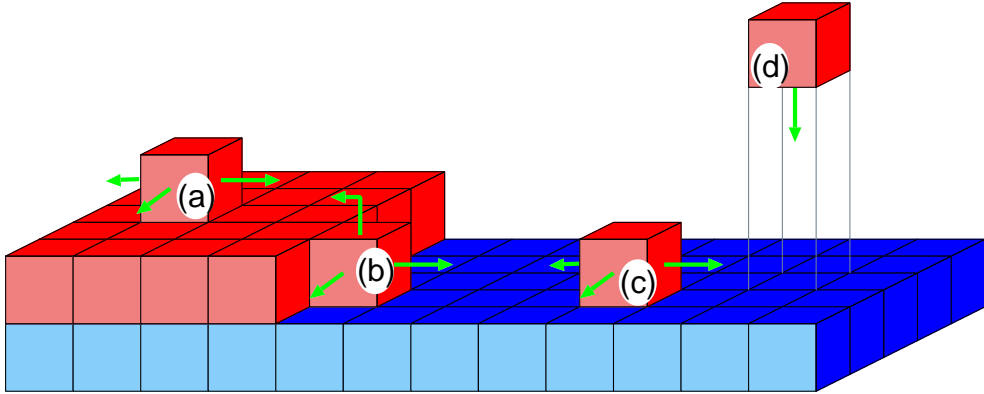
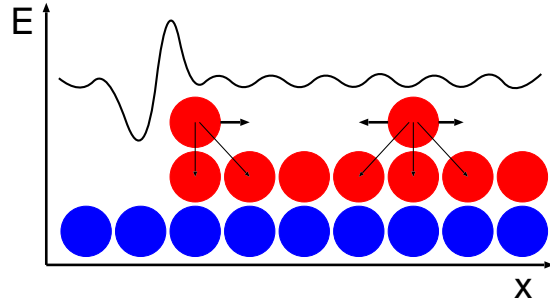


**Figure 2.6:** Illustration of the solid-on-solid model. Several situations are depicted: Adatoms may freely move in all four directions to nearest neighbor positions (a, c), the movement along an island boundary, a jump on the island, and detachment from the island is shown in (b) and the deposition of an adatom is shown in (d).

**Figure 2.7:** Illustration of the Schwöbel barrier. Adatoms at an island edge experience an additional energy barrier due to asymmetric bonds.



tion since detailed investigations of this setting have shown that this simplification does not have any impact, neither on the island morphology nor on other simulation results. Moreover it speeds up the computation time by a factor of about two—an argument strongly supporting this choice. It should be noted that due to both simplifications the ergodicity in the Markov condition (Sec. 2.2) is not completely fulfilled. This can be interpreted as a perturbation of the system path towards equilibrium. Instead of reaching a global equilibrium state connected to a global energy minimum, which would be given by a flat surface, the system tends to a local minimum state only. As a reasonable assumption it is expected that both paths (the perturbed one and the non-perturbed) and both states are close to each other in the configurational space and the main features of a growing surface are described in an appropriate manner still with both of them.

### 2.4.1 Schwöbel barrier

Besides the motion of adatoms on the flat surface other events might occur where the adatoms jump from one layer to another, e.g., from top of an island or terrace down or vice versa. In such cases an additional energy barrier comes into the play. Due to

the asymmetric bonds (see Fig. 2.7), not only the jump on top of an island is hindered, but also adatoms landed on islands can not easily step down. This effect was first discovered by Ehrlich, and afterwards discussed by Schwöbel. Therefore it is also sometimes referred to as Ehrlich-Schwöbel barrier [Sch66; Ehr66].

In various material systems this barrier is known to have an immense impact on island formation. By changing its value or assuming it to be asymmetric, meaning that the barriers for a jump up and a jump down differ, three different growth regimes may be achieved. These are homogeneous, globular and granular growth [Els03]. Without the Schwöbel barrier at relatively high temperatures ( $T = 750$  K) homogeneous growth takes place. Since high temperatures are responsible for smoothing the surface, in general. For lower temperatures the relaxation mechanism becomes less effective, and the stochastic nature of the deposition process prevails. At  $T = 500$  K a rough surface with random morphology develops (granular growth). Switching on the Schwöbel barrier ( $E_{SCH} = 0.2$  eV) results in a growth instability [Kru00] favoring the nucleation of new islands on top of existing islands. This leads to the third regime: globular growth. In this regime even at  $T = 750$  K distinct compact islands with a well-defined average spacing emerge due to the suppressed adatom mobility at step edges.

However, in some material systems [Shi96] and in particular in material systems relevant for semiconductor QD growth, such as Si and InAs/GaAs, this barrier turned out to be small [Rob02]. In the growth simulation presented here, the Schwöbel barrier is implemented as an additional energy term  $E_{SCH}$ , contributing to the total energy of Eq. (2.20), which in the case of an adatom jumping down or up becomes

$$E = E_s + E_n + E_{SCH} - E_{str} ,$$

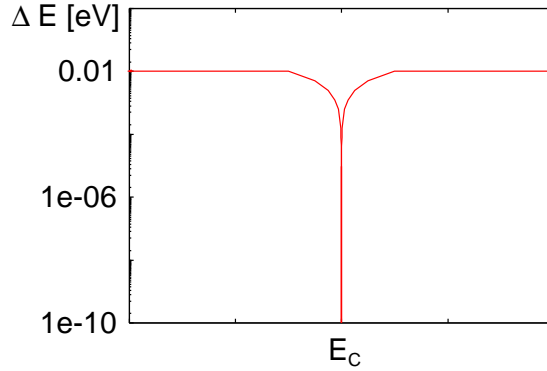
where we use a value of  $E_{SCH} = 0.1$  eV. It should be noted that in the case of a vertical adatom-jump our simulation does not take into account the (vertical) jump length, since we simulate in low coverage regimes. One possibility to overcome this restriction in the framework of a solid-on-solid (SOS) model is described in [Els05a].

## 2.4.2 Energy intervals

As mentioned in Sec. 2.2 the use of energy intervals in the Monte Carlo algorithm is an essential ingredient. On the one hand all values for deposition and diffusion are discrete and known beforehand, on the other hand the continuous values of the strain field contribute to the total energy of an event. So the total energy covers a continuous range. This makes the creation of a structure consisting of energy intervals, in which all events are to be sorted in, necessary. In every Monte Carlo step, there exists a sample set of processes (as deposition and diffusion events), each with a certain probability. The algorithm which is used works as follows (see also Appendix E):

- (1) the sample set is sorted according to the probabilities,

**Figure 2.8:** Adaptive energy intervals. In the neighborhood of a critical energy  $E_C$  the number of energy intervals (each with a width of  $\Delta E$ ) is dramatically increased close to the numerical precision.



- (2) classes are formed from the sorted sample set, which build up a probability-vector,
- (3) randomly one class is selected, and
- (4) randomly again one event from this class is selected, and is executed.

Instead of choosing a linear interval distribution for the above mentioned classes, in a certain interval around ‘critical points’ the number of intervals is increased close to the numerical precision (Fig. 2.8). Such points are, e.g., the binding energy to the substrate plus  $n$  times the next neighbor bond strength. With this, we ensure that, without having a large number of classes, the dynamics is governed by the probabilities of the processes and *not* by the grain size of the mesh. In particular the mechanism of the formation of nuclei in the presence of a small additional energy field, which is important since the size of a critical nucleus (the smallest stable island size) is known to be small, is therefore modeled with high accuracy.

### 2.4.3 Growth parameters

At this stage all ingredients for starting a simulation of one layer of QDs have been obtained. The question, how to handle a stacked array of QDs will be addressed in the following section. To summarize, here all relevant growth parameters will be listed. They can be separated into material dependent parameters and experimentally accessible growth parameters. While the first category already was explained in detail in Sec. 2.4, pp. 21 and Sec. 2.4.1, p. 21 some remarks should be given for the latter one.

We start all of our growth simulations on a flat wetting layer (see Sec. 1.1). According to the flux rate  $F$  adatoms are deposited on the surface at random positions. They are allowed to move according to the Arrhenius rate Eq. (2.19), where the temperature  $T$  and the energy terms  $E_S$  and  $E_b$  enter. Moreover the adatom movement is influenced by the strain field. However, after having deposited a certain amount of adatoms on the surface the flux is switched of. This amount is described by the coverage  $c$ . From this point only diffusion processes take place until a given total simulation time  $t$  is

surface binding energy	$E_S = 1.3 \text{ eV}$
binding energy to one nearest neighbor	$E_b = 0.3 \text{ eV}$
coupling between initial and final sites	$c_f = 0.2$
attempt frequency	$\nu_0 = 10^{13} \text{ s}^{-1}$
Schwöbel barrier	$E_{SCH} = 0.1 \text{ eV}$
temperature	$T = 700, \dots, 800 \text{ K}$
flux rate	$F = 0.01, 0.10, 1.00 \text{ Monolayers (ML)/s}$
coverage	$c = 0.3 \%$
growth time	$t = 50 \text{ s}$
simulation area	$L_x, L_y = 100 \text{ lattice sites (l.s.)}$

**Table 2.1:** Typical set of parameters for the KMC simulation routine, related to the growth of InAs/GaAs.

reached. The time difference between switching of the flux and ending the whole process, experimentally mostly realized by capping, is referred to as growth interruption time  $t_{ir}$ .

The simulation area  $L_x \times L_y$  is connected to ‘normal’ length scales via the mesh size of the lattice on which the simulation is carried out. As grid for our calculations we have chosen the lattice constant of GaAs  $a_{GaAs} = 0.565 \text{ nm}$ , being the parent material in the InAs/GaAs heteroepitaxy. If not stated otherwise we have taken a simulation area of  $100 \times 100$  lattice sites (l.s.), which is smaller than in previous studies [e.g. Mei03a] by a factor of two. Doing KMC simulations of one layer of strained QDs already is computationally highly expensive. Simulating several layers of stacked QDs, and probably running the simulation for one set of parameters more than one time to do some statistics, finally forced us to reduce the simulation area.

An example (similar to that of Sec. 2.4 but more refined here) should clarify the meaning of the parameters introduced above. Consider a system of  $100 \times 100$  l.s. with a flux rate of  $F = 0.01 \text{ ML/s}$ , a coverage of  $c = 0.3 \%$  and a total simulation time  $t = 50 \text{ s}$ . Every  $1/100$  second an atom will be placed randomly on the surface until after  $30 \text{ s}$  the desired coverage is reached. The surface can relax during the growth interruption time of  $t_{ir} = 20 \text{ s}$  while the flux is switched off ( $F = 0$ ).

A comprehensive list of all relevant growth parameters and their values is given in Tab. 2.1.

#### 2.4.4 Simulation of Quantum Dot stacks

Starting in Chapter 5 we will present results of the above described KMC simulation, which should be sketched in short here (see Fig. 2.9). Starting with a perfect, defect free, wetting layer (Fig. 2.9, (a)), which is not simulated explicitly, we deposit adatoms randomly with a given flux rate. At the surface they are allowed to move according to the Arrhenius law until a certain time is reached (Fig. 2.9, (b)). Since the growth sim-

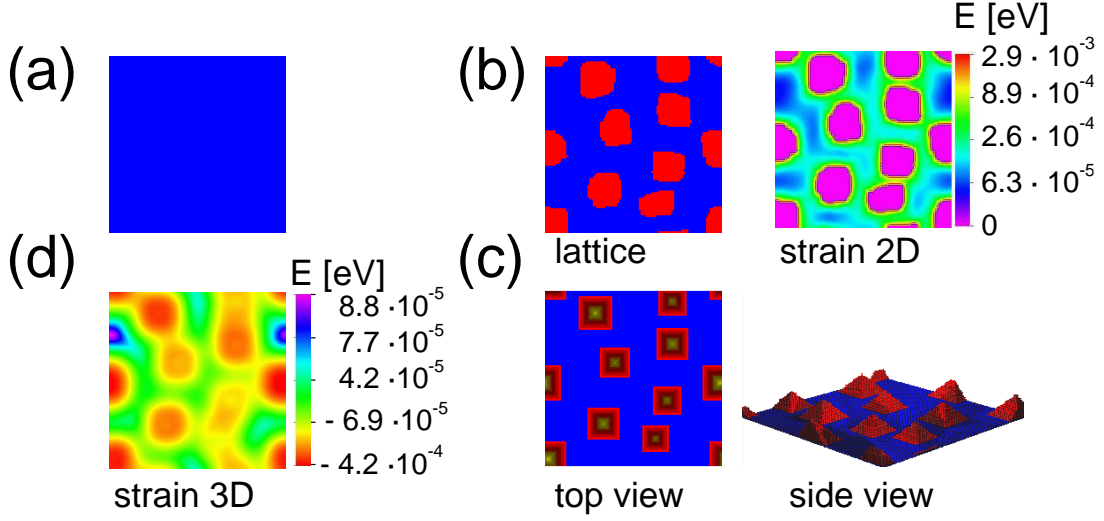


**Figure 2.9:** Sketch of the growth simulation method, a kinetic Monte Carlo (KMC) routine combined with the strain field which is taken into account self-consistently and calculated in the framework of elasticity theory. Starting with a wetting layer (a) the island fundamentals are simulated using KMC under the presence of the two-dimensional strain field (b) plus the strain field from all layers beneath, then a three-dimensional shape is superimposed (c) and the structure is capped with a spacer layer. The three-dimensional strain on the spacer layer is calculated (d), which is acting on the adatoms of the next quantum dot layer (a).

ulation does not deal with the three-dimensional growth of islands, but rather focuses on the positions of the island fundamentals, a three-dimensional (3D) shape is imposed to the simulation result (Fig. 2.9, (c)).

We have restricted ourselves to the simulation of the island fundamentals for the following reasons: Submonolayer islands serve as precursors (platelets) for the growth of three-dimensional islands and thus determine the position and the size of the quantum dots in the SK growth mode [Pri95]. Since we focus on the size and position ordering of the array of quantum dots, and not on the 3D morphology of individual dots, it is sufficient to simulate the growth of the submonolayer platelets.

However, to treat the strain field correctly it is necessary to superimpose a three-dimensional shape, since the strain field strongly depends on the volume and the center of mass of the structures (Ch. 4). This is done by calculating the number of members  $s_i$  and the center of mass  $\mathbf{r}_i^{com}(x, y)$  of each simulated island  $i$ . The baselength  $l_i$  of one island equals approximately the square root of the number of members. In units of the grid chosen in the simulations, namely  $a_{GaAs}$ , i.e., the lattice constant of GaAs

$$l_i \approx \sqrt{s_i} a_{GaAs}.$$

The 2D islands on the surface are then replaced by 3D pyramids with a quadratic base of the length of  $l_i$  and a height of  $2/3 l_i$  centered at  $\mathbf{r}_i^{com}(x, y)$ . Both, the choice of

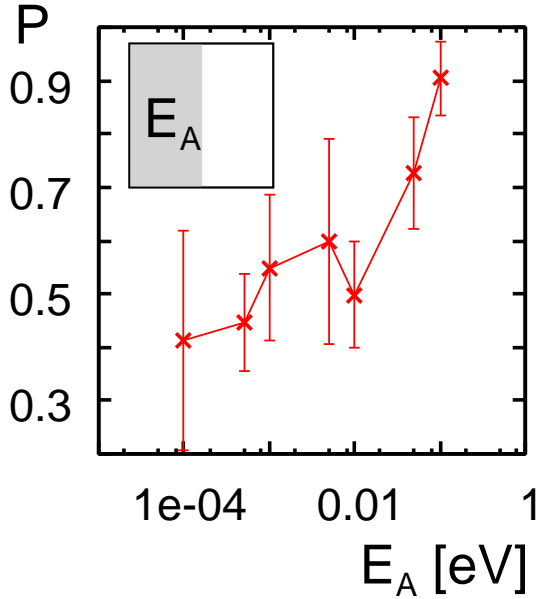


**Figure 2.10:** Simulations with an additional energy barrier  $E_A$  at the left half of the sample (see inset). The ratio  $P$  of atoms in the left half to the total number of atoms is shown. Sample size  $50 \times 50$  lattice sites (l.s.),  $T = 700$  K,  $c = 0.1$  monolayer (ML),  $F = 0.01$  ML/s, simulation time 50 s, average over 10 runs was taken. The errorbars show the standard deviation.

the shape and the choice of the height are supported by experimental findings [see e.g. [Led96](#); [Moi94](#)] and are discussed in Sec. 6.1.

Assuming that the final structure of 3D pyramids is fixed, we cover it implicitly with a spacer layer of the parent material and calculate the three-dimensional strain field generated by the meanwhile buried islands (Fig. 2.9, (d)). At this stage the cycle closes (Fig. 2.9, (d)→(a)). Again the next layer of islands can be grown via KMC simulation and so forth. All adatoms are moving under the influence of the strain field (see Ch. 3), resulting from both, all buried islands and the islands in the growing plane, which directly acts on the jump barriers.

### 2.4.5 Sensitivity of the KMC simulation

In this section we will address the question how additional energy terms in the Arrhenius factor (Eq. (2.19)) act on adatom diffusion and in particular on the positions of stable nuclei. This point is of interest since later (Ch. 5 and the following) the impact of the so called elastic strain energy on adatom diffusion will be discussed. However, an additional energy may be interpreted in other ways, so for example one could have in mind a sample with an inhomogeneous energy surface due to temperature fluctuations [[Nur01](#)] or a sample with anisotropic surface diffusion [[Mei03a](#)], e.g., due to a certain reconstruction.

The test scenario is the following: we prepare a growth sample such that one half of the sample acts as an energy trap, meaning that at the left half side of the sample a certain energy  $E_A$  acts as additional diffusion barrier. Such, that the energy of the Arrhenius term (Eq. (2.19)) for adatoms being in the left half plane becomes  $E = E_s + E_b + E_A$ .

If the energy has no influence on the island positions, one expects that half of the islands will be found on the left side of the growth sample and the others on the right side. From the modeling point of view we already pointed out how it is ensured that we measure the impact of additional energies with high accuracy (see Sec. 2.4.2).

In Fig. 2.10 the ratio of the number of atoms in the left half of the sample (where the additional barrier is introduced) to the total number of adatoms is shown. It is clearly to be seen, that starting from  $E_A \approx 0.01$  eV the impact on adatom diffusion becomes visible. To generalize this finding, one can conclude that any additional energy which is of the order of one tenth of the neighbor bond strength  $E_b$  or higher may influence the positions of nuclei. Or vice versa: if an additional energy, which is less than one tenth of the binding energy to the next neighbors, acts on the diffusion barrier, so *no*, or to be careful one should state ‘almost no’, influence on island positions can be expected.

# Chapter 3

## Strain field from elasticity theory

In the heteroepitaxial growth of lattice mismatched materials, e.g., InAs/GaAs, after the deposition of the substrate of material  $A$  with a lattice constant  $a_A$  a second material of type  $B$  having a different lattice constant  $a_B$  is deposited. Among other properties, it is mainly the difference in the lattice parameter which finally leads to the desired growth mode—in the self-organized growth of quantum dot arrays the layer-plus-island growth, referred to as Stranski-Krastanov (SK) growth mode. After the growth of a thin *pseudomorphic* layer of material  $B$ , i.e., atoms of material  $B$  adopt the lattice constant  $a_A$  of the substrate, a transition from two-dimensional layer growth towards the three-dimensional formation of islands occurs.

Thus, in lattice mismatched systems we deal with the deformation of bodies, the displacement of atoms and the consequences coming with that. An appropriate way to describe such problems can be found in the framework of elasticity theory. Since we are interested in effects on a mesoscopic scale the description using a mesoscopic method is sufficient, instead of calculating the atomistic details from first principles, and moreover both approaches give the same results when one chooses appropriate length scales.

Detailed information about elasticity theory coming with extensive deviations of the formalism can be found in many textbooks [Lan70; Saa74; Kha83]. After the next introductory section the reader will be guided towards the formulation of the final equations for the three-dimensional anisotropic strain field, which is used throughout this thesis for the investigations of static arrays of quantum dots of various shapes and arrangement (Ch. 4) and growth simulations of one (Ch. 5) and multiple layers (Ch. 6) of quantum dot arrays.

### 3.1 Linear elasticity theory—basic equations

Considering a piece of material initially located at  $\mathbf{r}$ , the change of the position can be described by the displacement vector  $\mathbf{u}(\mathbf{r})$

$$\mathbf{r}' = \mathbf{r} + \mathbf{u}(\mathbf{r}) \quad (3.1)$$

where  $\mathbf{r}'$  is the final position. With respect to crystals  $\mathbf{r}$  corresponds to the bulk state and  $\mathbf{r}'$  gives the position in the deformed system. The next task is to determine the displacement vector  $\mathbf{u} = (u_1, u_2, u_3)^T$  and its variation.

For small deviations of the displacement vector

$$\frac{\partial u_i}{\partial r_j} = \nabla_j u_i \ll 1, \quad (3.2)$$

with  $\nabla_j$  being the nabla operator and indices  $i, j \in \{1, 2, 3\}$ , partial differential equations can be derived, which give an answer to the question of the behavior of the displacement field. More specifically, if we know the elastic field, i.e., the relative displacement of all atoms, the force that an inclusion exerts on another and the elastic interaction energy of elastic inclusions, can be calculated. At the end of this chapter, all necessary conditions for computing these quantities will be provided.

The information about the change of the displacement vector is contained in the derivative tensor  $\nabla_i u_j$ , which in linear approximation can be split into a symmetric part, the *strain tensor*

$$\varepsilon_{ij} = \frac{1}{2} (\nabla_j u_i + \nabla_i u_j) \quad (3.3)$$

and an antisymmetric part, the *rotation tensor*

$$\omega_{ij} = \frac{1}{2} (\nabla_j u_i - \nabla_i u_j) \quad (3.4)$$

respectively. Since by definition  $\varepsilon_{ij} = \varepsilon_{ji}$  the strain tensor contains six independent components. While the diagonal components, the normal strain  $\varepsilon_{ii}$ , represent compression or dilatation along the axis of the chosen coordinate system, the shear strain is contained in the non-diagonal components  $\varepsilon_{ij} (i \neq j)$ . In the rotation tensor  $\omega_{ij}$  only three independent variables remain, since  $\omega_{ii} = 0$  and  $\omega_{ij} = -\omega_{ji}$  for  $(i \neq j)$ . They can be written as a vector expressed by the curl operator as

$$\boldsymbol{\omega} = \begin{pmatrix} \omega_{32} \\ \omega_{13} \\ \omega_{21} \end{pmatrix} = \frac{1}{2} \nabla \times \mathbf{u}(\mathbf{r}). \quad (3.5)$$

The above given quantities describe geometrical effects due to distortion *inside* a material. If an *external* force  $\mathbf{f}$  acts on some volume  $V$  of material in static equilibrium, this must be described by the divergence of a tensor of second rank—the *stress tensor*  $\sigma_{ij}$

$$\nabla_j \sigma_{ij} + f_i = 0 \quad (3.6)$$

Here as well as in the following, Einstein's summation convention over equal indices is used. The elements of the stress tensor  $\sigma_{ij}$  represent the force component along

$ij, kl \rightarrow m, n$	$ij, kl \rightarrow m, n$	$ij, kl \rightarrow m, n$
11 $\rightarrow$ 1	23 $\rightarrow$ 4	32 $\rightarrow$ 4
22 $\rightarrow$ 2	31 $\rightarrow$ 5	13 $\rightarrow$ 5
33 $\rightarrow$ 3	12 $\rightarrow$ 6	21 $\rightarrow$ 6

**Table 3.1:** Conversion of the indices of the stiffness tensor into Voigt notation.

the  $i$ -direction acting on a unit surface perpendicular to the  $j$ -axis. The connection between stress and strain tensor can be written in a linear form known as Hooke's law

$$\sigma_{ij} = \lambda_{ijkl} \varepsilon_{kl} \quad (3.7)$$

with the (material) constants  $\lambda_{ijkl}$  being referred to as *stiffness* tensor or elastic moduli. In full generality this tensor consists of 81 elements, but the luck is this time on the side of the theoretician, it can be shown that only 21 of them are independent. For an easier notation, instead of using the indices  $ij$  and  $kl$ ,  $m$  and  $n$  as indicated in Tab. 3.1 are used, which is referred to as 'Voigt notation'. Restricting oneself to cubic materials, even more components can be substituted and only three independent elastic moduli, in Voigt notation  $c_{11}$ ,  $c_{12}$ , and  $c_{44}$ , remain. Values of these quantities are listed in the Appendix D.2 for some selected materials. For cubic crystals Hooke's law can be written as

$$\begin{pmatrix} \sigma_{11} \\ \sigma_{22} \\ \sigma_{33} \\ \sigma_{12} \\ \sigma_{13} \\ \sigma_{23} \end{pmatrix} = \begin{pmatrix} c_{11} & c_{12} & c_{12} & 0 & 0 & 0 \\ c_{12} & c_{11} & c_{12} & 0 & 0 & 0 \\ c_{12} & c_{12} & c_{11} & 0 & 0 & 0 \\ 0 & 0 & 0 & c_{44} & 0 & 0 \\ 0 & 0 & 0 & 0 & c_{44} & 0 \\ 0 & 0 & 0 & 0 & 0 & c_{44} \end{pmatrix} \begin{pmatrix} \varepsilon_{11} \\ \varepsilon_{22} \\ \varepsilon_{33} \\ \varepsilon_{12} \\ \varepsilon_{13} \\ \varepsilon_{23} \end{pmatrix} \quad (3.8)$$

If we further assume that the material of interest is homogeneously isotropic, only two independent elastic constants remain. The so-called Lamé coefficients  $\lambda$  and  $\mu$  are connected to the elastic moduli via

$$c_{11} = \lambda + 2\mu \quad , \quad c_{12} = \lambda \quad , \quad \text{and} \quad c_{44} = \mu \quad (3.9)$$

such that Hooke's law now becomes

$$\sigma_{ij} = 2\mu \varepsilon_{ij} + \lambda \delta_{ij} \varepsilon_{nn} . \quad (3.10)$$

This should, however, be the end of simplifications. The isotropic approximation and its application to the problem of computing the strain field of quantum dots (Sec. 3.5) is mentioned only for the sake of completeness here. All calculations shown later on are done with the anisotropic strain field of this chapter.

## 3.2 Elastic energy of interacting inclusions

At first it is useful to list the assumptions under which our problem is considered:

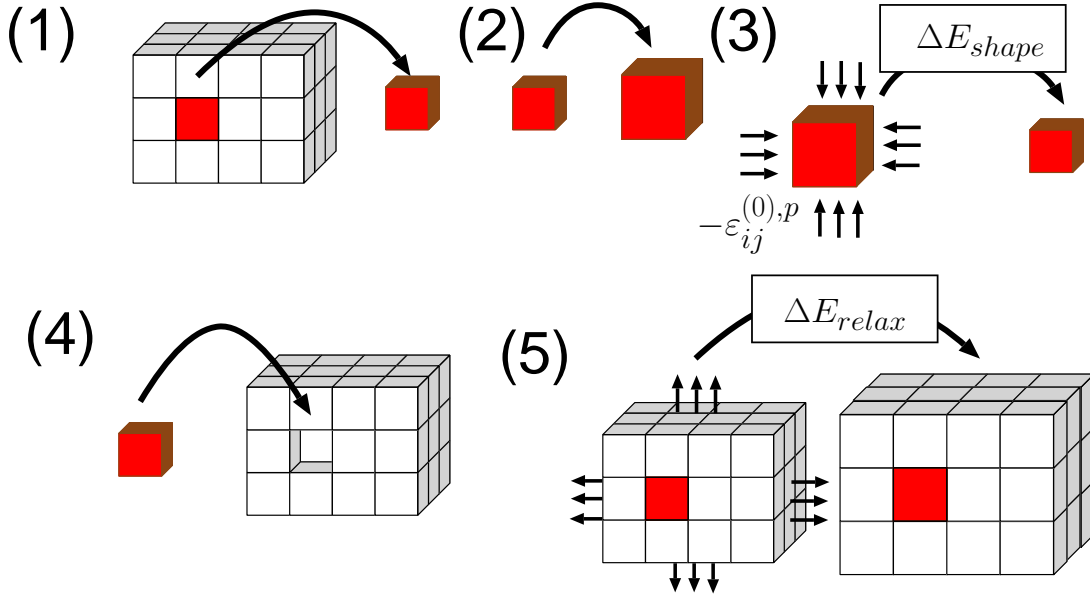


**Figure 3.1:** Schematic illustration for a fictitious experiment to evaluate the energy of interacting elastic inclusions.

- The size and distances of the inclusions are small compared to the typical length dimensions of the parent material.
- Both materials have the same elastic moduli  $\lambda_{ijklm}$ , namely the ones of the parent material. This is the so-called ‘homogeneous moduli approximation’, and probably intuitively clear assuming the validity of the previous point.
- At external boundaries  $S$  the stress vanishes, which is referred to as stress-free boundary condition and can be expressed using the normal vector  $n_j$  as follows:

$$n_j(\mathbf{r})\sigma_{ij}(\mathbf{r})\Big|_S = 0.$$

Using Hookes law Eq. (3.7), (3.8) and the definition of the strain tensor Eq. (3.3), we can rewrite the above equation as:

$$n_j(\mathbf{r}) (\lambda_{ijkl} \nabla_k u_l(\mathbf{r})) \Big|_S = 0. \quad (3.11)$$

For the following considerations we introduce the stress-free strain  $\varepsilon_{ij}^{(0),p}$  describing the shape deformation of the parent material. The type of material is denoted by the superscript  $p$ . The considerations of this section also can be found in [Kha83].

Now one can think of an algorithm that describes the strain energy using the following fictitious experiment (Fig. 3.1):

- (1) Cutting the inclusions out, since they are assumed to be small, the energy is not affected.
- (2) Transform each inclusion to a new phase corresponding to one of the crystal lattice rearrangements. The expansion is described by  $\varepsilon_{ij}^{(0),p}$ . Again the energy does not change since we are considering stress-free strain.
- (3) Restore the previous shape of the inclusions by applying surface forces, i.e., surface traction. Here, the homogeneous strain with the value  $\varepsilon_{ij} = -\varepsilon_{ij}^{(0),p}$  is required. The internal stress due to surface traction can be expressed as  $\sigma_{kl} = -\lambda_{ijkl}\varepsilon_{ij}^{(0),p}$  and therefore the energy change during this step can be written as

$$\Delta E_{shape} = \frac{1}{2} \sum_p v^p \lambda_{ijkl} \varepsilon_{ij}^{(0),p} \varepsilon_{kl}^{(0),p} \quad (3.12)$$

where the volume of the inclusion is denoted by  $v^p$ .

- (4) Now we have to reinsert the inclusions. In the last step we ensured that they fit into the holes, therefore here the energy change is zero again.
- (5) Finally we let the volume relax. The associated relaxation energy per unit volume can be expressed as a power series in the deformations  $\varepsilon_{ij}(\mathbf{r})$ . Considering only terms up to second order

$$f_{relax}(\mathbf{r}) = -\sigma_{ij}^{(0)}(\mathbf{r})\varepsilon_{ij} + \frac{1}{2}\lambda_{ijkl}\varepsilon_{ij}\varepsilon_{kl} \quad (3.13)$$

with expansion coefficients  $\sigma_{ij}^{(0)}(\mathbf{r})$  and  $\lambda_{ijkl}$ . Integration over the volume gives the total relaxation energy

$$\Delta E_{relax} = \int_V d^3\mathbf{r} \left( -\sigma_{ij}^{(0)}(\mathbf{r})\varepsilon_{ij} + \frac{1}{2}\lambda_{ijkl}\varepsilon_{ij}\varepsilon_{kl} \right). \quad (3.14)$$

Summing up all non-zero energies we can write down the elastic energy

$$\begin{aligned} E_{el} &= \Delta E_{shape} + \Delta E_{relax} \\ &= \frac{1}{2} \sum_p v^p \lambda_{ijkl} \varepsilon_{ij}^{(0),p} \varepsilon_{kl}^{(0),p} + \int_V d^3\mathbf{r} \left( -\sigma_{ij}^{(0)}(\mathbf{r})\varepsilon_{ij} + \frac{1}{2}\lambda_{ijkl}\varepsilon_{ij}\varepsilon_{kl} \right). \end{aligned} \quad (3.15)$$

Note that  $E_{el}$  is an energy density. The strain energy  $E_{str}$  of our growth simulations which enters the Arrhenius term of Eq. (2.19) is the elastic interaction energy of adatoms. It is derived in Sec. 3.3 (see Eqs. (3.42), (3.43)).

In the stress-free state being considered, in general, the system shows non-zero strain, i.e., if  $\sigma_{ij}(\mathbf{r}) = 0$  and  $\mathbf{r}$  is inside a particle of type  $p$  then  $\varepsilon_{ij}(\mathbf{r}) = \varepsilon_{ij}^{(0),p} \neq 0$ . Introducing a shape function  $\vartheta^p(\mathbf{r})$  of particles of type  $p$ , with

$$\vartheta^p(\mathbf{r}) = \begin{cases} 1 & \text{if } \mathbf{r} \text{ is inside a particle of type } p \\ 0 & \text{else,} \end{cases} \quad (3.16)$$

such that

$$\int_V d^3\mathbf{r} \vartheta^p(\mathbf{r}) = v^p \quad (3.17)$$

the stress-free strain becomes:

$$\varepsilon_{ij}^{(0)}(\mathbf{r}) = \sum_p \vartheta^p(\mathbf{r}) \varepsilon_{ij}^{(0),p}. \quad (3.18)$$

The elastic stress also can be expressed as [Lan70]

$$\sigma_{ij}(\mathbf{r}) = \frac{\delta E_{el}}{\delta \varepsilon_{ij}(\mathbf{r})}. \quad (3.19)$$

Combining Eq. (3.15) and Eq. (3.19) we gain

$$\sigma_{ij}(\mathbf{r}) = -\sigma_{ij}^{(0)} + \lambda_{ijkl} \varepsilon_{kl} \quad (3.20)$$

If we set  $\sigma_{ij}(\mathbf{r}) = 0$  the connection between the stress-free strain  $\varepsilon_{ij}^{(0)}(\mathbf{r})$  and the tensor  $\sigma_{ij}^{(0)}(\mathbf{r})$  becomes clear: Eq. (3.20) can be transformed into

$$\sigma_{ij}^{(0)}(\mathbf{r}) = \lambda_{ijkl} \varepsilon_{kl}^{(0)}(\mathbf{r}) \quad (3.21)$$

giving the explanation for the meaning of the expansion coefficient in Eq. (3.13).

In mechanical equilibrium strain and displacements both minimize the relaxation energy giving the following sets of equations [Kha83]

$$\frac{\partial \Delta E_{relax}}{\partial \varepsilon_{ij}} = 0 \quad \text{and} \quad (3.22a)$$

$$\frac{\partial \Delta E_{relax}}{\partial u_i(\mathbf{r})} = 0. \quad (3.22b)$$

Substituting the relaxation energy of Eq. (3.14) into Eq. (3.22a) immediately gives

$$-\sigma_{ij}^{(0)} = \frac{1}{2} \lambda_{ijkl} \varepsilon_{ij}(\mathbf{r}) \quad (3.23)$$

which can be used to write the relaxation energy Eq. (3.14) in a more simple form

$$\Delta E_{relax} = -\frac{1}{2} \int_V d^3\mathbf{r} \sigma_{ij}^{(0)}(\mathbf{r}) \varepsilon_{ij} \quad (3.24)$$

and leads to an equation for the elastic energy, Eq. (3.15), of the form of

$$E_{el} = \frac{1}{2} \sum_p \int_V d^3\mathbf{r} \sigma_{ij}^{(0),p} \vartheta^p(\mathbf{r}) \left( \varepsilon_{ij}^{(0),p} - \varepsilon_{ij}(\mathbf{r}) \right). \quad (3.25)$$

An commonly used expression for the equilibrium condition can be derived by taking into account the condition of Eq. (3.22b) and calculating the first variational derivative of the relaxation energy Eq. (3.14) while keeping in mind the symmetry properties of the tensors

$$\sigma_{ij}^{(0),p} = \sigma_{ji}^{(0),p} \quad \text{and} \quad \lambda_{ijkl} = \lambda_{klij} = \lambda_{jikl}. \quad (3.26)$$

Substituting Eq. (3.14) into Eq. (3.22b) and using the connection between the strain and the displacements of Eq. (3.3) we gain

$$\delta\Delta E_{relax} = \int_V d^3\mathbf{r} \left( - \sum_p \sigma_{ij}^{(0),p} \nabla_j \vartheta^p(\mathbf{r}) \nabla_j \delta u_i + \lambda_{ijkl} \nabla_l u_k \nabla_j \delta u_i \right) \quad (3.27)$$

Since the variation  $\delta\mathbf{u}$  vanishes at the body surface, Gauss's theorem may be applied, reducing Eq. (3.27) to

$$\delta\Delta E_{relax} = \int_V d^3\mathbf{r} \left( - \sum_p \sigma_{ij}^{(0),p} \nabla_j \vartheta^p(\mathbf{r}) - \lambda_{ijkl} \nabla_j \nabla_l u_k \right) \delta u_i \quad (3.28)$$

which leads to

$$\frac{\partial\Delta E_{relax}}{\partial u_i} = \sum_p \sigma_{ij}^{(0),p} \nabla_j \vartheta^p(\mathbf{r}) - \lambda_{ijkl} \nabla_j \nabla_l u_k \quad (3.29)$$

Substituting Eq. (3.29) into the equilibrium condition of Eq. (3.22b) finally gives

$$\lambda_{ijkl} \nabla_j \nabla_l u_k = \sum_p \nabla_j (\sigma_{ij}^{(0),p} \vartheta^p(\mathbf{r})), \quad (3.30)$$

an equilibrium equation for the local displacements.

For further information and a more refined discussion see [Kha83].

### 3.3 Elastic energy in terms of the Green's tensor

In general, the Green's tensor is the reverse of a differential operator of a boundary problem. In our case the static Green's tensor  $G_{ij}(\mathbf{r}, \mathbf{r}')$  of the elasticity theory fulfills the equilibrium condition

$$\lambda_{ijkl} \nabla_j \nabla_l u_k(\mathbf{r}) = \nabla_j (\sigma_{ij}^{(0)} \vartheta(\mathbf{r})) \quad (3.31)$$

and the boundary condition

$$n_j(\mathbf{r}) (\lambda_{ijkl} \nabla_k u_l(\mathbf{r})) \Big|_S = 0 \quad (3.32)$$

The connection between the Green's tensor and the displacement vector or in other words, the solution of the equilibrium equation with respect to the boundary condition, is then given by

$$u_i(\mathbf{r}) = \int d^3\mathbf{r}' G_{ij}(\mathbf{r}, \mathbf{r}') f_j(\mathbf{r}') \quad (3.33)$$

To derive an expression of elastic energy in terms of the Green's tensor of Eq. (3.33) we start at the definition of Eq. (3.3)

$$\int_V d^3\mathbf{r} \sigma_{ij}^{(0),p} \vartheta^p(\mathbf{r}) \varepsilon_{ij} = \int_V d^3\mathbf{r} \sigma_{ij}^{(0),p} \vartheta^p(\mathbf{r}) \nabla_j u_i \quad (3.34)$$

substituting the definition of the Green's tensor Eq. (3.33)

$$= \int d^3\mathbf{r} \int d^3\mathbf{r}' \sigma_{ij}^{(0),p} \vartheta^p(\mathbf{r}) \nabla_i G_{il}(\mathbf{r}, \mathbf{r}') f_l(\mathbf{r}') \quad (3.35)$$

using the expressions for the equilibrium condition Eq. (3.6), Eq. (3.30)

$$= \int d^3\mathbf{r} \int d^3\mathbf{r}' \sigma_{ij}^{(0),p} \vartheta^p(\mathbf{r}) \nabla_i G_{il}(\mathbf{r}, \mathbf{r}') \nabla'_m \sigma_{lm}^{(0),q} \vartheta^q(\mathbf{r}') \quad (3.36)$$

the elastic energy of Eq. (3.25) can be transferred to

$$E_{el} = \frac{1}{2} \sum_p \int_V d^3\mathbf{r} \sigma_{ij}^{(0),p} \vartheta^p(\mathbf{r}) \varepsilon_{ij}^{(0),p} - \frac{1}{2} \sum_{p,q} \int_V d^3\mathbf{r} \int d^3\mathbf{r}' \sigma_{ij}^{(0),p} \vartheta^p(\mathbf{r}) \nabla_j G_{il}(\mathbf{r}, \mathbf{r}') \nabla'_m \sigma_{lm}^{(0),q} \vartheta^q(\mathbf{r}') \quad (3.37)$$

Now we introduce the 2D shape functions  $\tilde{\vartheta}^{B,S}$  and the 2D position vector  $\mathbf{r}_{\parallel} = (x, y)$  the shape of islands with heights  $h^S$  and  $h^B$  (the superscripts  $B, S$  refer to buried and surface islands) can be described by

$$\begin{aligned} \vartheta^B(\mathbf{r}) &= h^B \tilde{\vartheta}^B(\mathbf{r}_{\parallel}) \delta(z_0 - z_1) \quad \text{and,} \\ \vartheta^S(\mathbf{r}) &= h^S \tilde{\vartheta}^S(\mathbf{r}_{\parallel}) \delta(z_0) \end{aligned} \quad (3.38)$$

such that, e.g., the volume of a surface island is given by

$$\begin{aligned} \int_V d^3\mathbf{r} \vartheta^S(\mathbf{r}) &= \int_V d^3\mathbf{r} h^S \tilde{\vartheta}^S(\mathbf{r}_{\parallel}) \delta(z_0) \\ &= h^S \int_A d^2\mathbf{r}_{\parallel} \tilde{\vartheta}^S(\mathbf{r}_{\parallel}) \end{aligned}$$

The stress-free strain condition at  $z = z_0$  may be applied, since we assume that the (surface-) islands of interest have a small height compared to their lateral extension (the variables and notation used from now on is illustrated in Fig. 3.3).

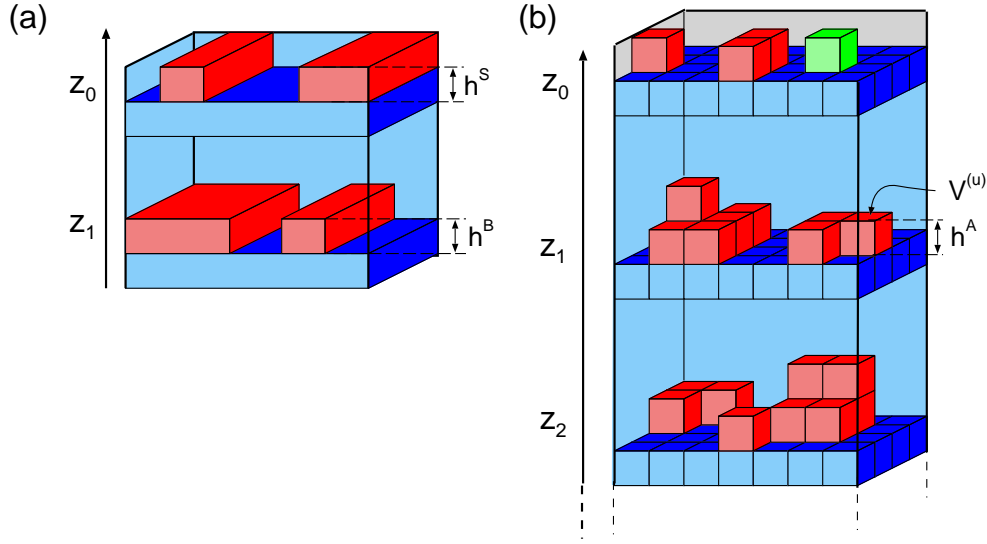


**Figure 3.2:** Illustration of the energy terms used in our calculations. The elastic interaction energy  $E_{el}^A$  of two arrays of islands (a), one at the surface and a buried one, was derived in [Shc98b]. Here we calculate the elastic interaction energy  $E_{el}^V(\mathbf{r}_{\parallel}, z = z_0) = E_{str}$  acting on an adatom (green) located at the surface (b). This is done in the framework of a solid-on-solid model. The grid of our calculations is the lattice constant  $a_{GaAs}$  of the parent material GaAs, such that the volume of all adatoms is  $V^{(u)} = a_{GaAs}^3$ . The contributions come from other adatoms (red) and can be divided into two parts: one contribution from adatoms located at the surface (grey region) denoted by  $E_{el}^{2D}$  and the other from adatoms located beneath the surface (blue region)  $E_{el}^{3D}$ .

Taking only into account the interaction energy of surface islands with buried islands ( $p = S, q = B$ ) and using the 2D shape functions of Eq. (3.38) we arrive at an expression for the elastic energy of interacting inclusions per unit surface area  $E_{el}^A$  as is used in [Shc98b, (Eq. 2.11)]

$$\begin{aligned}
 E_{el}^A &= \frac{h^S h^B}{A} \\
 &\times \int d^2 \mathbf{r}_{\parallel} \int d^2 \mathbf{r}'_{\parallel} \tilde{\vartheta}^S(\mathbf{r}_{\parallel}) \sigma_{ij}^{(0)S} [\nabla_j \nabla'_m G_{il}(\mathbf{r}_{\parallel} - \mathbf{r}'_{\parallel}; z, z')] \Big|_{\substack{z=z_0 \\ z'=z_0-z_1}} \sigma_{lm}^{(0)B} \tilde{\vartheta}^B(\mathbf{r}'_{\parallel})
 \end{aligned} \tag{3.39}$$

with  $A$  being the total surface area.

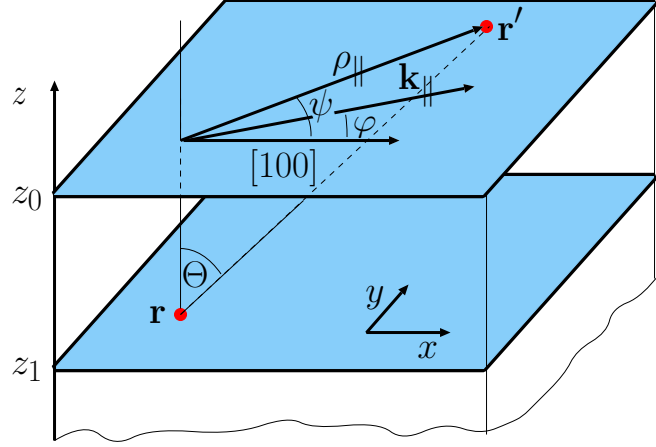


**Figure 3.3:** Illustration of the notation used. Two elastic point defects (red points) are located at  $\mathbf{r}$  and  $\mathbf{r}'$ .

Since it is convenient to calculate the Green's tensor in  $\mathbf{k}$ -space, we define

$$W(\mathbf{r}_{\parallel} - \mathbf{r}'_{\parallel}; z_0 - z_1) = \int \frac{d^2 \mathbf{k}_{\parallel}}{(2\pi)^2} \left\{ \sigma_{ij}^{(0)S} \left[ \tilde{\nabla}_j \tilde{\nabla}'_m \tilde{G}_{il}(\mathbf{k}_{\parallel}; z, z') \right] \Big|_{\substack{z=z_0 \\ z'=z_0-z_1}} \sigma_{lm}^{(0)B} \right\} e^{i\mathbf{k}_{\parallel}(\mathbf{r}_{\parallel} - \mathbf{r}'_{\parallel})} \quad (3.40)$$

with  $\tilde{G}_{il}(\mathbf{k}_{\parallel}; z, z')$  is the Fourier transform of the static Green's tensor  $G_{il}(\mathbf{r}_{\parallel} - \mathbf{r}'_{\parallel}; z, z')$  in elastically anisotropic cubic crystals obtained by Portz and Maradudin [Por77] and  $\tilde{\nabla}_x = ik_x$ ,  $\tilde{\nabla}'_x = -ik_x$ ,  $\tilde{\nabla}_y = ik_y$ , and  $\tilde{\nabla}'_y = -ik_y$ .

Now the strain energy reads

$$E_{el}^A = \frac{h^S h^B}{A} \int d^2 \mathbf{r}_{\parallel} \int d^2 \mathbf{r}'_{\parallel} \tilde{\vartheta}^S(\mathbf{r}_{\parallel}) W(\mathbf{r}_{\parallel} - \mathbf{r}'_{\parallel}; z_0 - z_1) \tilde{\vartheta}^B(\mathbf{r}'_{\parallel}). \quad (3.41)$$

This equation we would like to apply to a more general situation. We are interested in the elastic energy between one adatom in the growing layer (located at the point  $(\mathbf{r}_{\parallel}, z = z_0)$ ) induced by both: islands in all capped/buried layers—which should be treated as 3D structures—and islands in the growing layer (see Fig. 3.2). Another disadvantage of the previous equations is the restriction to plate-shaped, two-dimensional islands with small height. By integrating in the  $z$ -direction as well, we will overcome this restriction. Denoting the volume of our sample by  $V$  and the volume of a unit cell by  $V^{(u)}$  the shape function of an adatom on the surface having a height  $h^A$  and being of the size of a unit cell, is:

$$\vartheta^A(\mathbf{r}) = h^A \tilde{\vartheta}^A(\mathbf{r}_{\parallel}) \delta(z_0) = V^{(u)} \delta(\mathbf{r}_{\parallel}; z = z_0).$$

Therefore the elastic interaction energy between an adatom at the surface and several inclusions

$$E_{el}^V(\mathbf{r}_{\parallel}; z = z_0) = V^{(u)} \int_A \int_{-\infty}^{z_0} d\mathbf{r}'_{\parallel} dz' W(\mathbf{r}_{\parallel} - \mathbf{r}'_{\parallel}; z_0 - z') \quad (3.42)$$

and, with respect to the cubic solid-on-solid model used in our simulation, the integral can be split up into a sum, as

$$E_{el}^V(\mathbf{r}_{\parallel}; z = z_0) = E_{str} = (V^{(u)})^2 \sum_{\mathbf{r}' \in V} W(\mathbf{r}_{\parallel} - \mathbf{r}'_{\parallel}; z_0 - z(\mathbf{r}')). \quad (3.43)$$

This, finally, is the expression which enters as a correction term for the diffusion barriers of the Arrhenius factor in Eq. (2.19). In the further analysis we will derive an expression for the contribution of adatoms in the same plane  $E_{el}^{2D}$  and a second expression accounting for contributions of buried adatoms  $E_{el}^{3D}$  (see Fig. 3.2). The function  $W(\cdot; \cdot)$  is well defined for buried and surface islands as described in the following sections. Of course there are only non-zero contributions for  $\mathbf{r}_{\parallel}$  being inside a (surface/buried) island.

### 3.3.1 The interaction term

To evaluate the interaction term  $W(\mathbf{r}_{\parallel} - \mathbf{r}'_{\parallel}; z_0 - z')$  it is useful to make some more simplifications.

For the stress tensor  $\sigma_{ij}^{(0)}$  we take the tensor with uniaxial symmetry

$$\sigma_{ij}^{(0)S,B} = \begin{pmatrix} \sigma_{\parallel}^{(0)S,B} & 0 & 0 \\ 0 & \sigma_{\parallel}^{(0)S,B} & 0 \\ 0 & 0 & \sigma_{\perp}^{(0)S,B} \end{pmatrix} = \sigma^{(0)S,B} \begin{pmatrix} 1 & 0 & 0 \\ 0 & 1 & 0 \\ 0 & 0 & P^{S,B} \end{pmatrix}$$

and, for further calculations, we set the anisotropy parameter of the stress tensor  $P^{S,B} = 1$ . For inclusions of small height this is a sufficient approximation, a more detailed discussion of this parameter can be found in [Shc98b]. However, it should be stressed that this simplification does not affect the feature of anisotropy, in general.

Therefore we can rewrite the integrand of Eq. (3.40)

$$\sigma_{ij}^{(0)S} \left[ \tilde{\nabla}_j \tilde{\nabla}'_m \tilde{G}_{il}(\mathbf{k}_{\parallel}; z, z') \right] \sigma_{lm}^{(0)B} = \sigma^{(0)S} \left[ \tilde{\nabla}_i \tilde{\nabla}'_j \tilde{G}_{ij}(\mathbf{k}_{\parallel}; z, z') \right] \sigma^{(0)B}$$

Using the formalism developed in [Ipa93; Ipa98], which is based on [Por77], we are able to write down the derivative of the Green's tensor by means of the elastic operator

$$B_{Elastic}(\mathbf{k}_{\parallel}; z, z') = (c_{11} + 2c_{12})^2 \left[ \tilde{\nabla}_i \tilde{\nabla}'_j \tilde{G}_{ij}(\mathbf{k}_{\parallel}; z, z') \right]$$

which can be decomposed in a set of static analogs of Rayleigh waves as

$$B_{Elastic}(\mathbf{k}_{\parallel}; z, z') = B_0 \delta(z - z') + k_{\parallel} \sum_{s=1}^3 C_s(\varphi) e^{-\alpha_s(\varphi) k_{\parallel} (z-z')} + k_{\parallel} \underbrace{\sum_{s=1}^3 \sum_{s'=1}^3 D_{ss'}(\varphi) e^{-\alpha_{s'}(\varphi) k_{\parallel} (z-z')}}_{s \leftrightarrow s'} \quad (3.44)$$

with coefficients  $B_0$ ,  $C_s$ , and  $D_{s's'}$  and the dimensionless  $\alpha_s$  describing the spatial attenuation. The first and the second term correspond to contributions of the infinite cubic medium and the third term accounts for contributions from the surface.

Changing the indices in Eq. (3.44) as indicated, we arrive at

$$\begin{aligned} B_{Elastic}(\mathbf{k}_{\parallel}; z, z') &= B_0 \delta(z - z') + k_{\parallel} \sum_{s=1}^3 \underbrace{\left[ C_s(\varphi) + \sum_{s'=1}^3 D_{s's'}(\varphi) \right]}_{=: R_s(\varphi)} e^{-\alpha_s(\varphi) k_{\parallel} (z-z')} \\ &= B_0 \delta(z - z') + k_{\parallel} \sum_{s=1}^3 R_s(\varphi) e^{-\alpha_s(\varphi) k_{\parallel} (z-z')} \end{aligned} \quad (3.45)$$

with

$$R_s(\varphi) = \frac{(c_{11} + 2c_{12})(c_{11} + 2c_{12})}{c_{11}} \left( \frac{\Delta a}{a} \right)^2 r_s(\varphi).$$

being referred to in [Shc98b] as  $R_s = Q_s$ . The  $c_{ij}$  are the elastic constants in Voigt notation, and  $(\Delta a/a)$  is the lattice mismatch. The dimensionless functions  $r_s(\varphi)$  can be obtained using the equations of [Ipa93, Eq. (A1–A6)], and  $\alpha_s(\varphi)$  are the solutions with positive real part of a polynomial of sixth order [Por77, Eq. (2.16)]. Both can be computed with arbitrary numerical precision (see Appendix C). Here,  $\varphi$  is the angle between  $\mathbf{k}$  and the [100]-direction. Please note that our coordinate system is such, that the  $x$ -axis is directed parallel to the [100]-direction (see Fig 3.3).

Introducing  $\rho_{\parallel} := \mathbf{r}_{\parallel} - \mathbf{r}'_{\parallel}$  and, setting<sup>1</sup>  $B_0 = 0$ , one can now write Eq. (3.40) as:

$$\begin{aligned} W(\rho_{\parallel}; z_0 - z') &= \frac{1}{c_{11}} \left( \frac{\Delta a}{a} \right)^2 (\sigma^{(0)})^2 \\ &\quad \times \int \frac{d^2 \mathbf{k}_{\parallel}}{(2\pi)^2} k_{\parallel} \sum_{s=1}^3 r_s(\varphi) e^{-\alpha_s(\varphi) k_{\parallel} (z_0 - z')} e^{i \mathbf{k}_{\parallel} \rho_{\parallel}}. \end{aligned} \quad (3.46)$$

Since we are dealing only with one sort of inclusions, starting with the equation above, we do not any longer differentiate between surface and buried islands and suppress the superscripts  $S$  and  $B$ .

With the relations  $\int f(\mathbf{k}_{\parallel}) d^2 \mathbf{k}_{\parallel} = \int \int k f(k, \varphi) dk d\varphi$ ,  $\mathbf{k}_{\parallel} \rho_{\parallel} = k_{\parallel} \rho_{\parallel} \cos(\varphi - \psi)$  and

$$\int_0^{\infty} x^2 \exp(-ax) dx = 2/a^3 \quad \text{for } a \in \mathbb{C} \text{ with } \text{Re}(a) > 0 \quad (3.47)$$

<sup>1</sup>Since  $B_0$  is an additional constant we will neglect it for simplicity reasons.

one can write Eq. (3.46) as<sup>2</sup>

$$W(\boldsymbol{\rho}_{\parallel}; z_0 - z') = \frac{1}{c_{11}} \left( \frac{\Delta a}{a} \right)^2 (\sigma^{(0)})^2 \times \sum_{s=1}^3 \frac{1}{2\pi^2} \int_0^{2\pi} d\varphi \frac{r_s(\varphi)}{[\alpha_s(\varphi)(z_0 - z') - i\rho_{\parallel} \cos(\varphi - \psi)]^3} \quad (3.48)$$

The next task is to determine a solution for the integral stated above (Eq. (3.48)). Since there is a cubic term in the denominator, it is hard to find an analytic solution. So one should do it numerically.

At first, another choice of constants  $R^2 = \rho_{\parallel}^2 + (z_0 - z')^2$  and  $R \cos(\theta) = z_0 - z'$  gives

$$[\alpha_s(\varphi)(z_0 - z') - i\rho_{\parallel} \cos(\varphi - \psi)]^3 = R^3 [\alpha_s(\varphi) \cos(\theta) - i \sin(\theta) \cos(\varphi - \psi)]^3$$

and the integrand of interest from Eq. (3.48) becomes

$$\begin{aligned} \int_0^{2\pi} d\varphi \frac{r_s(\varphi)}{[\alpha_s(\varphi)(z_0 - z') - i\rho_{\parallel} \cos(\varphi - \psi)]^3} &= \\ &= \frac{1}{R^3} \int_0^{2\pi} d\varphi \frac{r_s(\varphi)}{[\alpha_s(\varphi) \cos(\theta) - i \sin(\theta) \cos(\varphi - \psi)]^3} \\ &:= \frac{1}{R^3} I_s(\psi, \theta) \end{aligned} \quad (3.49)$$

which can be integrated numerically in principle, e.g., with the help of *mathematica*. But until now the values for  $\alpha_s$  and  $r_s$  are not present in a closed form, although, as mentioned previously, they can be obtained with arbitrary numerical precision (see appendix C, [Por77]).

To proceed, we now need an appropriate fit for the material parameters  $\alpha_s$  and  $r_s$  (see Eq. (3.45)). Therefore we try three different sets and choose the best, after evaluation. The superscripts which indicate the type of fit<sup>3</sup> are suppressed on the constants  $A, B, C$  to avoid confusion.

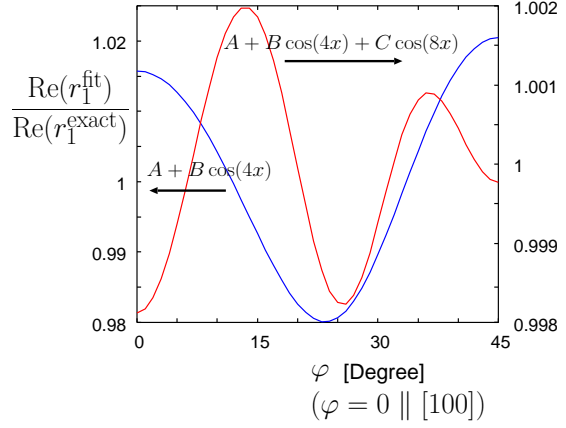
$$\begin{aligned} \alpha_s^{cs}(\varphi) &= A_s^\alpha + B_s^\alpha \cos(4\varphi) \\ r_{1,2}^{cs}(\varphi) &= A_{1,2}^r + B_{1,2}^r \cos(4\varphi) \\ r_3^{cs}(\varphi) &= A_3^r + B_3^r \sin^2(4\varphi) \end{aligned} \quad (3.50a)$$

$$\begin{aligned} \alpha_s^{c8}(\varphi) &= A_s^\alpha + B_s^\alpha \cos(4\varphi) + C_s^\alpha \cos(8\varphi) \\ r_s^{c8}(\varphi) &= A_s^r + B_s^r \cos(4\varphi) + C_s^r \cos(8\varphi) \end{aligned} \quad (3.50b)$$

<sup>2</sup>The condition  $\text{Re}(a) > 0$  is fulfilled for all material systems examined here.

<sup>3</sup>The author has chosen the superscripts with the intention that it should be self-explanatory. For the case that this fails: *cs* should mean something like ‘there appears a cosine and a sine’, *c4* should mean ‘there is a cosine with a period up to four’ ...

**Figure 3.4:** Ratio between fit and exact numerical results (blue line: Eq. (3.50a) and Eq. (3.50c), red line: Eq. (3.50b)). Material parameters of GaAs are chosen. This ratio is shown exemplarily for the real part of  $r_1^{(\cdot)}(\varphi)$ .



$$\begin{aligned}\alpha_s^{c4}(\varphi) &= A_s^\alpha + B_s^\alpha \cos(4\varphi) \\ r_s^{c4}(\varphi) &= A_s^r + B_s^r \cos(4\varphi)\end{aligned}\quad (3.50c)$$

All of these fits—even the last one—are very close to numerical data (Fig. 3.4). The detailed values for the fitting constants are listed in the appendix D.1. To decide which one of the introduced fits is useful for our purposes, we process the special case of the two-dimensional strain field since one of the strongest predictions to the solutions (both, the 3D and 2D case) is of course the consistency and that the solution of the 3D strain field must go continuously towards the 2D solution in the limit case  $z' \rightarrow 0$ .

### 3.3.2 The originating plane: $(z_0 - z') = 0$

With  $z_0 - z' = 0$ ,  $\mathbf{k}\boldsymbol{\rho} = k\rho \cos(\varphi - \psi)$  and  $\int f(\mathbf{k}_{\parallel}) d^2\mathbf{k}_{\parallel} = \int \int k f(k, \varphi) dk d\varphi$  Eq. (3.46) becomes

$$W(\boldsymbol{\rho}_{\parallel}; 0) = \frac{1}{c_{11}} \left( \frac{\Delta a}{a} \right)^2 (\sigma^{(0)})^2 \int_0^\infty \frac{dk_{\parallel}}{(2\pi)^2} k_{\parallel}^2 \int_0^{2\pi} d\varphi \sum_{s=1}^3 r_s(\varphi) e^{ik_{\parallel}\rho_{\parallel} \cos(\varphi - \psi)} \quad (3.51)$$

For  $\psi = 0$  this can be written in terms of Bessel-Functions which solve the differential equation

$$z^2 y'' + zy' + (z^2 - n^2)y = 0$$

and can be represented as

$$J_n(z) = \frac{(-i)^n}{\pi} \int_0^\pi \exp\{iz \cos \varphi\} \cos(n\varphi) d\varphi.$$

For all of the fitting schemes (Eq. (3.50a-3.50c)) the sum over  $r_s(\varphi)$  can be expressed as

$$\sum_{s=1}^3 r_s^{cs}(\varphi) = A_0 + B_0 \cos(4\varphi) + C_0 \sin^2(4\varphi) \quad (3.52a)$$

$$\sum_{s=1}^3 r_s^{c8}(\varphi) = A_0 + B_0 \cos(4\varphi) + C_0 \cos(8\varphi) \quad (3.52b)$$

$$\sum_{s=1}^3 r_s^{c4}(\varphi) = A_0 + B_0 \cos(4\varphi) \quad (3.52c)$$

with fitting constants  $A_0, B_0, C_0 \in \mathbb{R}$ . In the case of  $r_s^{c4}(\varphi)$  and  $r_s^{c8}(\varphi)$  these are the sums of real parts of the parameters used in Eq. (3.50b) and Eq. (3.50c). The complete list of parameters can be found in Sec. D.1, exemplarily for GaAs this would read

$$\sum_{s=1}^3 r_s^{c4}(\varphi) = A_0 + B_0 \cos(4\varphi) \quad \text{with}$$

$$A_0 = \sum_{s=1}^3 A_s^r = -2.01 \quad \text{and}$$

$$B_0 = \sum_{s=1}^3 B_s^r = -0.14 \quad .$$

In the simplest case for  $\psi = 0$  one obtains<sup>4</sup>

$$I_{2D}^{(\cdot)}(\psi = 0) := \int_0^\infty \frac{dk_{\parallel}}{(2\pi)^2} k_{\parallel}^2 \int_0^{2\pi} d\varphi \sum_{s=1}^3 r_s^{(\cdot)}(\varphi) e^{ik_{\parallel} \rho_{\parallel} \cos(\varphi-0)}$$

$$I_{2D}^{cs}(\psi = 0) = -\frac{1}{2\pi\rho_{\parallel}^3} (A_0 - 15B_0 + 32C_0) \quad (3.53a)$$

$$I_{2D}^{c8}(\psi = 0) = -\frac{1}{2\pi\rho_{\parallel}^3} (A_0 - 15B_0 + 63C_0) \quad (3.53b)$$

$$I_{2D}^{c4}(\psi = 0) = -\frac{1}{2\pi\rho_{\parallel}^3} (A_0 - 15B_0) \quad (3.53c)$$

Normally—of course— $\psi \neq 0$ , this makes things rather difficult. The results of the previous section do not help, because the condition of Eq. (3.47) is not fulfilled anymore.

<sup>4</sup>We choose the coordinate system such, that the  $x$ -axes is parallel to, e.g., the [100]-direction, and the angle  $\psi = 0 \Leftrightarrow \mathbf{r}_{\parallel} \parallel x$ .

However, after some analytical calculation one finds

$$I_{2D}^{(\cdot)}(\psi) := \int_0^\infty \frac{dk_{\parallel}}{(2\pi)^2} k_{\parallel}^2 \int_0^{2\pi} d\varphi \sum_{s=1}^3 r_s(\varphi) e^{ik_{\parallel}\rho_{\parallel} \cos(\varphi-\psi)}$$

$$I_{2D}^{cs}(\psi) = \frac{1}{2\pi\rho_{\parallel}^3} \left( -A_0 + 15B_0 \cos(4\psi) - \frac{1}{2}C_0 - \frac{63}{2}C_0 \cos(8\psi) \right) \quad (3.54a)$$

$$I_{2D}^{c8}(\psi) = \frac{1}{2\pi\rho_{\parallel}^3} (-A_0 + 15B_0 \cos(4\psi) - 63C_0 \cos(8\psi)) \quad (3.54b)$$

$$I_{2D}^{c4}(\psi) = \frac{1}{2\pi\rho_{\parallel}^3} (-A_0 + 15B_0 \cos(4\psi)) \quad (3.54c)$$

Since in Sec. 3.3.3 it will be found that  $r_{(\cdot)}^{c4}$  and  $\alpha_{(\cdot)}^{c4}$  is the fitting scheme of choice, we finally write down the elastic energy for the 2D case, combining Eq. (3.42), Eq. (3.51), Eq. (3.50c), and Eq. (3.54c):

$$E_{el}^{2D}(\mathbf{r}_{\parallel}; z = z_0) = \frac{h^S V^{(u)}}{c_{11}} \left( \frac{\Delta a}{a} \right)^2 (\sigma^{(0)})^2$$

$$\times \int_A d^2 \mathbf{r}'_{\parallel} \left( \frac{1}{2\pi\rho_{\parallel}^3} [-A_0 + 15B_0 \cos(4\psi)] \right). \quad (3.55)$$

### 3.3.3 The best fitting scheme

Comparing the results obtained in Sec. 3.3.1 and Sec. 3.3.2 we now can decide which fit (Eq. (3.50a-3.50c)) is best. Not only the smallest deviation from analytical results is decisive. Another (natural) claim is: values obtained for the 3D case should go continuously towards the analytical results for  $(z_0 - z') = 0$ .

The differences between the numerical results of the angle dependent part of the elastic energy (Eq. (3.48)) for a spherical angle of  $\Theta = 89.75^\circ$  and the corresponding analytical result (Eq. (3.54a-3.54c),  $\Theta = 90^\circ$ ) is shown in Fig. 3.5

$$\Delta E_{el}^{(\cdot)} := \sum_s I_s^{(\cdot)}(\psi, \Theta = 89.75^\circ) - I_{2D}^{(\cdot)}(\psi)$$

It is clear that both results should differ, but since we are looking for a smooth function the difference should vanish for small deviations in the spherical angle meaning

$$\sum_s I_s^{(\cdot)}(\psi, \Theta \rightarrow 90^\circ) = I_{2D}^{(\cdot)}(\psi)$$

Surprisingly the fit  $r_s^{c4}$  (Eq. (3.50c)) gives the smallest deviation. And furthermore, as can be seen in Fig. 3.6, the numerical result converges smoothly towards the analytical solution.

So for further investigations we will use the fitting scheme  $r_s^{c4}$  and  $\alpha_s^{c4}$  (see Eq. (3.50c)). It is not only the simplest but the best, too.

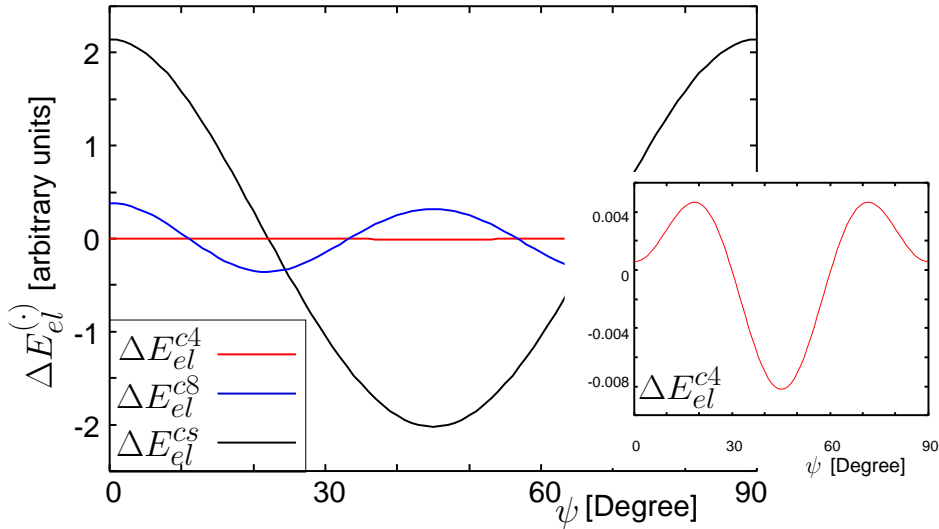


**Figure 3.5:** Difference between numerical and analytical results for the angle dependent part of the elastic energy density  $\Delta E_{el}^{(\cdot)} := \sum_s I_s^{(\cdot)}(\psi, \Theta = 89.75^\circ) - I_{2D}^{(\cdot)}(\psi)$ . Black line: fit function  $r_s^{cs}$ , blue line:  $r_s^{c8}$  red line:  $r_s^{c4}$  (see Eq. (3.50a-3.50c)). Inset: only enlargement of  $r_s^{c4}$  is shown. Material parameters of GaAs were used.

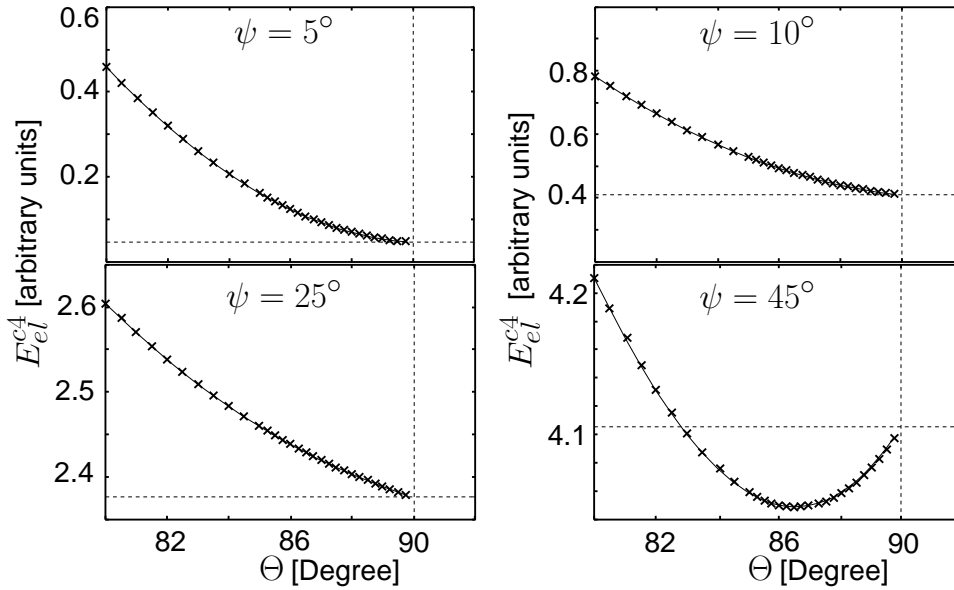


**Figure 3.6:** Elastic energy density as function of the spherical angle  $\Theta$ . Numerically calculated results (solid line) for different in-plane angles  $\psi$ . The dotted line marks the analytical result ( $\Theta = 90^\circ$ ). Material parameters of GaAs were used. Fit function:  $r_s^{c4}$  of Eq. (3.50c).

### 3.4 Final set of equations

To conclude here are suggested ways to treat the problem:

From the exact numerical solution for the Green's-tensor in  $k$ -space an analytical solution for the second derivative of Green's tensor in the *two-dimensional* real space was derived. The result for the second derivative of Green's tensor in the *three-dimensional* real space was found by numerical integration.

Having both results, the calculation of the elastic interacting energy is straightforward.

The equations for both cases are:

$$E_{el}^{2D}(\mathbf{r}_{\parallel}; z = z_0) = \frac{h^S V^{(u)}}{c_{11}} \left( \frac{\Delta a}{a} \right)^2 (\sigma^{(0)})^2 \quad (3.56)$$

$$\times \int_A d^2 \mathbf{r}'_{\parallel} \left( \frac{1}{2\pi \rho_{\parallel}^3} [-A_0 + 15B_0 \cos(4\psi)] \right)$$

$$E_{el}^{3D}(\mathbf{r}_{\parallel}; z = z_0) = \frac{V^{(u)}}{c_{11}} \left( \frac{\Delta a}{a} \right)^2 (\sigma^{(0)})^2 \quad (3.57)$$

$$\times \int_A \int_{-\infty}^{z_0} d^2 \mathbf{r}'_{\parallel} dz' \frac{1}{2\pi^2 R^3} \sum_{s=1}^3 I_s(\psi, \theta(\mathbf{r}'_{\parallel}, z')).$$

To reduce computation time, a lookup table is implemented, such that values of  $\sum_{s=1}^3 I_s(\psi, \theta)$  for  $\psi \in \{0, 1, \dots, 90\}$  and  $\theta \in \{0, 1, \dots, 90\}$  are stored permanently and a cubic interpolation is done at running time to evaluate  $I_s$  at arbitrary points.

$$E_{el}^{2D}(\mathbf{r}_{\parallel}; z = z_0) = \frac{h^S V^{(u)}}{c_{11}} \left( \frac{\Delta a}{a} \right)^2 (\sigma^{(0)})^2 \int_A d^2 \mathbf{r}'_{\parallel} W^{2D}(\mathbf{r}_{\parallel} - \mathbf{r}'_{\parallel}) \hat{\vartheta}(\mathbf{r}'_{\parallel}, 0) \quad (3.58)$$

$$E_{el}^{3D}(\mathbf{r}_{\parallel}; z = z_0) = \frac{V^{(u)}}{c_{11}} \left( \frac{\Delta a}{a} \right)^2 (\sigma^{(0)})^2$$

$$\int_A \int_{-\infty}^{z_0} d^2 \mathbf{r}'_{\parallel} dz' W^{3D}(\mathbf{r}_{\parallel} - \mathbf{r}'_{\parallel}; z - z') \hat{\vartheta}(\mathbf{r}'_{\parallel}, z'), \quad (3.59)$$

with interaction terms

$$\tilde{W}^{2D}(\rho, \psi) = \frac{1}{2\pi \rho_{\parallel}^3} [-A_0 + 15B_0 \cos(4\psi)] \quad \text{and} \quad (3.60)$$

$$\tilde{W}^{3D}(R, \psi, \theta) = \frac{1}{2\pi^2 R^3} \sum_{s=1}^3 I_s(\psi, \theta), \quad (3.61)$$

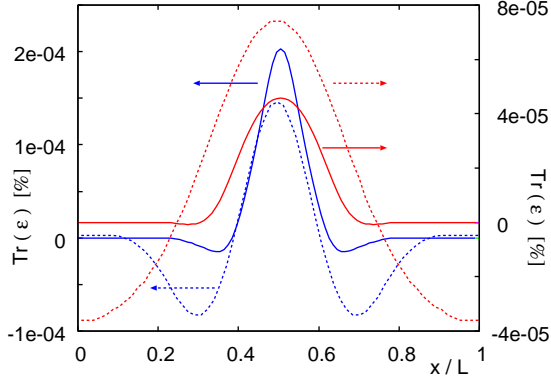


**Figure 3.7:** Trace of the strain tensor computed with the method developed here (solid lines) and an atomistic approach (dashed lines) [Ham06]. The strain at the relaxed surface of a plate-like circular shaped island with a radius of 10 lattice sites (l.s.) is shown. Distance between the surface and base of the buried sample structure is  $d = 9$  l.s. (red) and  $d = 17$  l.s. (blue). The position in [100]-direction is given by  $x$  and  $L \times L = 100 \times 100$  l.s. is the system size. Material parameters of GaAs were used.

where  $\hat{\vartheta}(\mathbf{r}'_{\parallel}, z')$  is a shape function being unity if  $(\mathbf{r}'_{\parallel}, z')$  is inside an inclusion and zero elsewhere.<sup>5</sup> The tilted and non-tilted interaction terms can be easily transformed into each other via a variable transformation.

In the following kinetic Monte Carlo simulations (Ch. 5, and 6) we will use

$$E_{str}(\mathbf{r}_{\parallel}) = E_{el}^{2D}(\mathbf{r}_{\parallel}; z = z_0) + E_{el}^{3D}(\mathbf{r}_{\parallel}; z = z_0) \quad (3.62)$$

in the Arrhenius term of Eq. (2.20) for calculating the strain energy contribution acting on a moving adatom at the surface, i.e., located at  $(\mathbf{r}_{\parallel}, z_0)$ .

Since the above equations give access to the trace of the strain tensor [cf. Shc98b, Appendix B], i.e., the hydrostatic compression corresponding to the volume deformation, as a quick illustration for the accuracy of the continuum method developed here, a comparison with an atomistic quantum-mechanical approach developed by Th. Hammerschmidt will be carried out [Kun06]. The latter is a recently developed parametrization of an analytical many-body potential of the Abel-Tersoff type [Ham06]. It reproduces many properties of Ga, As, In, GaAs, and InAs bulk structures, and of GaAs and InAs surfaces, as obtained from experiment or density-functional theory calculations, with good overall accuracy. The elastic constants are reproduced within 1% error and detailed tests showed a good description of both linear and non-linear elastic response of biaxially strained InAs.

Although it is known that for low strain both methods must agree, while for large strains, namely inside quantum dots and around its interface, the results differ [Pry98], we carry out this calculation to be sure that our computations are correct. In Fig. 3.7 the strain tensor of a plate-like circular shaped island with a radius of 10 lattice sites (l.s.) is shown. The distance between the surface and base of the buried sample is  $d = 9$  and 17 l.s., respectively.

<sup>5</sup>In case the impatient reader skipped the sections before, as depicted in Fig. 3.3 on page 40, the following notation is used:  $\rho_{\parallel} = \mathbf{r}_{\parallel} - \mathbf{r}'_{\parallel}$ ,  $\rho = \|\rho_{\parallel}\|$ ,  $\psi$  is the angle between  $\rho_{\parallel}$  and the [100]-direction,  $R = \|\mathbf{r} - \mathbf{r}'\|$  and  $\theta$  is the angle between the growth direction  $z$  and  $\mathbf{r} - \mathbf{r}'$ .

As can be seen, both models give qualitatively nearly the same results for  $d = 9$  l.s. The small quantitative differences can be attributed to small differences in the grid which was used. For very low strain ( $d = 17$  l.s.) relatively large discrepancies between the two models can be seen. They are connected to the convergence criteria of the atomistic calculation. In this approach it is assumed that the values are stable, if the energy acting on an atom is lower than  $10^{-3}$  eV. Decreasing this value, in principle, would allow a more exact calculation, but is not feasible due to the dramatical increase of the computational effort.

One further point should be added. On the atomistic scale, other methods might be more exact but they are, by far, not that computationally efficient and fast. While the calculations of the atomistic method in Fig. 3.7 took several days, our method was able to produce the results in several minutes. For later calculations it is of high importance that strain fields of arbitrary structures can be computed very fast.

### 3.5 Isotropic approximation

For the sake of completeness, here in short a possibility to calculate the strain field in the isotropic approximation will be sketched [Mei02a; Mei03b; Mei03a].

The displacement field  $\mathbf{u}(\mathbf{r})$  generated by the forces  $\mathbf{F}$  for isotropic media satisfies the inhomogeneous differential equation [Lan70]

$$\frac{3\lambda + 2\mu}{2(1 + \mu)} \left( \Delta \mathbf{u} + \frac{1}{1 - 2\mu} \nabla(\nabla \cdot \mathbf{u}) \right) = \mathbf{F}. \quad (3.63)$$

Here, Lamé coefficients  $\lambda$  and  $\mu$  are used. Also common is the use of Poisson's ratio  $\nu$  which is connected to the Lamé coefficients via

$$\nu = \frac{\lambda}{2(\lambda + \mu)} \quad (3.64)$$

in addition to the shear modulus  $\mu$ .

A solution to this equation is to be found for the special case known as Ceruti's problem [Saa74] of a tangential force acting on the boundary of a semi-infinite solid. For the solution two potentials have to be defined: Lamé's strain potential and Galerkin's vector potential. Each of the potentials is a solution to Eq. (3.63).

According to Helmholtz's theorem, any vector function  $\mathbf{u}$  can be written as a sum of terms resulting from a scalar and a vector potential  $\Phi$  and  $\Psi$ , respectively.

$$\mathbf{u} = \nabla\Phi + \nabla \times \Psi, \quad \text{with} \quad \nabla \cdot \Psi = 0. \quad (3.65)$$

If one chooses  $\Delta\Phi = \text{const.}$  and  $\Psi = 0$ , the scalar function  $\Phi$  is called Lamé strain potential and it is easy to show that any harmonic function  $\Phi$  can be used to satisfy Eq. (3.63) with

$$\mathbf{u} = \frac{1}{2\mu} \nabla\Phi, \quad (\mu = \text{const.}). \quad (3.66)$$

Furthermore one can define a vector potential  $\mathbf{V}$  that is connected to the displacement field by

$$2\mu \mathbf{u} = 2(1 - \nu)\Delta\mathbf{V} - \nabla(\nabla \cdot \mathbf{V}). \quad (3.67)$$

This, again, is a general solution to the homogeneous Eq. (3.63), if the Galerkin vector  $\mathbf{V}$  is a biharmonic function, since the substitution of Eq. (3.67) in Eq. (3.63) gives  $\Delta(\Delta\mathbf{V}) = 0$ .

To solve Cerruti's problem, a special choice for  $\Phi$  and  $\mathbf{V}$  is made

$$\Phi = \frac{C x}{r + z}, \quad \mathbf{V} = \begin{pmatrix} A r \\ 0 \\ B x \ln(r + z) \end{pmatrix}, \quad (3.68)$$

and Eqs. (3.66) and (3.67) are superponed as

$$4\mu \mathbf{u} = \nabla\Phi + 2(1 - \nu)\Delta\mathbf{V} - \nabla(\nabla \cdot \mathbf{V}). \quad (3.69)$$

to give the solution of the homogeneous Eq. (3.63).

By using a generalized Hooke's law, which relates the displacement field  $\mathbf{u}$  defined by the strain tensor components  $\varepsilon_{ij}$  to the stress tensor components  $\sigma_{ij}$ , the constants  $A$ ,  $B$  and  $C$  can be determined by the conditions of vanishing stress at the surface for  $\sigma_{zz}$  and  $\sigma_{yz}$ , while on any horizontal plane at depth  $z$  from the surface the sum of all forces along the  $x$ -axis must balance  $\mathbf{F}$ , i. e.:

$$\int_{-\infty}^{\infty} \int_{-\infty}^{\infty} \sigma_{xz} dy dx = 0. \quad (3.70)$$

One finds for the constants  $A$ ,  $B$  and  $C$ :

$$A = \frac{|\mathbf{F}|}{4\pi(1 - \nu)}, \quad B = \frac{|\mathbf{F}|(1 - 2\nu)}{4\pi(1 - \nu)}, \quad C = \frac{|\mathbf{F}|(1 - 2\nu)}{2\pi}. \quad (3.71)$$

Now, the displacements can be calculated:

$$\begin{aligned} u_x &= \frac{|\mathbf{F}|}{4\pi\mu r} \left[ 1 + \frac{x^2}{r^2} + (1 - 2\nu) \left( \frac{r}{r + z} - \frac{x^2}{(r + z)^2} \right) \right] \\ u_y &= \frac{|\mathbf{F}|}{4\pi\mu r} \left[ \frac{xy}{r^2} - \frac{xy(1 - 2\nu)}{(r + z)^2} \right] \\ u_z &= \frac{|\mathbf{F}|}{4\pi\mu r} \left[ \frac{xz}{r^2} + \frac{x(1 - 2\nu)}{r + z} \right]. \end{aligned} \quad (3.72)$$

This corresponds to the explicit form of the Green's tensor at  $z = 0$ :

$$\begin{aligned}
G_{xx}(x - x', y - y') &= \frac{1}{2\pi\mu r^3} [(\nu - 1)(y - y')^2 - (x - x')^2] \\
G_{yy}(x - x', y - y') &= \frac{1}{2\pi\mu r^3} [(\nu - 1)(x - x')^2 - (y - y')^2] \\
G_{xy}(x - x', y - y') &= \frac{1}{2\pi\mu r^3} [-\nu(x - x')(y - y')] \\
&= G_{yx}(x - x', y - y')
\end{aligned} \tag{3.73}$$

The components of the strain can be calculated using the strain-displacement relations

$$\varepsilon_{ij} = \frac{1}{2} \left( \frac{\partial u_i}{\partial x_j} + \frac{\partial u_j}{\partial x_i} \right). \tag{3.74}$$

The resulting expressions simplify considerably if the  $z$ -dependence is neglected by setting  $z = 0$ , and  $r = \sqrt{(x^2 + y^2)}$  is used:

$$\begin{aligned}
\varepsilon_{xx} &= \frac{|\mathbf{F}|x}{2\pi\mu r^5} [-x^2 + y^2(3\nu - 1)] \\
\varepsilon_{yy} &= \frac{|\mathbf{F}|x\nu}{2\pi\mu r^5} [x^2 - 2y^2] \\
\varepsilon_{zz} &= \frac{|\mathbf{F}|x\nu}{2\pi\mu r^3} \\
\varepsilon_{xy} &= \frac{|\mathbf{F}|y}{4\pi\mu r^5} [x^2(-1 - 4\nu) + y^2(2\nu - 1)] \\
\varepsilon_{xz} &= \varepsilon_{yz} = \varepsilon_{zx} = \varepsilon_{zy} = 0.
\end{aligned} \tag{3.75}$$

The force  $|\mathbf{F}|$  is used as a fit parameter to adjust the strain energy to appropriate values; it is of the order of some  $10^{-9}\text{N}$ .

Now, of course, the strain field has to be translated into an energy correction term to be used in the Monte Carlo simulation, see Eq. (2.19). This derives from the general definition of the strain energy density [Lan70]:

$$E_{str} = \frac{1}{2} \sum_{ij} \varepsilon_{ij} \sigma_{ij} \tag{3.76}$$

and with  $\sigma_{ij} = 2\mu\varepsilon_{ij} + \delta_{ij}\lambda\sum_n \varepsilon_{nn}$  one finds

$$E_{str} = \frac{\lambda}{2} \left( \sum_i \varepsilon_{ii} \right)^2 + \mu \sum_{ij} \varepsilon_{ij}^2. \tag{3.77}$$

This equation is valid for the isotropic case only. Unfortunately, most crystalline structures have a more or less pronounced anisotropic character and the elastic properties even for the simplest anisotropic case, the cubic crystal, are given by three material parameters  $c_{11}$ ,  $c_{12}$  and  $c_{44}$  instead of the two Lamé coefficients. However, often for cubic crystals average Lamé coefficients can be introduced via [Pim98]

$$\lambda = \frac{1}{5} (2c_{11} + 3c_{12} - 4c_{44}) \quad (3.78)$$

$$\mu = \frac{1}{10} (8c_{44} + c_{11} - c_{12}) . \quad (3.79)$$

The equivalence of the above presented isotropic formulation and an anisotropic model which is presented in short in the Appendix A was shown in [Mei02a]. Also in Appendix A the reader can find the proof for the equivalence of the two anisotropic models, the one developed here in the section before and another one suggested by V. A. Shchukin. The latter for example was used in [Mei01b].

## 3.6 Summary

The calculation of the elastic strain field in the framework of elasticity theory is an important ingredient in the kinetic Monte Carlo simulations which will follow in the next chapters (Ch. 5, Ch. 6). But it can be used as a single tool for calculating strain properties of arrays of quantum dots, as well (Ch. 4).

Therefore in this chapter the derivation of the three-dimensional anisotropic strain field was shown in detail. The formalism developed here offers a fast approach for calculating the elastic interaction energy of arbitrarily shaped islands, where only the material dependent elastic constants enter.

Comparison of our computations with an atomistic approach were carried out and showed good agreement. The exactness of our calculations also will be seen in the comparative results, which will be given in the next chapters.



# Chapter 4

## Elastic strain field of sample structures and patterns

During the growth process the adatoms which are deposited on the surface form nuclei, which build up islands at a later stage. The adatom movement and the process of island formation, i.e., attachment and detachment of adatoms, is influenced by the strain field, induced by already existing islands. So, for instance, a preferred spatial ordering or an ordering in size and shape can be understood as a strain driven process. Considering the growth of QD stacks, already the very first adatoms approaching the surface move under the influence of a strain field, which comes from the previously grown structures beneath.

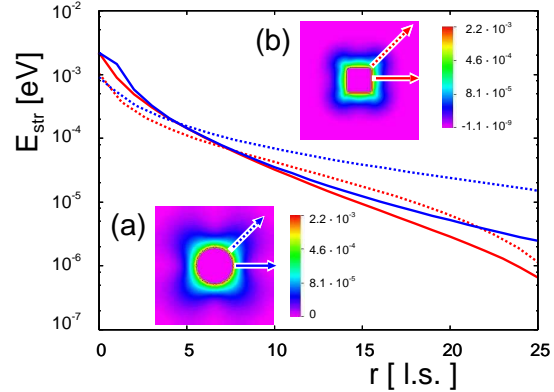
Before we proceed to kinetic Monte Carlo growth simulations with incorporated strain field, in this chapter the anisotropic strain field (developed in Ch. 3, see in particular Sec. 3.4, p. 48) of various structures and patterns itself will be examined and discussed.

### 4.1 Strain field in a single layer

At first the strain field in a single monolayer will be examined, that is, the interaction energy of islands and adatoms, being in the same plane. In general, cubic materials like InAs show a fourfold symmetry in their anisotropic strain field. The directional dependence due to the anisotropic material character is clearly to be seen (Fig. 4.1). The absolute value of the elastic energy in the  $x$ -direction ( $[100]$ , elastically soft direction) decays faster than in the  $[110]$ -direction (elastically hard). A higher value of the strain energy causes higher adatom mobilities due to a lowering of the binding energies (see discussion in Sec. 5.2). In general, this prevents Ostwald ripening, but is here moreover directionally dependent.

In some experiments spatial ordering of islands along a preferred direction was reported. As one example [Sch98a] should be mentioned. Self-organized  $\text{Si}_{1-x}\text{Ge}_x$  islands were grown on Si using liquid phase epitaxy (LPE). Interestingly, in the inter-

**Figure 4.1:** Elastic energy of a monolayer height island. (a, blue lines): circular island with radius of 15 atoms and (b, red lines): square island,  $20 \times 20$  atoms. Sample size  $100 \times 100$  atoms. The curves represent cross sections of the elastic energy along the  $[100]$  (dotted lines) and  $[110]$ -direction (solid lines) The  $x$ -axes is chosen such, that the cross sections start at the island edge.



mediate coverage regime nearly all islands were found to be aligned along the  $[100]$ -direction, building up extended chains. Growing samples with a lower coverage, first the island distribution seems to be random, but a closer look shows island-dimers and a few island-trimers, again aligned in the  $[100]$ -direction. This behavior can be understood as a strain driven process and can be reproduced using a KMC simulation incorporating an anisotropic strain field [Mei01b]. Similar behavior can be expected also with simulations incorporating the strain field developed in this work, as an ordering along the  $[100]$ -direction is slightly favorable (Fig. 4.1). It should be mentioned that, however, for reproducing these results appropriate growth conditions have to be applied, e.g., very long simulation times.

By comparing rectangular vs. disk shaped structures as is done in Fig. 4.1 one can see the influence of an asymmetric edge of the sample. While the anisotropic material character, the ‘tongues’ of the strain field towards  $[110]$ , are easy to be seen on the disk shaped sample (Fig. 4.1 (a), dotted line), this feature is slightly suppressed in the rectangular one.

## 4.2 Strain field of buried structures

### 4.2.1 Interaction energy of single point defects

In this section we discuss the features of the strain field which can be deduced by the investigation by one single point-like inclusion of material A in a matrix of material B. For theoretical considerations the type of material A can be chosen arbitrarily, taking into account the homogeneous moduli approximation (Sec. 3.2, [Kha83]). For a direct comparison of our results, Ref. [Hol99] offers some theoretically obtained data for different parent materials (B). As grid for our calculations we have used the lattice constant of the parent material. These are in particular  $a_{\text{Si}} = 0.543$  nm,  $a_{\text{GaAs}} = 0.565$  nm, and  $a_{\text{ZnSe}} = 0.567$  nm for Si, GaAs and ZnSe respectively (see Appendix D.2, [Lid97; Hel75]). This means, that the conversion from, i.e., ten grid points (lattice sites, l.s.) in the GaAs material system to nm would give  $10a_{\text{GaAs}} = 5.65$  nm.

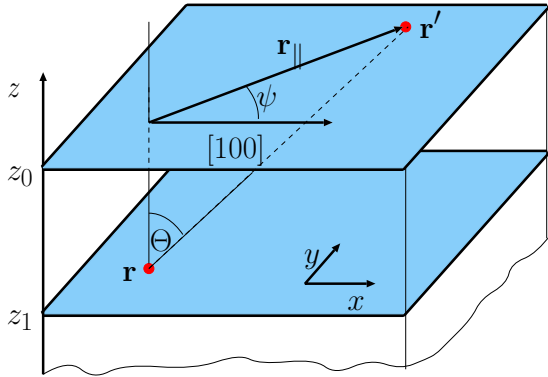


**Figure 4.2:** Illustration of the notation used. Two point-like quantum dots (red points) are located at  $\mathbf{r}$  and  $\mathbf{r}'$ .

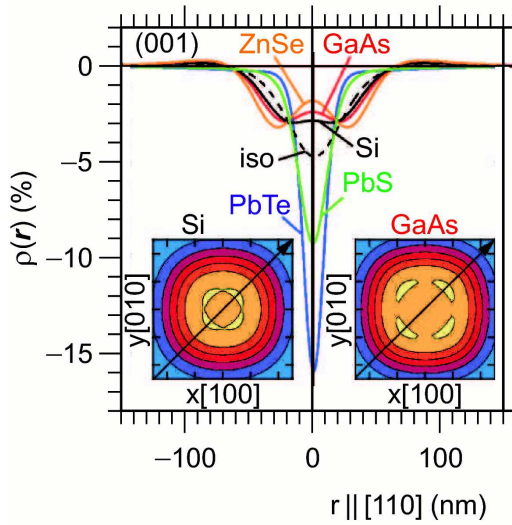


**Figure 4.3:** Normalized elastic energy distribution  $\rho(x, y)$  on the surface above a strained self-assembled quantum dot of arbitrary material at 50 nm below the surface for various matrix materials and for the (001), surface orientation, calculated within the framework of elasticity theory. The curves represent cross sections of  $\rho$  in the [110]-direction. The dashed line represents elastically isotropic materials. Insets: 2D contour plots with  $-50 \leq (x, y) \leq +50$  nm and with a 0.5% step width between contours. The yellow areas correspond to the minima of  $\rho$ . Taken from Ref. [Hol99].

The minimum of the elastic strain energy for a buried strain source (at the depth of 50 nm) was found for angles  $\Theta \approx 16^\circ$ ,  $23^\circ$  and,  $32^\circ$  for Si, GaAs, and ZnSe, respectively (see Fig 4.3). The same situation is considered in Fig. 4.4. The strain energy computed with our model is shown as a function of the in-plane radius  $r_{\parallel}$  (Fig. 4.4 (a)) and as density plots in the plane spanned by the [100] and [010]-direction for different materials (Fig. 4.4 (c–e)). The interaction term  $W^{3D}$  as given in Sec. 3.4, Eq. (3.57) is shown in Fig. 4.4 (b). A comparison of the curves of Fig. 4.3 and Fig. 4.4 (a) and (b) illustrates the meaning of the ‘normalized elastic energy’ as is used in [Hol99]. This term refers to an expression similar to the ‘interaction term’ of this thesis. The position of the strain field minima and maxima is, however, the same for both quantities. The strongly pronounced minimum can be found at  $\Theta \approx 25^\circ$  ( $\psi = 45^\circ$ ) for GaAs. If we choose other material parameters we find these minima for  $\Theta \approx 19^\circ$ ,  $25^\circ$  and,  $33^\circ$  for Si, GaAs, and ZnSe, respectively. With respect to the in-plane radius, for the different material systems Si, GaAs and ZnSe we find the minima to be at  $r_{\parallel} \approx 17, 23, 30$  nm, respectively (Fig. 4.4). These values are in good

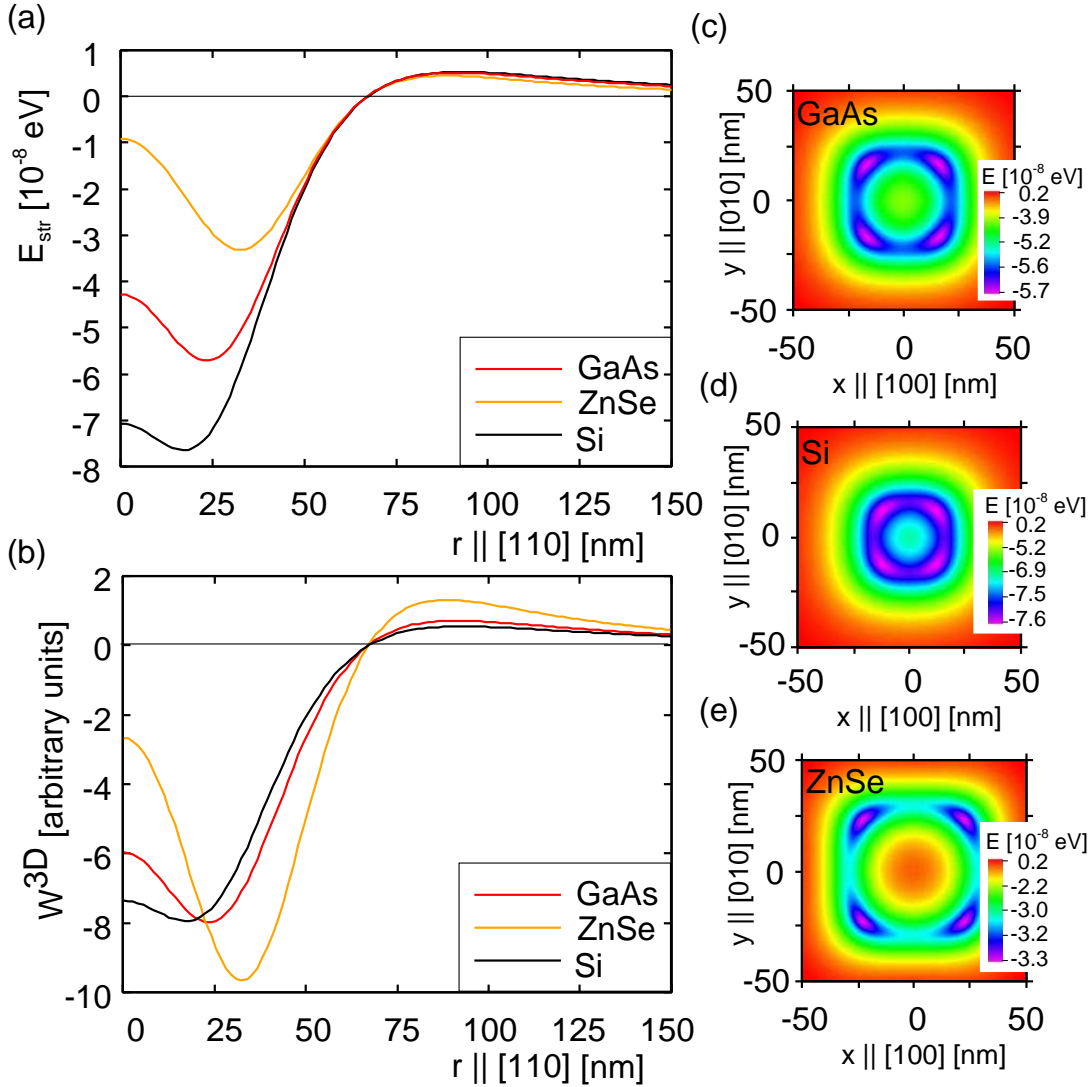


**Figure 4.4:** Elastic energy of a buried dot located 50 nm below the surface. The elastic energy  $E_{str}$  and the interaction term  $W^{3D}$  (see Eq. (3.57)) along the  $[110]$ -direction is shown for different materials in (a) and (b), respectively. The density plots (c–d) show the elastic energy  $E_{str}$  in the plane spanned by the  $[100]$  and the  $[010]$ -direction.

agreement with [Hol99], too (cf. Tab. 4.1).

The above discussed behavior strongly depends upon the specific material. The main features are due to the anisotropic material character which in cubic materials

	$\Theta$ [Degree]		$r_{\parallel}$ [nm]	
	[Hol99]	this report	[Hol99]	this report
Si	16	19	18	17
GaAs	23	25	22	23
ZnSe	32	33	30	30

**Table 4.1:** Comparison of the results obtained in this work with [Hol99]. Listed are the spherical angle  $\Theta$  and in-plane radius  $r_{\parallel}$  in [110] direction, where the minima of elastic energy is found. The strain source is buried at about 50 nm.

can be quantified by the anisotropy ratio<sup>1</sup>

$$A = \frac{2c_{44}}{c_{11} - c_{12}}, \quad (4.1)$$

with  $A = 1$  corresponding to isotropic materials. Very large values for  $A$  can be found in the II-VI compounds, for example  $A = 2.74$  for ZnSe. Whereas in III-V compounds  $A$  is somewhat lower, ranging from 1.82 to 2.08 for GaAs and InAs. In contrast to that, for Si and Ge  $A = 1.56$  and 1.66 respectively. (For a more complete list cf. Sec. D.2, p. D.2.) Generally, for semiconductor materials with diamond or zinc-blende structure having the chemical bonds in the [111]-direction, the elastically hard direction is along the [111]-direction, and the elastically soft direction is [001]. Here,  $A > 1$  is valid.

In contrast to that, for rock salt materials, elastic hard and chemical bond directions are along [001] and elastic soft along [111], with  $A < 1$ .

As can be seen in Fig. 4.4, with increasing anisotropy the depth of the elastic minimum increases and if the anisotropy exceeds a critical value (Fig. 4.3) the minimum located directly above the point source splits into four side minima. As will be also discussed in the following sections, these side minima are partly responsible for the strain mediated *anticorrelated* growth of QDs.

We can conclude that even with the approximation for  $\alpha_S$  and  $r_S$  used in this report (see Eq. (3.50a) on page 43), the qualitative three-dimensional behavior of the elastic strain energy *and* properties resulting from the different character of the material systems, are both represented in our model in a very good manner and coincide with the findings in [Hol99].

As a final remark in this section it should be underlined that here a new feature of the strain field developed in this work appeared for the first time. In previous strain field models of our group [Sch98b; Kun00; Mei01c; Mei01b; Mei03b; Mei03a] the strain energy was strictly positive  $E_{str} > 0$ . Therefore it was responsible for reducing the binding energy resulting in a faster diffusion (see Sec. 2.4, p. 21, Eqs. (2.19) and (2.20)). Here both possibilities—*positive and negative* values for the strain energy—may occur. They refer to compressive and tensile strained regions respectively, giving

<sup>1</sup>In other references the dimensionless parameter  $\xi = (c_{11} - c_{12} - 2c_{44})/c_{44}$  is used. Here the elastic isotropic medium corresponds to  $\xi = 0$ , and in typical semiconductors  $\xi < 0$  and  $|\xi| \approx 1$ . The relation with  $A$  is  $A = 2/(\xi + 2)$ .

rise to repulsive and attractive regions for the adatoms, influencing the location of favorable nucleation sites. For a more detailed discussion see Sec. 5.2, p. 76.

### 4.2.2 Shape and height dependence—one single inclusion

First of all we study the dependence of the resulting strain field at the free (growth) surface on the shape of inclusions. Therefore in Fig. 4.5 we compare the strain field of three different three-dimensional structures, a half sphere, a platelet and a pyramid. All these shapes occur in self-assembled QDs grown in experiments.

For large spacer layer thicknesses  $d$  the shape of the strain field in the growth surface does not depend very much on the shape of the structure. Only the side maxima of the platelet shaped island are different from that of the two other input sample structures, since the platelet is a highly non-symmetric pattern, having a very large lateral extension compared to its height. Therefore the behavior even at larger distances is not at all comparable to a point-like inclusion, whereas the sphere as well as the pyramid are more compact, such that the orientation of the strain field of these sample structures is like that of a single point.

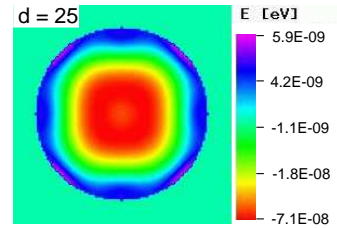
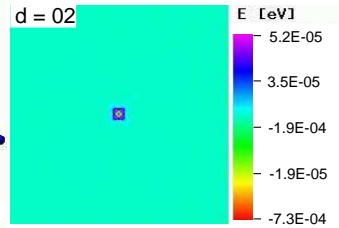
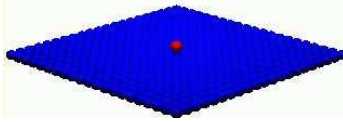
The absolute values of the energy are following the rule of thumb that the strain field is proportional to the volume of the structure. In the solid-on-solid model, which is used in this work, the platelet (pyramid/half sphere) are modeled within a grid of the length of one unit cell of GaAs, such that the volume is about 450 (2400/19300) lattice sites cubed. The values of the strain field differ in one order of magnitude, just as the volume does.

Another interesting question is the behavior of the strain field if one tries to induce a symmetry breaking. For instance, by changing the orientation of the facets of the observed structure. Fig. 4.6 shows a situation like that. The strain field of pyramids with a base length 9 and a height of 6 lattice sites, having its bases oriented along the [100]-direction plus the angle  $\gamma$ . The behavior of the strain field does not follow the orientation of the facets. Instead the strongly pronounced features remain at their position even for small distances between the sample and the top layer.

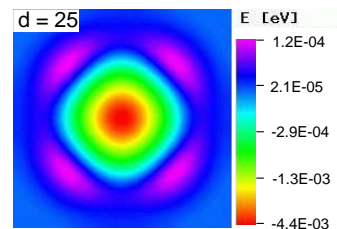
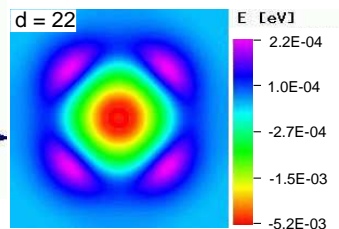
Fig. 4.7 shows an example of ‘successful’ symmetry breaking. The strain field of a buried platelet is shown. It differs strongly from the symmetry of the lattice which shows up for point defects, since the ratio between height and width of the sample is far from being unity—of course therefore no point-like behavior can be expected. The side maxima of the strain field are rotated by 45 degrees with respect to the [110] crystallographic direction which governs the side maxima for point defects, half spheres, and pyramids.

input sample structures

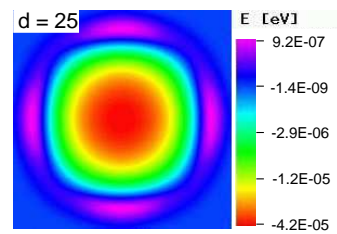
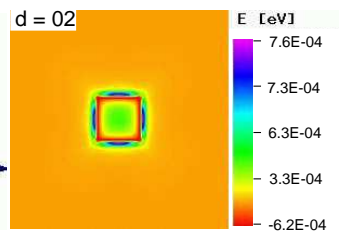
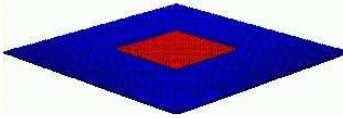
point defect,  
length 1 l.s.  
height 1 l.s.



half sphere,  
radius 21 l.s.



platelet,  
base length 21 l.s.  
height 1 l.s.



pyramid,  
base length 21 l.s.  
height 14 l.s.

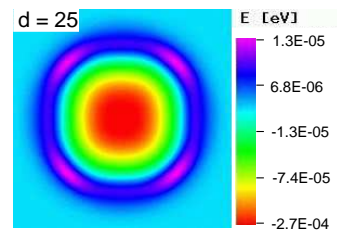
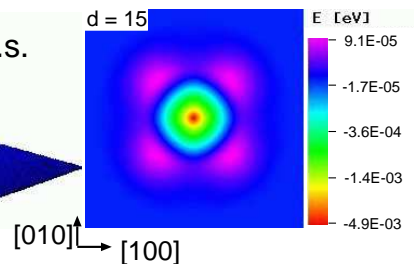
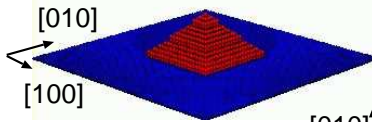


**Figure 4.5:** Elastic energy of various sample structures (depicted in the left column), buried directly beneath the surface (middle column) and buried at a depth of  $d = 25$  l.s. (right column). The energy distribution in the growth surface at  $z = z_0$ , where the base of the structure is at  $z = z'$  and the thickness of the spacer layer  $d = z_0 - z'$ . The calculations were done with a lateral energy cut-off at radii of  $r_{\parallel}^{\text{cut}} = 40$  l.s. Material parameters of GaAs were used.

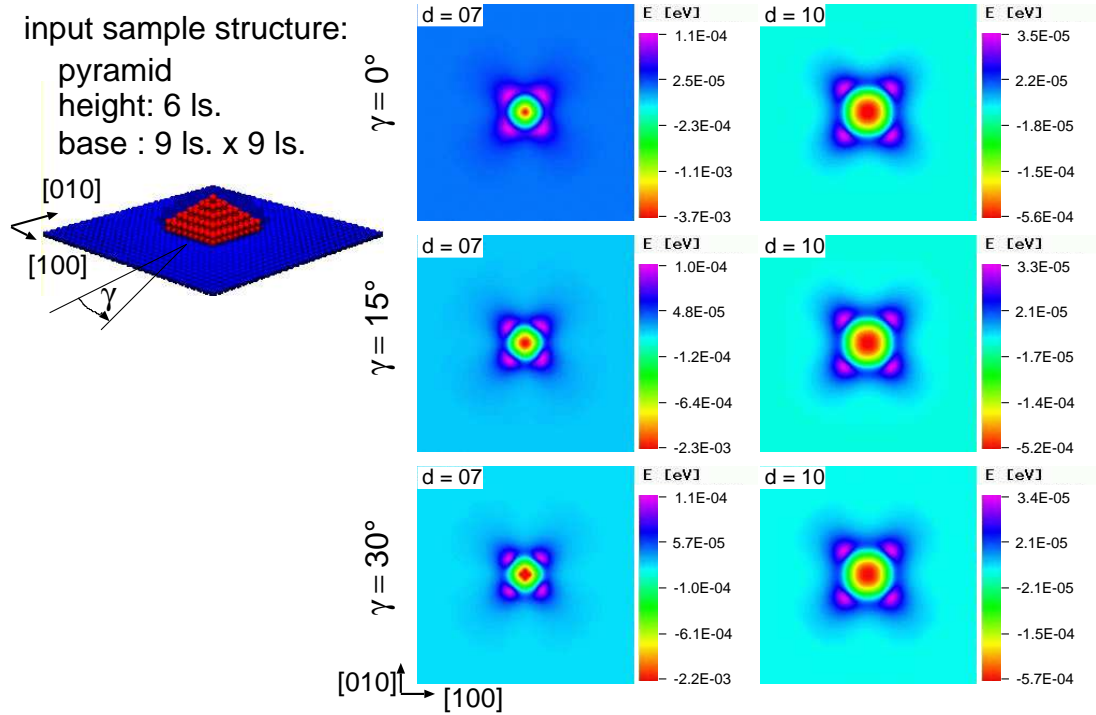
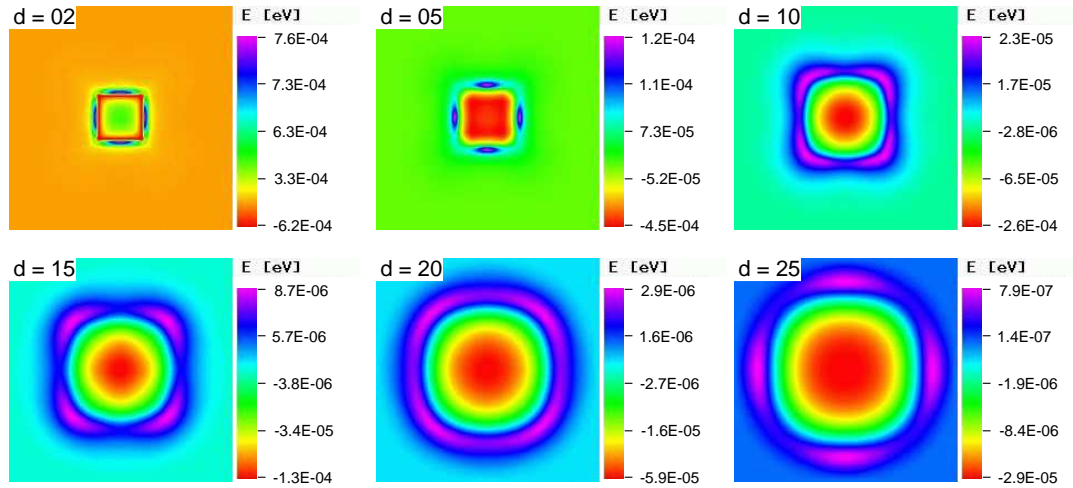


**Figure 4.6:** Elastic energy of a pyramid buried at 7 l.s. (middle column) and 10 l.s. (right column) beneath the surface with respect to the orientation of its base.  $\gamma$  denotes the angle between the  $[100]$  direction and the orientation of the base. The calculations were done with a lateral energy cut-off at radii of  $r_{\parallel}^{\text{cut}} = 40$  l.s. Material parameters of GaAs were used.

input sample structure:

(a) platelet with base of 21 l.s. x 21 l.s., height 1 l.s.



(b) point defect with length 1 l.s., height 1 l.s.

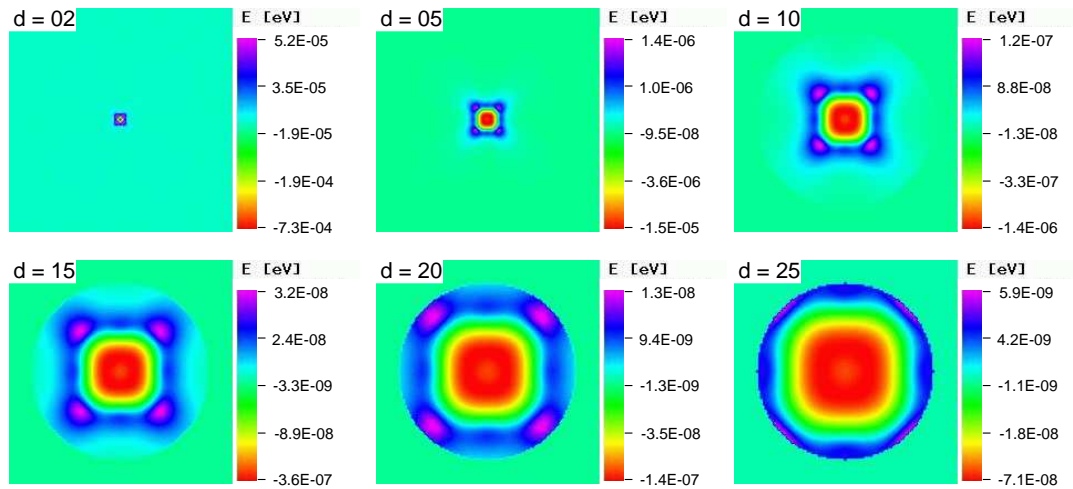


**Figure 4.7:** Elastic energy of a platelet (a) and a point defect (b) buried at depths of 2, 5, 10, 15, 20 and 25 l.s. The calculations were done with a lateral energy cut-off at radii of  $r_{\parallel}^{\text{cut}} = 40 \text{ l.s.}$  Material parameters of GaAs were used.

### 4.2.3 Periodic arrays of point-like inclusions

As previously mentioned, the minimum of the elastic energy—corresponding to a maximum of the tensile strain and therefore to an attractive potential—can be found under a certain polar angle  $\theta = \theta_{\min}$  in the  $[110]$ -direction (cf. Fig. 4.2). The opposite case, the angle under which a repulsive potential due to compressive strain can be found (the side maxima), also lies in the  $[110]$ -direction, and will be denoted by  $\theta_{\max}$ . (This statement is not generally true, but of course with respect to the material systems examined here, namely GaAs, Si, and ZnSe.) Since the strain field has a direct impact on the hopping barriers of the adatoms (Sec. 2.4, Eq. (2.20)) they can serve as region of favorable nucleation. For a detailed discussion on the influence of the strain field on the adatom movement see Sec. 5.2.

In this section we will calculate the strain field not only of *one* point defect, but rather of an array of point defects to clarify the behavior of overlapping strain fields. To do this, in the following very compact pictures will be presented, showing the propagation of the strain field (Fig. 4.9, Fig. 4.10). It seems reasonable to present to the reader a detailed explanation of the illustrations to avoid misinterpretation.

We calculate the elastic strain field of an given structure located at  $z = z'$  on the relaxed growth surface at  $z = z_0$ , with varying spacer layer thickness  $d = z_0 - z' = 0, a_{\text{GaAs}}, 2a_{\text{GaAs}}, \dots$ , where  $a_{\text{GaAs}} = 0.565$  nm is the lattice constant of the parent material (GaAs). Since for each value of  $d$  only the growth surface of the sample is of interest, we combine all relaxed top layers into one single image (Fig. 4.8). As grid of

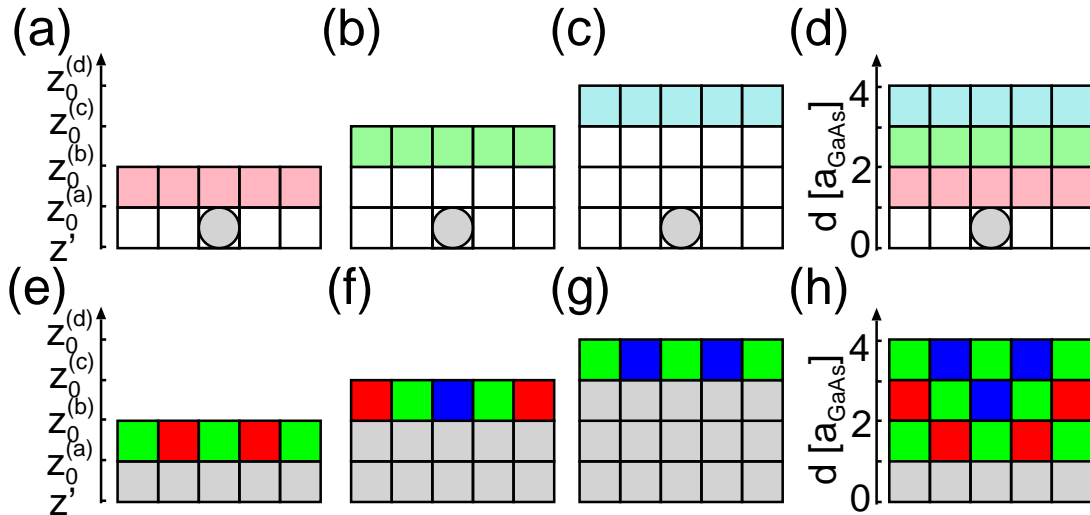


**Figure 4.8:** Schematic illustration of the density plots in Fig. 4.9, Fig. 4.10 and following figures. A given structure at  $z = z'$  is overgrown with a spacer of varying thickness (a–c) and only the (relaxed) top layer of each sample, which is located at  $z = z_0$ , is shown in dependence of the spacer layer thickness  $d = z_0 - z'$  (d). In the lower row (e–h) some features (red, green, blue) are introduced for illustrative purposes.

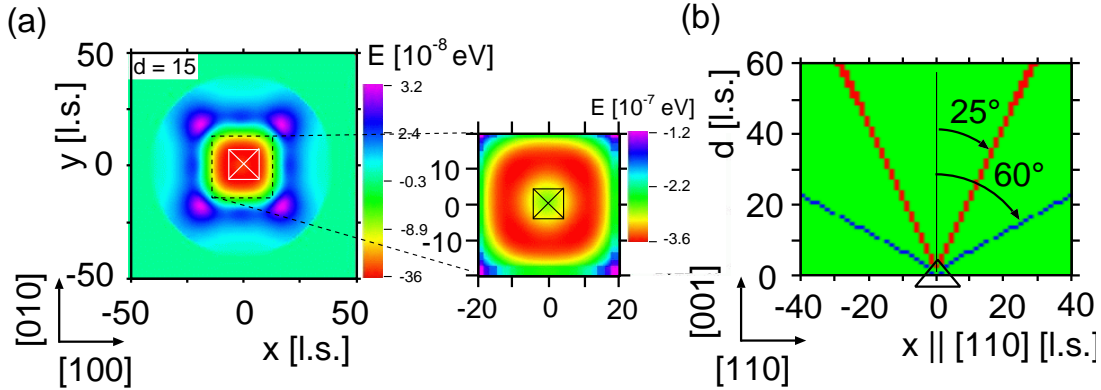


**Figure 4.9:** Elastic energy of a single point-like quantum dot. The energy in the  $(x, y)$ -plane at  $d = 15$  l.s. is shown [(a), the inset shows an enlargement of the central region]. In (b) the plane spanned by the  $z$ -direction and the  $[110]$ -direction is shown. The blue and red points mark the minimum and maximum of the elastic energy, respectively. The position of the point-like inclusion is indicated by white/black boxes (a) and a triangle (b).

our calculation the lattice constant  $a_{GaAs}$  of the parent material is chosen. The values of the strain energy decay logarithmically in the  $z$ -direction, a quantitative image as a density plot is therefore only meaningful for a small range of values of the spacer thickness (Fig. 4.10 (a)). Rather, for each plane the maximal and the minimal values are marked as points (Fig. 4.8, (e–h)). So the propagation of the strain field can be explored in detail.

For the GaAs material system the value of the angle under which the energy minimum propagates is  $\theta_{\min} = 25^\circ$ , as already shown in Sec. 4.2.1. The repulsive potential, corresponding to compressive strain and positive values of the elastic energy can be found under an angle of  $\theta_{\max} = 60^\circ$  (Fig. 4.9 (b)).

The situation of several inclusions with overlapping strain fields is shown in Fig. 4.10. As input sample structure an array of point-like inclusions, i.e. quantum dots, is taken, all of them with unique distance of 25 l.s. Although the minima are propagating similar to that of one single inclusion (Fig. 4.9, (b)), up to  $d = 20$  l.s. the attractive potential is located directly above the points of the input array (Fig. 4.10 (c), red curve). This gives rise to the assumption that correlated growth in this regions is favorable. In the region of  $d > 20$  and  $d < 30$  l.s. the attractive potential clearly is exactly in the gap *between* the ‘islands’ (Fig. 4.10 (c), blue curve). The occurrence of anticorrelated growth could be expected. From Fig. 4.10 one can visualize the angle under which anticorrelated growth is likely to occur, namely  $\theta_{\min} = 45^\circ$ .

Simple geometrical considerations would predict the occurrence of anticorrelated growth at a buffer layer thickness of

$$d_{anti} = b/(\sqrt{2} \tan \alpha), \quad (4.2)$$

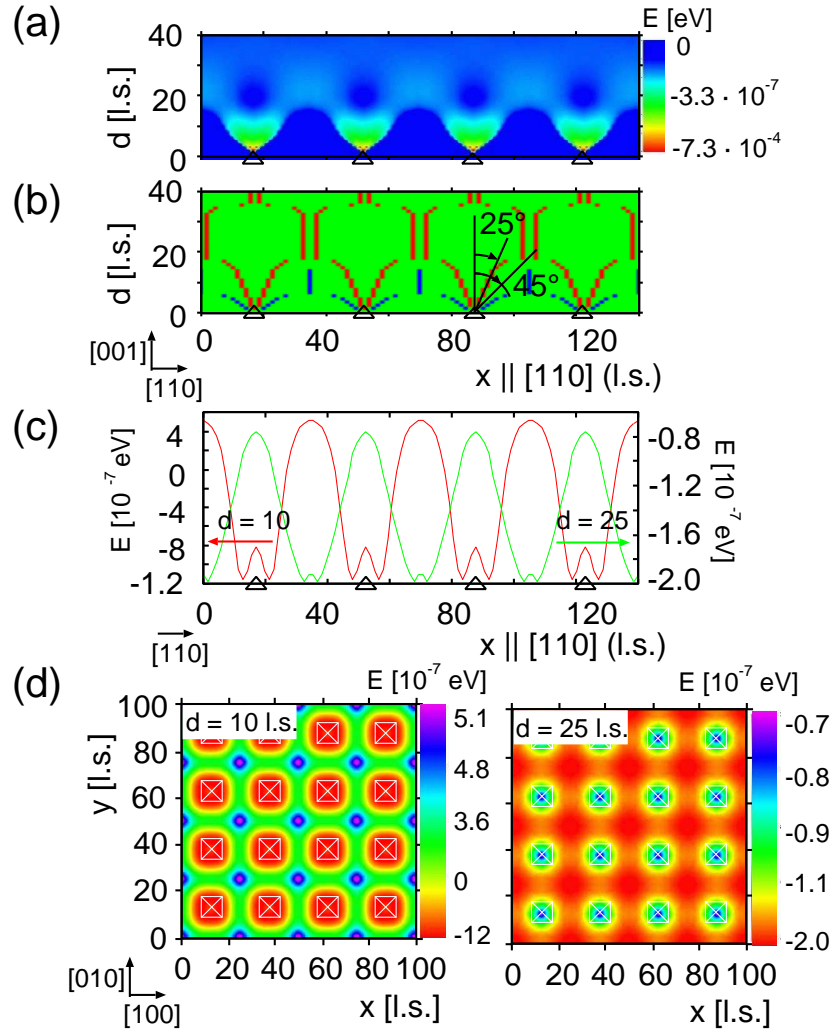


**Figure 4.10:** Elastic energy of a periodic array of point-like quantum dots. Sample size is  $100 \times 100$  l.s., distance of the inclusions is 25 l.s. The density plots (a, b) are cuts through the  $z$ -direction along [110]-direction. (a) density plot of the strain energy, (b) red and blue dots mark the minimum and maximum of the elastic energy respectively (c) strain energy at  $d = 10$  and  $d = 25$  l.s (d) strain energy in the  $(x, y)$ -plane at  $d = 10$  and  $d = 25$  l.s. Black triangles (a–c) and white squares (d) mark the positions of the point-like quantum dots.

with lateral island-island distances  $b = 25$  and  $\alpha = 25^\circ$  the result is  $d_{anti} \approx 38$ . This value for  $d$  conflicts with the calculations shown in Fig. 4.10. Instead of a potential leading to anticorrelation for this particular buffer layer thickness, again the attractive regions are located directly above the buried structures.

The propagation direction of the extrema is only for small values of  $d$  still the same as for single inclusion (Fig. 4.10 (c)). As soon as the strain fields overlap and interact,

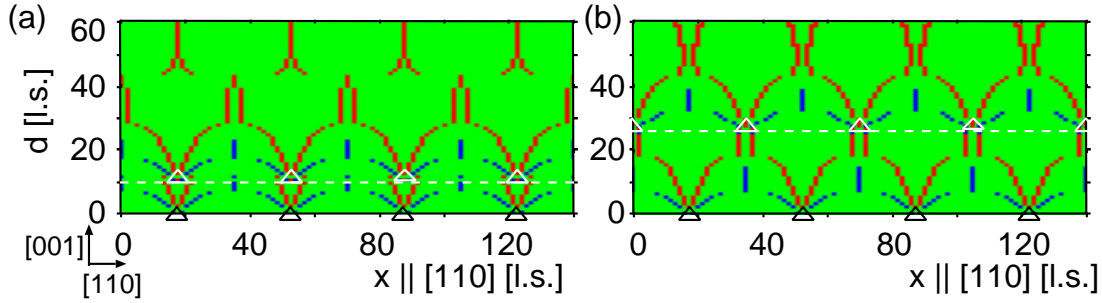


**Figure 4.11:** Elastic energy of an array of point-like quantum dots. Additionally to the periodic array at  $d = 0$  (Fig. 4.10) another one at (a)  $d = 10$  [(b):  $d = 25$ ] being vertical correlated (anticorrelated) is introduced. Sample size is  $100 \times 100$  l.s., distance of the inclusions is 25 l.s. All density plots are cuts through the z-direction along  $[110]$ -direction. The red and blue points mark the minimum and maximum of the elastic energy respectively. The positions of the point-like inclusions are marked by black and white triangles and the dashed white line indicates the location of the plane where the second array is inserted.

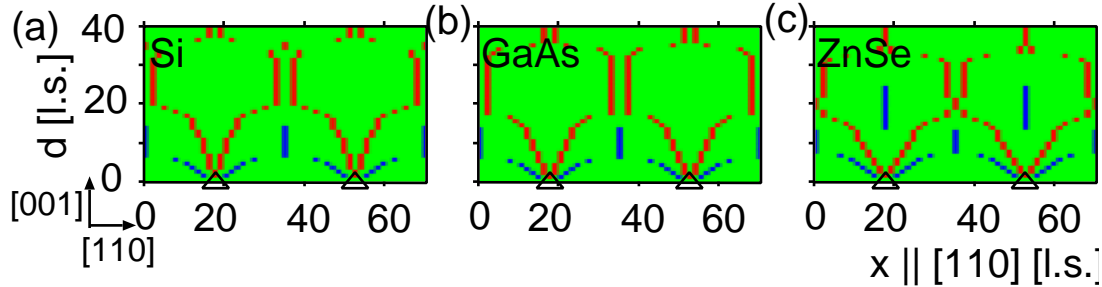


**Figure 4.12:** Same as Fig. 4.10 (b), but for (a) Si, (b) GaAs, and (c) ZnSe as parent material. Red and blue dots mark the minimum and maximum of the elastic energy respectively. The positions of the point-like quantum dots are indicated by triangles.

the behavior changes. The interaction can be seen for spacer layer thicknesses  $d$  larger than one half of the lateral island-island distance.

This interaction, however, seems only to play a role if the dots are in the same plane. In Fig. 4.11 additionally to the array at the bottom another one was introduced in the buffer layer. First, an array which is vertically correlated to the initial array, all point-like inclusions in the two arrays are placed directly above another (Fig. 4.11 (a)). And second, an array where the inclusions are between the ones of the underlying sample structure (Fig. 4.11 (b)). For both cases the vertical positions for the additional layers were chosen such that the arrays are placed at values for  $d$  where (anti) correlated positioning is likely to occur, namely  $d = 10$  for the correlated array and  $d = 25$  l.s. for the anticorrelated one (see Fig. 4.10). Above the additionally inserted arrays the propagation of the strain field in Fig. 4.11 (a) and (b) does not change significantly, but

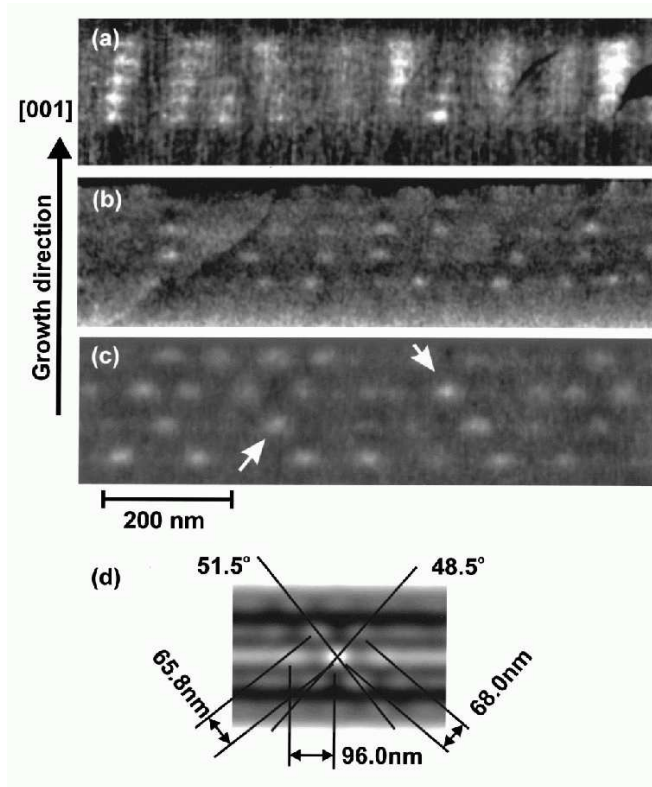


**Figure 4.13:** Cross-sectional atomic force microscopy images of the  $\text{In}_{0.5}\text{Ga}_{0.5}\text{As}$  QDs for a spacer layer thickness of (a) 75 ML, (b) 112 ML, and (c)  $150^+$  ML are shown. The autocorrelation of the image shown in (c) is given in (d). The gray scale is 5 Å. [Wan04]

rather seems to replicate the behavior of only one layer of inclusions (Fig. 4.10 (b)). Since the field resulting from the first layer is orders of magnitude smaller than the field arising from the other one it has almost no impact on the overall behavior (cf. Fig. 4.10 (a)).

The discussion above shows, how elastic interactions of an array of inclusions in a GaAs matrix might cause a modified correlation-anticorrelation transition. This is of great relevance since experiments indeed show that anticorrelated islands in the GaAs material system preferred to grow with a reclining angle of  $\theta_{\min} = 50^\circ$  (Fig. 4.13, 4.14; [Wan04]). This result almost agrees with our findings. The remaining discrepancy might come from the fact that not only the strain field is responsible for the stacking of the QDs. This might be caused also by interactions due to modulations in chemical composition and/or be due to morphological reasons in the spacer layer.

In the discussion so far in this section only GaAs was considered as parent material. As previously seen in Sec. 4.2.1 the directional properties of the strain field are strongly material dependent. Therefore with the use of the already described setup the resulting propagation of the strain field is shown in Fig. 4.12 exemplarily for Si, GaAs and ZnSe. It turns out, that also an increase of the angle  $\theta_{\min}$  with increasing anisotropy ratio, which was seen for single point defects in Sec. 4.2.1 too, can be observed. From Fig. 4.12 an angle of  $\alpha = 43^\circ, 45^\circ, 47^\circ$  can be obtained for Si, GaAs and ZnSe respectively.

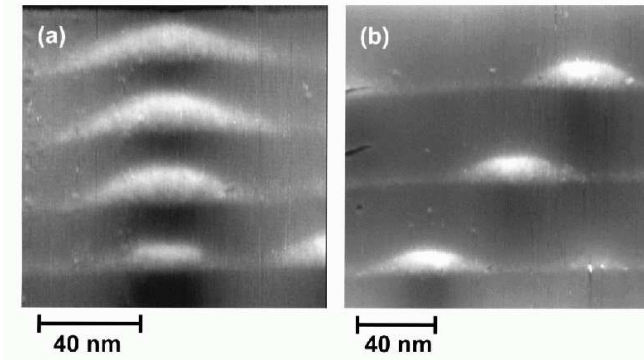


**Figure 4.14:** Cross-sectional scanning tunneling microscopy images of  $\text{In}_{0.5}\text{Ga}_{0.5}\text{As}$  QDs. (a) A column of correlated QDs in the 75 ML region and (b) an array of anticorrelated QDs in the 150 ML region. The gray scale is 5 Å. [Wan04]

#### 4.2.4 Periodic arrays of islands

Instead of point defects, the elastic energy of arrays of islands with different shapes is studied here. This can help to distinguish effects resulting only from the overlap of strain fields in arrays of inclusions and effects which are induced by the introduction of a volume.

To allow a good comparison to experiment we have chosen values which correspond to [Wan04] but are scaled down to make the computation feasible. In particular in Fig. 4.15 we show the strain field of an array of  $4 \times 4$  platelets, pyramids and cuboids. The direct connection to [Wan04] can be drawn for the sample structure consisting of pyramids having a height of 5 l.s. and a base of  $20 \times 20$  l.s. (Fig. 4.15, (b)). If we set one grid point of our calculation to one nanometer (1 l.s.  $\hat{=}$  1 nm), we obtain the setup of [Wan04] (Fig. 4.13, 4.14). The other sample structures are calculated to study the influence of the height to width ratio, even if their shape is very unlikely to occur in experiments.

First it is noteworthy that the previous calculated inclination angle  $\theta_{min}$  does not change. It coincides with the values obtained for arrays of point-like inclusions.

A striking new feature appearing here for the first time (Fig. 4.15, (a–e)) is that the minimum of the elastic energy is directly located above the buried structures and *remains at the correlated position* for a large range of spacer layer thicknesses  $d$ . In the previous section (Fig. 4.10) this behavior never was observed. Instead already for low values of  $d$  two separating minima appeared above the buried inclusion. Due to the volume effect of the minima being and staying above an island, the transition from the correlated to the anticorrelated regime starts at larger values for  $d$  and happens much faster compared to the point-like islands.

The samples of cubic shape (Fig. 4.15, (a, c–e)) show in small region of  $d$  properties of single point defects. At their edges minima and maxima appear, similar to that of Fig. 4.9, before minimum above the center of each inclusion builds up. In the central region these point-features do not show up, only at the edges due to symmetry reasons (i.e. the absence of neighboring atoms) this features are to be seen. Sample structures with smoother edges, such as pyramids (Fig. 4.15 (b)), also do not exhibit this behavior.

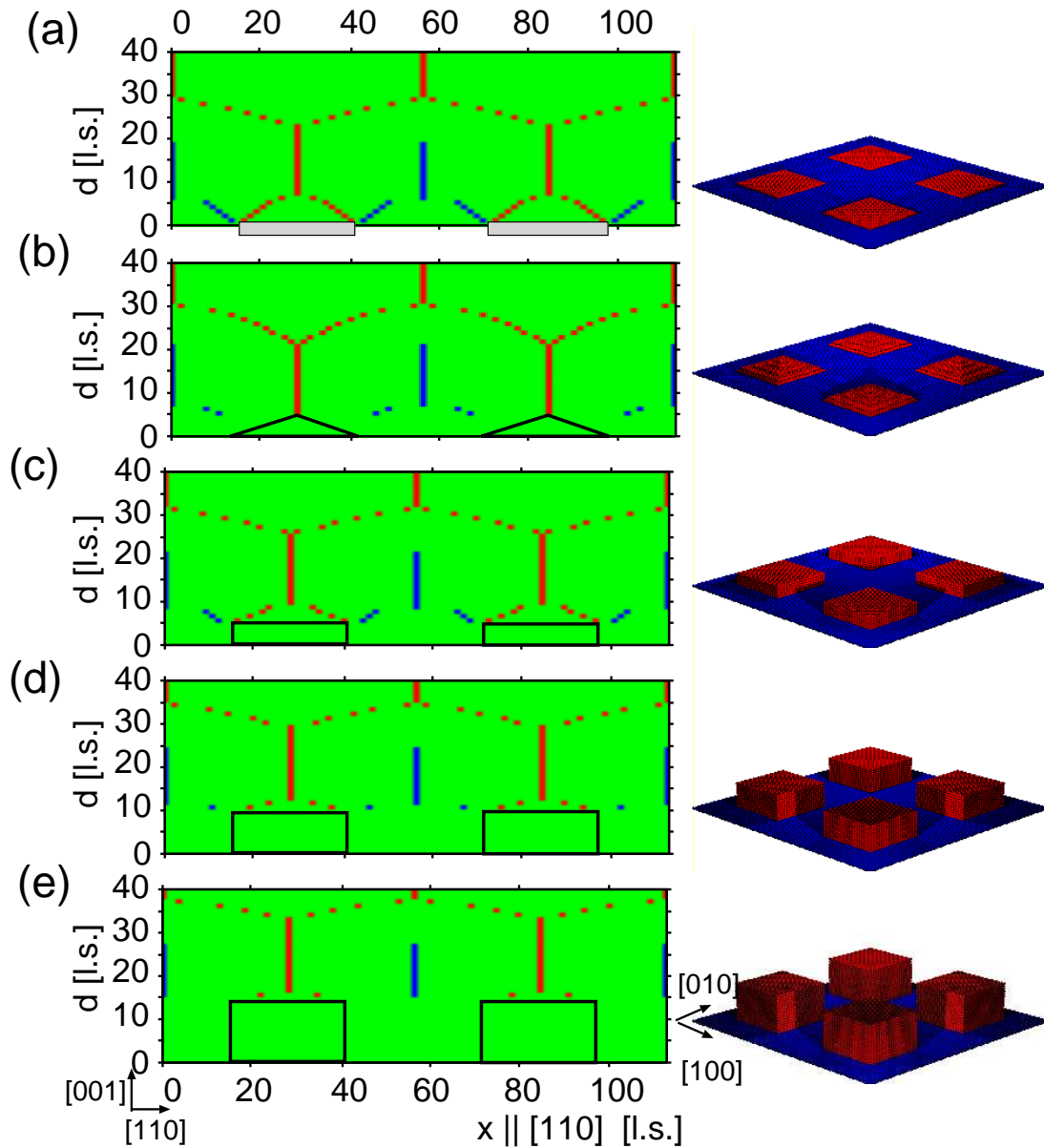


**Figure 4.15:** Elastic energy of an array of quantum dots of various shapes, which are (a) platelets with a height of 1 l.s. (b) pyramids with a height of 5 l.s. (c–e) cuboids with a height of 5, 10, 15 l.s. respectively. The lateral island distances are 40 l.s. each having a base length of  $20 \times 20$  l.s., Left: the plane spanned by the  $z$ -direction and the  $[110]$ -direction is shown. Red and blue dots mark the minimum and maximum of the elastic energy respectively. The positions and shapes of the quantum dots are indicated by black boxes or triangles. In the right panel the shape of the quantum dots is shown. Sample size is  $80 \times 80$  l.s.

The strain field of all sample structures shows, regardless of their width to height ratio, a central minimum with a vertical length of about 16 l.s. The vertical length of the transition region from the correlated to the anticorrelated positions of the minima, also seems to be influenced only by the width and the lateral distance of the inclusions, having always a value of about 5 l.s.

## 4.2.5 Stripe shaped array of islands

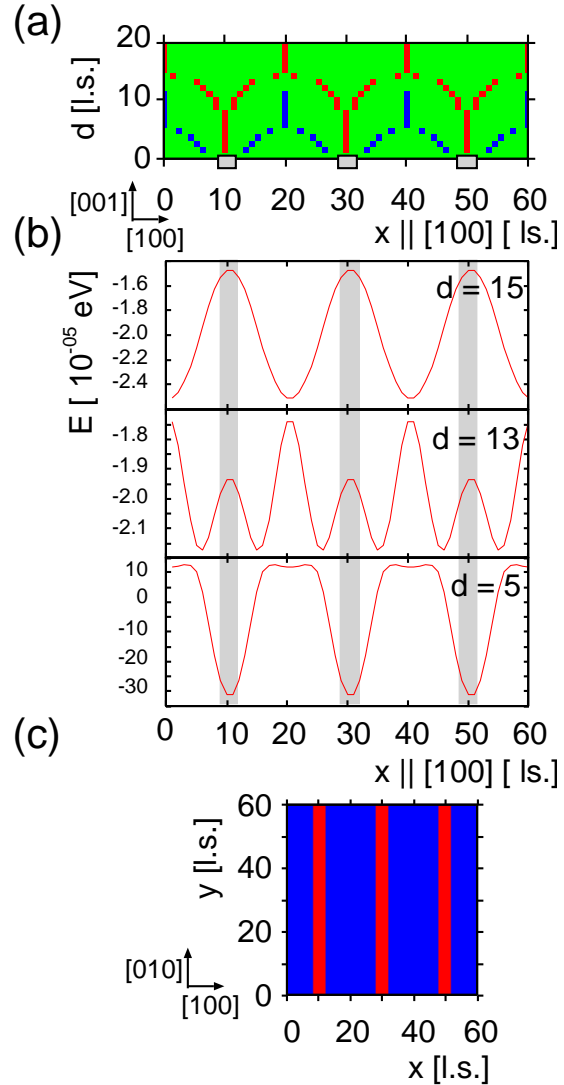
In the previous sections many properties of the strain field were investigated. Various shapes of inclusions were examined, and the case of regular periodic arrays of inclusions was discussed. One of the things which has not so far been discussed is the case of elongated structures, such as stripe-shaped islands. It should be noted that this investigation already was done in a broader perspective, Shchukin *et al.* studied such structures in an analytic approach [Shc98b], which was the starting point for the development of our model for the strain field (Ch. 3). The reason for presenting this point here is not only for completeness, but to present to the reader a comparative illustration.

In Fig. 4.16 the resulting strain field is shown. As input sample islands of a width of 4 l.s. and a distance between the islands of  $D = 20$  l.s. are taken. These values are chosen to be comparable to the values used by Shchukin *et al.* In [Shc98b] the properties depending on the island distance  $D$  are studied, the island width is varied from  $0.2D$  over  $0.35D$  to  $0.5D$  such as the spacer layer thickness. We set  $D = 20$  l.s. and get values of 4, 7 and 10 l.s. for  $0.2D$ ,  $0.35D$  and  $0.5D$  respectively. In our model periodic boundary conditions are used, so the islands have an infinite elongation in the one lateral dimension ([100]-direction) and are repeated infinitely often in the other one ([010]-direction).

Schematically the propagation of the strain field is shown in a density plot, as explained in detail in the previous section (cf. Fig. 4.8). In contrast to the results shown there, here a cut through [100]-plane is shown. Again it is clearly to be seen where vertically correlated growth is likely to occur, namely up to a spacer layer thickness of  $d < 10$  l.s. Starting from this point the minima above one island splits into two minima which are moving to the ‘anticorrelated position’ between two islands. The transition is shown in detail in Fig. 4.16 (b). It shows excellent qualitative agreement to the figure of Shchukin *et al.* (Fig. 4.18, [Shc98b]). The point where the transition occurs is, however, different. The deviation can be resolved by inspecting the type of material. While in [Shc98b] CdSe/ZnSe islands are studied in a parent material having elastic constants of  $c_{11} = 0.850 \cdot 10^{12}$  erg cm<sup>-3</sup>,  $c_{12} = 0.502 \cdot 10^{12}$  erg cm<sup>-3</sup>, and  $c_{44} = 0.407 \cdot 10^{12}$  erg cm<sup>-3</sup>, with an anisotropy ratio of  $A = 2.34$  in Fig. 4.16 the parent material is GaAs with  $A = 1.83$ . Therefore the vertical propagation of the minima of the elastic energy differs—the angle  $\theta_{min}$  is larger in [Shc98b] and the transition occurs at lower spacer layer thicknesses.

As shown in Sec. 4.2.3 with increasing anisotropy ratio  $A$  the inclination angle  $\theta_{min}$  increases too. In Fig. 4.17 a comparison between Si, GaAs, and ZnSe (with  $A = 1.56$ , 1.83, and 2.74) is shown. The transition point decreases with increasing  $A$ , and the

**Figure 4.16:** Elastic energy of stripe shaped islands. Material parameters correspond to GaAs. The width of the islands is 4 l.s. and their distance 20 l.s. The plane spanned by the  $z$ -direction and the  $[100]$ -plane is shown and only the extrema are marked (a). Blue and red corresponds to maxima and minima of the elastic energy respectively. (b) shows the elastic energy for certain values of  $d$ . The position of the islands is indicated by grey boxes below (a) and grey regions (b). A top view onto the sample structure is shown in (c).



transition takes place between 13 – 15 l.s., 8 – 15 l.s., and 5 – 12 l.s. for Si, GaAs, and ZnSe respectively. The region where the transition takes place is enlarged with higher values of  $A$  while the length of the central minimum above the islands decreases. For the material system examined in [Shc98b], which is inbetween GaAs and ZnSe with respect to the elastic properties, one can see a transition between  $0.35D$  and  $0.5D$  (Fig. 4.18, in our model:  $0.35D = 7$  l.s.,  $0.5D = 10$  l.s.). Our computations are in agreement with these values.

### 4.3 Summary

In the previous sections properties of the anisotropic three-dimensional strain field, calculated in the framework of elasticity theory, were presented. It was shown that the

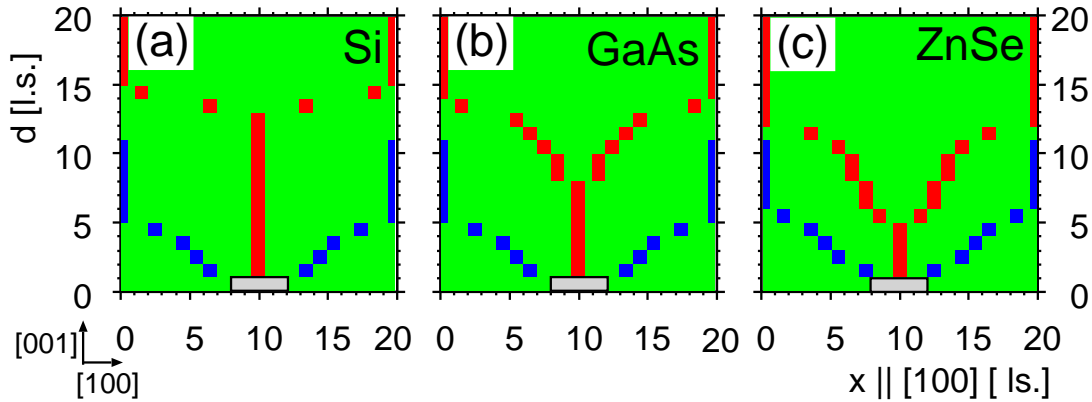


**Figure 4.17:** Elastic energy of stripe shaped islands for different parent materials. Material parameters correspond to Si, GaAs, and ZnSe in (a), (b), and (c) respectively. The width of the islands is 4 l.s. and their distance 20 l.s. The plane spanned by the  $z$ -direction and the  $[100]$ -plane is shown as an enlargement (cmp. Fig. 4.16). Blue (red) corresponds to maxima (minima) of the elastic energy. The position of the islands is indicated by grey boxes.

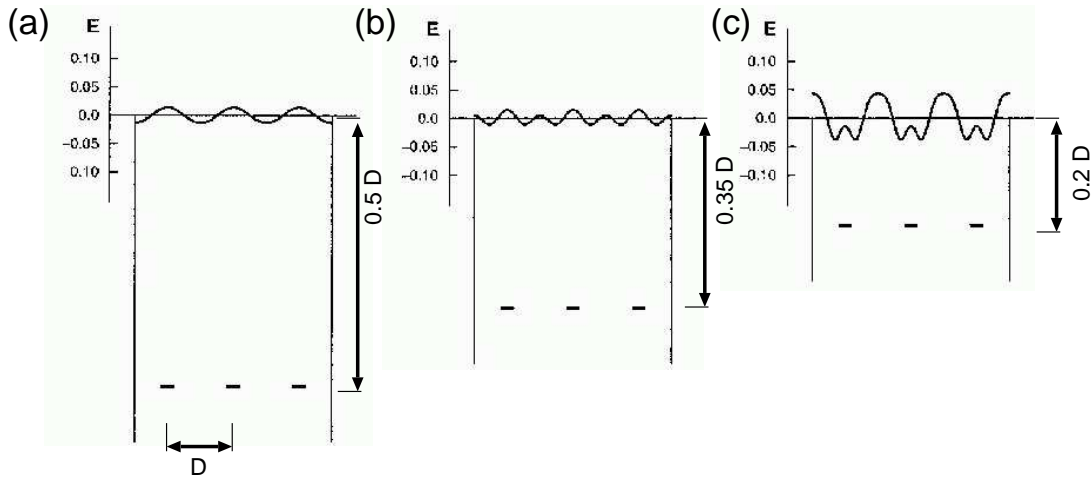


**Figure 4.18:** The interaction energy of a sheet of surface islands and a sheet of buried islands. Both sheets consist of identical one-dimensional arrays of infinitely elongated stripes. The energy is defined per unit surface area and is given in  $\text{meV } \text{\AA}^{-2}$ . The island distance is set to  $D$  and the width of the islands equals  $0.2D$ . Material: CdSe/ZnSe, [Shc98b]

computational efficient method developed in Chapter 3 offers the possibility to study arbitrarily shaped islands placed at any positions on the surface. In contrast to the strain field models previously studied in our group [Sch98b; Mei01c; Mei01a; Mei01b; Mei03a], not only compressive but also tensile strained regions can be considered.

While the first is acting as a repulsive potential for approaching adatoms, the latter gives rise to attractive regions which might serve as nucleation sites.

The foregoing investigations could already give some insights into various aspects of the self-organized growth of semiconducting materials—in particular the vertical placement of islands.

The results of the previous section can be condensed to the following points:

The elastic strain field is almost insensitive to the shape of islands. As long as no sharp edges or other highly non-symmetric shapes are considered.

The features of the strain field of one single inclusions are governed mainly by its volume and center of mass, and the elastic properties of the parent material.

If several inclusions are arranged periodically such that the strain fields coming from each island overlap and interact, the inclination angle of the strain field minima and maxima, which are in agreement with experimental findings, significantly differ from that of one single inclusion.

Taking into account the volume of islands and studying periodic arrays of arbitrarily shaped three-dimensional quantum dots, does not change the propagation of the strain field minima and maxima, but rather yields a large region where the strain field minima are located above the buried structures.

With increasing anisotropy ratio  $A$  the inclination angle of strain field minima  $\theta_{\min}$  increases, the transition point from correlated to anticorrelated positions of the strain field minima decreases while the region of transition is enlarged and the length of the central minimum above each island shrinks.

# Chapter 5

## Growth kinetics of quantum dot arrays

There are several requirements for the self-organized growth of ‘ideal’ quantum dots. Since there should exist at least one energy level the diameter of the QDs should not be smaller than a certain size. On the other hand an upper boundary is given by the fact that the temperature stability of QD based devices, such as QD lasers, becomes smaller if the spacing between the energy levels becomes too small. Therefore the QD size for the InAs/GaAs material system should lie in the interval of 4 – 20 nm. To ensure high efficiency of QD applications (e.g. QD lasers) a high density is required without losing high uniformity in size and shape of the QD structure.

In this chapter the way from the plain substrate towards epitaxial growth of one layer of ideal QDs is described. To cover the whole range of effects, their interplay and contribution to the process, various growth simulations and their dependence upon growth parameters will be shown.

Here we describe the self-organized growth of InAs QDs in a GaAs matrix.

### 5.1 Early stages of growth

Even the very first step, the deposition of material onto the surface is anything but easy to understand. Among various techniques of thin-film deposition, molecular beam epitaxy (MBE) probably is the simplest to understand, since it does not rely on difficult chemical reactions in some vapor or liquid phase, which are known to occur in, e.g., metalorganic chemical vapor deposition (MOCVD), vapor phase epitaxy (VPE), or liquid phase epitaxy (LPE) [Mad83; Her04]. Among other advantages, e.g., the capability of controlling the composition profile of alloys at the monolayer level, and easy implementation of in-situ measurements, of the MBE interactions of different atoms and molecules in the beam can be suppressed.

The question is, how can the growth process be described, starting from the source material which is evaporated in the so-called crucibles? The starting point is the de-

position of material, e.g., GaAs. Generally one can state that, when impinging onto the surface materials of the group III at relatively low temperatures have a sticking coefficient of unity [Chi90; Hey02]. In contrast, elements of group V need to ‘find’ group III elements at the surface, otherwise they cannot attach to them. The difference in these two cases is the fact that group III elements impinging as atoms and group V elements as molecules at the surface. In the latter case with respect to arsenic this could be  $\text{As}_4$  or  $\text{As}_2$  depending on the source material. Once the impinged adatoms stick on the surface they can move in the potential energy landscape associated with the underlying material and its reconstruction. Under most normal conditions, depending on temperature and the Ga:As flux ratio, on the GaAs(001) surface the  $(2 \times 4)$  and the  $c(4 \times 4)$  reconstruction can be found.

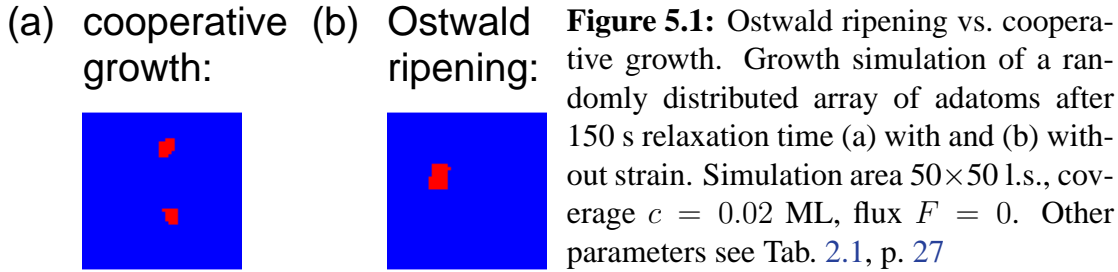
After the growth of the GaAs substrate InAs is deposited. First a wetting layer builds up by the most energetically favorable Stranski-Krastanov growth mode. This pseudomorphic layer grows lattice matched and is therefore uniformly strained. Moreover it was found out that its composition varies with the thickness and is not consisting of pure InAs, but rather of an  $\text{In}_x\text{Ga}_{1-x}\text{As}$  alloy with  $0.2 < x < 0.6$  [Joy99]. If the wetting layer thickness exceeds a critical coverage it will break up and islands start to form. The material for the islands is not only drawn from the new deposited adatoms but also is coming partly from the wetting layer of the surrounding islands. [Mül96b; Hei97b; Cul02; Pat03]

It still seems to be reasonable to assume, however, that the material, being heated in the evaporation cells, impinges onto the substrate with a certain flux rate  $F$ , which can be controlled and measured with high accuracy. This means that only one experimentally easily accessible variable comes into play. Other more complicated cases of course do exist but will not be covered here.

After the adatom has arrived at the surface it can move stochastically or it may evaporate again. The latter process is very unlikely to happen and therefore is not taken into account in the growth simulations presented later. Not only are the adatoms themselves treated here as effective atoms, but also the adatom motion is assumed to be a nearest neighbor hopping process under the influence of effective energy barriers (cf. Sec. 2.4, p. 21). The existence of a perfect defect-free wetting layer is implicitly presumed. From the microscopic point of view the story is of course much more complicated [Fra03] and there are only very few attempts to model all atomic processes in detail within a kinetic Monte Carlo approach [Kra02b].

## 5.2 Strain effects

As already mentioned before, the lattice mismatch of the material system used in heteroepitaxial growth gives rise to a strain field, which plays a crucial role in self-organized nanostructure formation. First of all, it ‘activates’ the Stranski-Krastanov growth mode, if the mismatch exceeds a certain value. This is true for InAs/GaAs, but in material systems with lower mismatch island growth often occurs due to the Asaro-



Tiller-Grinfeld instability, or to state it in other words, in low strain materials strain relaxation leads to the formation of islands, mounds and cusps [Jes93].

At later stages of growth due to the strain field, Ostwald ripening, which in the limit case would lead to *one* large island, is suppressed. Instead, the islands grow cooperatively. This point has already been shown earlier with the use of a phenomenological strain field [Sch98b]. As a quick test that this is also valid for the model of this work, in Fig. 5.1 a specific setup of a growth simulation is shown. Starting with a randomly distributed array of adatoms on the surface, the sample relaxed for 150 s in absence of strain (Fig. 5.1 (a)), and in the presence of the strain field (Fig. 5.1 (b)), respectively, both without additional deposition. Indeed it can be seen that with strain two islands of nearly the same size have formed while without strain only one large island survives.

The above was a discussion on the mesoscopic effects. The effects on the atomic scale shall now be discussed. While it is known and commonly accepted that strain has an impact on the binding energies and diffusion barriers (of adatoms), the question how both physical quantities are connected to each other is still debated. Thus, for example contradictory findings were reported for the Ag/Ag(111) system. While [Bru95] reports a lowering of the diffusion barrier under the influence of tensile strain larger than 3.5%, in [Rat97] a linear increase was found instead<sup>1</sup>. In semiconductor materials it was found that tensile strain corresponds to a high diffusion barrier while compressive strain leads to low diffusion barrier and the connection between the strain and barrier is mostly reported to be linear. The principle influence can be easily understood in an intuitive picture considering the limit case of large strain. While under large compressive strain the substrate behaves like a continuous film on which adatoms can move easily, in the opposite case the substrate consists of isolated atoms, so for each movement the adatom has to break a bond and form a new one, such that the diffusion barrier is equal to the pair-bond energy. For InAs/GaAs not only a linear dependence was found [Sch97]. Based on first-principles calculations Penev *et. al.* reported a different behavior [Pen01]: For any tensile strain the binding energy is monotonically decreasing. At a compressive strain of 3% the energy reaches its maximum and a larger compressive strain yields a reduction of the energy again.

In our calculations the trace of the strain tensor enters linearly in the energy barriers (see, e.g., Eq. (3.25)). This *is* an assumption, of course, but seems to be reasonable

<sup>1</sup>Both articles treat the same material system but with different methods. In [Bru95] effective-medium theory was used and [Rat97] investigated the strain effects from first-principles.

since one can expand the energy in a power series of the strain. The linear term is non-zero, so it makes sense to stop there [Shc03]. Moreover, the results of the simulations presented in this and the next chapter justify this treatment. The elastic energy  $E_{str}$  derived in Ch. 3 enters in the Arrhenius term as additional constant (cf. Sec. 2.4 and in particular Eq. (2.20) on p. 21).

To re-iterate an important point, commonly it is accepted that regions with tensile strain favor the nucleation of islands, while in the opposite case, in regions with compressive strain, the nucleation is hindered [see e.g. Liu99; Ter96]. The latter case plays an important role during the two-dimensional growth, discussed in this chapter, and the first case is responsible for the vertically aligned growth in stacked QD structures (see Ch. 6).

## 5.3 Variation of growth parameters

In the following the influence of experimentally easily accessible growth parameters is discussed and investigated using the previously described kinetic Monte Carlo routine (Sec. 2.4).

A special focus is set to the influence of the self-consistently calculated strain field. It should be mentioned that, however, the main interest of this work is *not* presenting an optimized set of parameters. This was already done in our group [Mei03a], (Fig. 5.3). Instead, the simulation routine was developed further and optimized for numerical efficiency, since the computation of quantum dot stack growth, being discussed in the next chapter, requires lots of (CPU-) resources.

The major differences to the model used previously [Mei03b] is the model of the strain field developed here fully incorporates the elastic anisotropy of the semiconductor material character and does not use a fit parameter to adjust the strength of the elastic energy contribution in the Arrhenius factor.

The main focus is set on vertical correlation and anticorrelation properties of QD stacks, being treated in the next chapter.

### 5.3.1 Temperature and flux

The influence of the temperature  $T$  on the growth process is easy to be seen in the Arrhenius term (Eq. (2.19), p. 21). An increase of this parameter increases the mean free path of a deposited adatom. The flux, or deposition rate  $F$  is a measure of how fast material is deposited on the surface. Both parameters, temperature and flux, are connected to each other such that a similar surface configuration can be found with parameters  $(T_1, F_1)$  and  $(T_2, F_2)$  where, e.g.,  $T_1 < T_2$  and  $F_1 > F_2$  (Fig. 5.2). This may be explained in the framework of rate equations.

The diffusion constant is given by [Bar95]

$$D(T) = D_0 \exp\left(-\frac{E}{k_B T}\right) \quad \text{with} \quad D_0 = \frac{1}{4} a_0^2 \nu_0 \quad (5.1)$$

with  $\nu_0$  the attempt frequency and the lattice constant  $a_0$ . With increasing temperature the mean free path of the adatom becomes larger and therefore also the probability for attachment onto existing islands instead of building up new islands. The characteristic distance  $l$  of nucleation centers can be described by [Bar95; Ven84; Sch95]

$$l \sim \left(\frac{D}{F}\right)^\gamma \quad (5.2)$$

with, e.g.,  $\gamma = 1/4$  being connected to the size of the largest mobile cluster. This length gives the radius of the area from which an existing island can draw adatoms, the so-called capture zone<sup>2</sup>.

In an intuitive picture this is plausible. On the one hand the higher the temperature the higher the mobility of adatoms and therefore the mean free path. The probability that two adatoms meet and nucleate is lower than the probability that the adatom reaches an existing island to attach on it. On the other hand, having many deposited single adatoms on the surface, due to a high flux rate, the movement of the adatoms is hindered and the mean free path lower. The nucleation probability for new islands becomes higher.

In Fig. 5.2 results of KMC simulations, surface images after a total growth time of 50 s and histograms of the island size distributions at flux end and after 50 s growth time, are shown. The histograms of Fig. 5.2 and the following show the square root of the number of island atoms, i.e., the mean diameter in atomic lattice units, as the island size. Here, and in the following chapters the anisotropic strain field of Ch. 3 was used (see also Sec. 3.4). The flux rate and temperature were varied, while the coverage was kept constant at 30%, meaning that the flux was set to zero after 0.3 (3, 30) s growth time in the samples with a flux rate of  $F = 1$  (0.1, 0.01) ML/s. Clearly the above explained behavior is to be seen, an increase of the temperature (or lowering the flux rate) leads to a decrease of the island size and an increase of the island-island distances.

The preferred alignment of islands in the [110]-direction may be caused by the strain field, which is in this direction smaller than in the [100]-direction (cf. Fig. 4.1 on p. 56). Therefore, adatoms arriving at islands are more likely to attach at these places. Moreover, if during the growth process two islands coalesce, this preferably happens at their diagonals. This behavior also was found in experiments for different materials, like SiGe on Si [Mei01b] but also in InAs on GaAs [Kra05].

However, it should be noted that not only the strain is (or could be) responsible for the anisotropy effects. In [Bel00] it was shown that for InAs ( $2 \times 4$ ) on GaAs(001)-( $2 \times 4$ ) “strain plays a negligible role in their [the islands] nucleation, and the [...] reconstruction dominates both island growth and island anisotropy.” So, at least for other reconstructions than the ( $2 \times 4$ ) this statement is not true, as our calculations indicate.

<sup>2</sup>Please note, Eq. (5.2) is only valid for simple models: irreversible layer-by-layer growth in the submonolayer regime without strain effects. For more advanced descriptions see [Ama02, and cites therein] and [Mul96a; Eva01; Eva02; Shi05a]

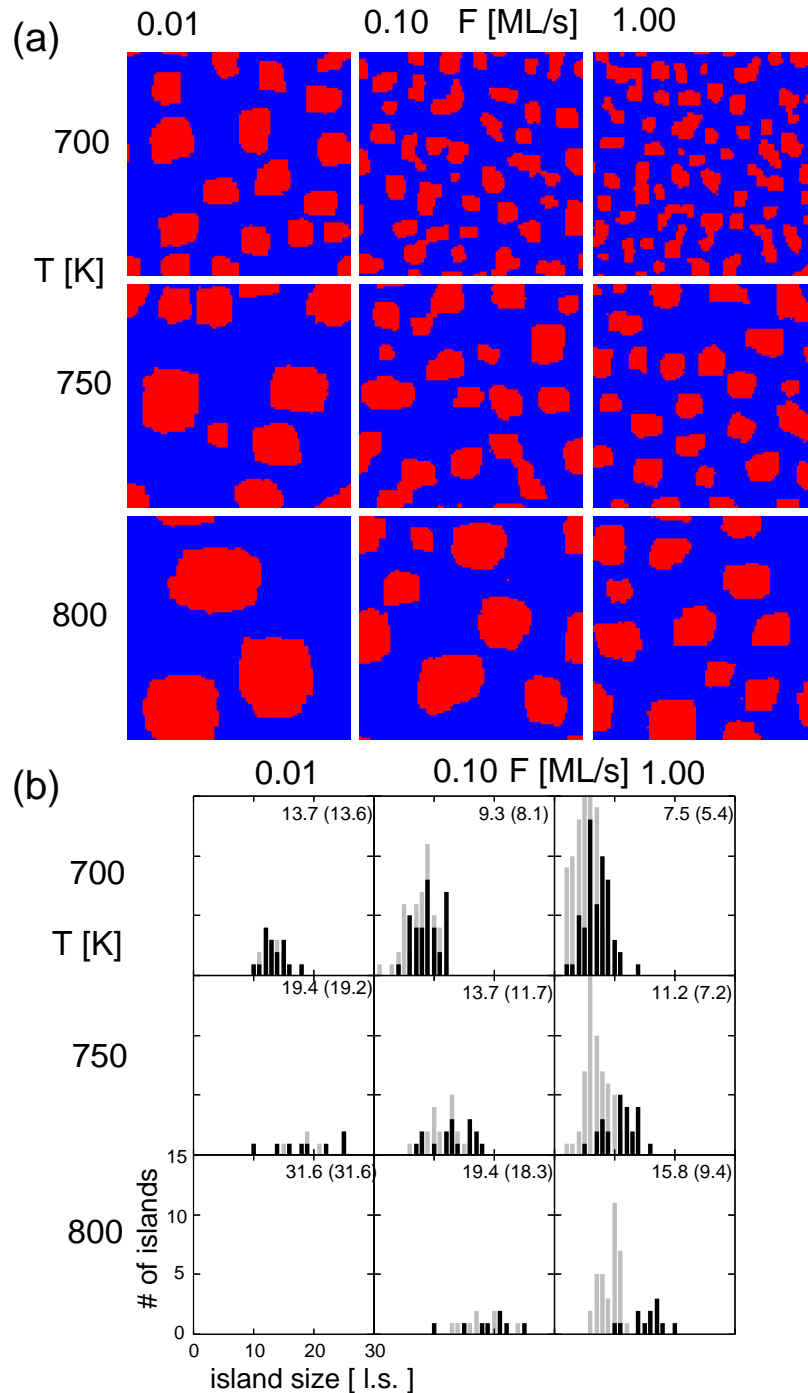


**Figure 5.2:** Results of the KMC simulation of quantum dot arrays. (a) surface images after 50 s growth time. (b) the histograms show the island sizes at the end of deposition (gray) and after 50 s (black, corresponding to the surface configurations shown in the upper panel). The numbers in the histograms indicate the mean island size of the sample (in brackets: mean island size after end of deposition). The axes are kept fixed, such that larger islands might not be shown. Simulation area  $100 \times 100$  l.s., coverage 30%. Anisotropic strain field.

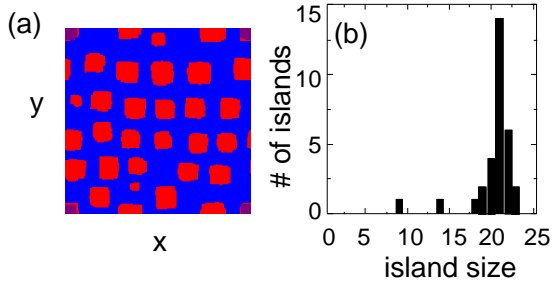


**Figure 5.3:** Optimized spatial ordering. (a) Spatial arrangement of islands. (b) Corresponding island size distribution. Parameters are: simulation area of  $200 \times 200$  l.s.,  $T = 700\text{K}$ ,  $F = 0.001\text{ML/s}$ ,  $c = 34\%$  and a growth interruption of  $t_{\text{ir}} = 500\text{s}$  after the end of deposition. Isotropic strain field was used. [Mei03a]

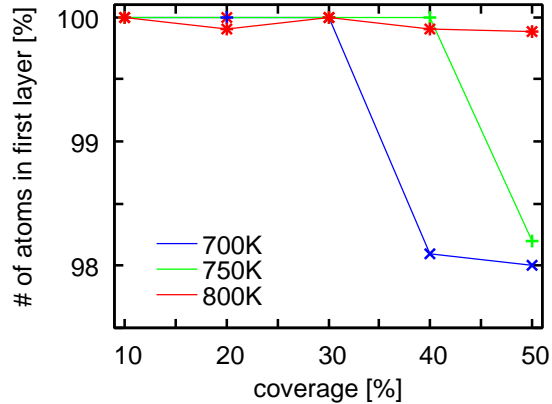
Previous investigations in our group [Mei03a] have shown the possibility to simulate QD arrays with a high degree of spatial ordering and a narrow island size distribution using an isotropic model for the strain field (Sec. 3.5) and additionally taking into account bonds to the next nearest neighbors (Fig. 5.3). Compared to that, the degree of spatial ordering in the simulations shown in Fig. 5.2 is lower, in general, and the arrays exhibit a broader island size distribution.

### 5.3.2 Coverage

The coverage  $c$  describes how much material is deposited on the surface above the wetting layer. It certainly has an effect on QD size distributions, since one cannot expect islands of equilibrium size if not enough material is deposited. On the other hand, if more material is dropped to the surface than necessary for optimal island sizes, small amounts may be compensated by a reduced distance of islands. At some point, however, islands will have to merge or make a transition from in-plane growth to three-dimensional growth. In the following, this point will be referred to as the critical coverage denoted as  $c_c$ .

In Fig. 5.4 the number of atoms in the first mono layer above the wetting layer are shown in dependence of the coverage. All other atoms are located in the monolayers above, in the growth regime examined here, in the second monolayer. It can be seen that the transition point  $c_c$  is different for different temperatures. For  $T = 700\text{K}$  the value of  $c_c$  lies between a coverage of 30–40% whereas for  $T = 750\text{K}$  this point shifts towards higher coverages. Since the mobility is increased with increasing temperature it is clear that the Schwöbel barrier is more easy to overcome. For higher temperatures adatoms on top of an island jump down and attach onto the island in the first layer. Further increasing of the coverage, however, leads to a higher probability that newly deposited adatoms already arrive on top of an existing island, and the more adatoms are located in the second layer the higher the probability that they attach to each other and build a stable nucleus in the second monolayer. For  $T = 800\text{K}$  the mobility in general is very high. Adatoms can, therefore, easily overcome both, the Schwöbel barrier and the pair bond energy. That is why the distribution of atoms in the different layers already at low coverage is random.

**Figure 5.4:** Number of atoms in the first monolayer vs. coverage. Simulation area  $100 \times 100$  l.s., flux rate  $F = 0.01$  ML/s, simulation time 50 s.



For several reasons we restrict ourself in this work mainly to the low-coverage, submonolayer regime: Firstly, it is known that (large) 2D islands remain at their places and act as island fundamentals for fully developed 3D islands [Pri95; Kun90]. Therefore, the positions of the QDs is already fixed by the submonolayer islands. Secondly in our mesoscopic KMC approach we are able to simulate large arrays of self-organized QDs retrieving time-resolved as the main quantities information about their size and their positions. Simulations and models concerning the detailed ‘real’ three-dimensional shape of QDs are done within microscopic approaches, which include the details of, e.g., the binding energies on an atomic level (cf. Sec. 2.1). These issues are not addressed here. Third, our intention is to combine KMC simulations with a realistic strain field. The influence of the strain field after the 2D-3D transition is known to be small [Krz02] and therefore not of interest to us. Finally, the model of the strain field is such that we are looking for a solution in a halfplane (cf. Ch. 3). This implies that we can calculate the 3D strain field of a given structure only for layers being *above*.

It should be noted that monolayer height islands are, however, of great relevance too, although most studies are concerned with extended three-dimensional islands [see e.g. Gon98; Tsa99; Kov02].

### 5.3.3 Growth interruption

In general a growth interruption has a smoothening effect on crystal surfaces [Kam96]. As an example how remarkably the properties of surfaces can change during equilibration following the end of deposition, in Fig. 5.5 the island size distributions and their temporal evolution is shown for two different flux rates with constant coverage  $c = 30\%$ . It should be noted that for a flux rate of  $F = 0.01$  (1.00) ML/s the flux is turned of after 30 (0.3) s, so the growth interruption time is different for the two samples shown.

For the sample grown with a flux rate of  $F = 0.01$  ML/s (Fig. 5.5 (a)) it can be seen, that at deposition end (30 s) the island size distribution is broad but as a trend a

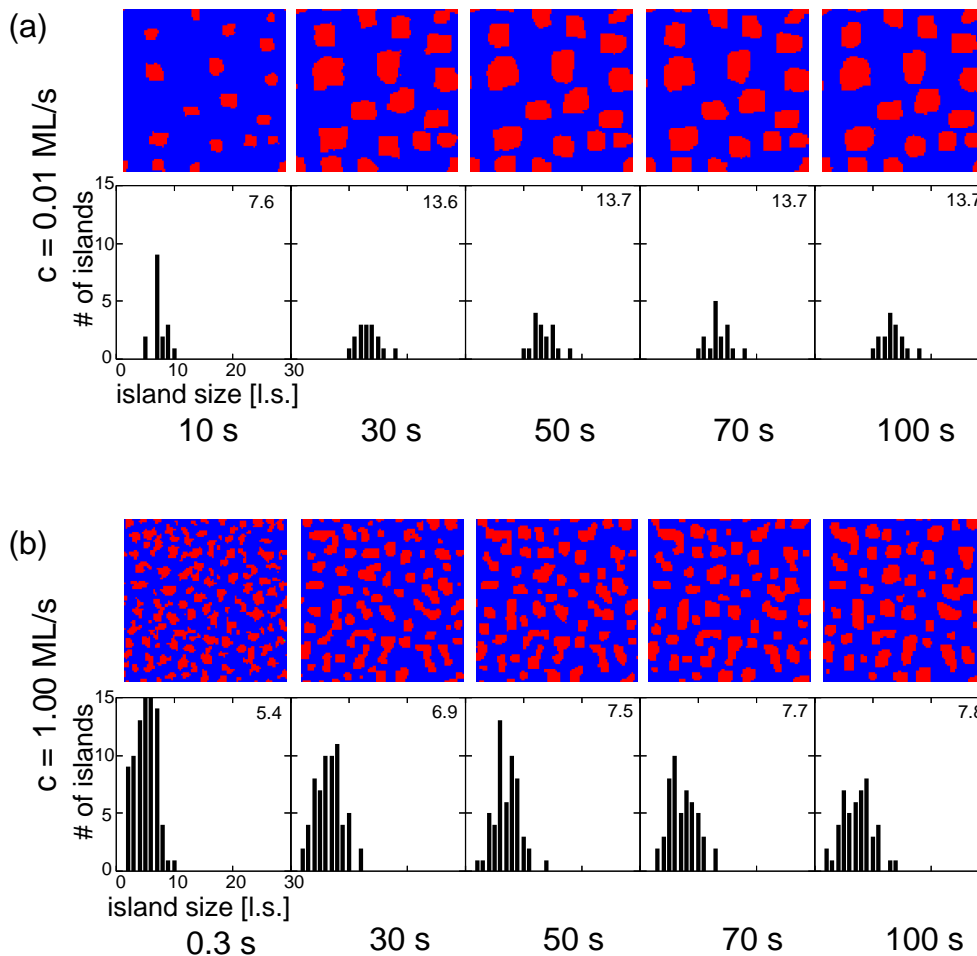


**Figure 5.5:** Temporal evolution of island size distributions. The numbers in the histograms indicate the mean island size of the sample. Simulation area  $100 \times 100$  l.s., coverage 30%, temperature 700 K.

preferred island size<sup>3</sup> of about 10 l.s. which during equilibration nearly stays constant can be evaluated. After the end of deposition the distribution becomes marginally sharper and the dominant island size gets more pronounced. In contrast, in the other sample (Fig. 5.5 (b)) with the higher flux rate much more islands of a small size are to be seen at the end of deposition (0.3 s). During the equilibration process the distribution shifts to larger islands but still small islands remain on the surface and the distribution is rather broad, even after 100 s.

As already explained in the previous sections, this is an effect of the low mean free path resulting from the large flux rate. The motion of adatoms is hindered by other adatoms and already existing islands and moreover, already in early stages of growth

<sup>3</sup>As the island size the square root of the number of island atoms, i.e., the mean diameter in atomic lattice units, is used.

many small islands, dimers and trimers, exists which in principle may dissolve again, but since the pair bond energy is relatively strong it is very unlikely to happen.

But of course also temperature has an influence on the equilibration process and the temporal evolution of the island sizes. In Fig. 5.2 the island size distributions at the end of deposition and at the end of growth are shown. Even if the surface configurations for some parameters (e.g. 700 K, 0.01 ML/s and 800 K, 1.00 ML/s) look similar it becomes obvious that, since with higher temperature the mean free path of adatoms is larger, the island sizes change much more with time at higher temperatures.

## 5.4 Summary

The simulation of one layer of quantum dot arrays using the anisotropic strain field model was discussed. By varying growth parameters like temperature, flux rate, and coverage, it was shown that our findings are in good agreement with experiments.

In some simulations island shapes aligned at the elastic hard ([110]) direction could be observed. This might be caused by the anisotropic strain field and is expected to be more pronounced in material systems with higher anisotropy ratio  $A$ , e.g. ZnSe, and to play a less important role in systems with low  $A$ , e.g. Si. Additional investigations to clarify the influence of the degree of anisotropy of the material system on the island shape and ordering could be of great value.

This chapter is intended to show not only growth properties of quantum dots simulated by kinetic Monte Carlo combined with strain field from elasticity theory. Rather it should be seen in a broader perspective, demonstrating the features which occur in *each layer* during the simulation of stacked quantum dot arrays. And, moreover, showing the properties of the simulation routine developed and optimized for this purpose.

# Chapter 6

## Growth of stacked structures

In the development of growth techniques of nanostructures, the step from the growth of one layer of quantum dots towards multilayer systems seems to be a natural and logical evolution. The necessity for growing one quantum dot layer above another came from the requirement of having as many dots per volume as possible to increase efficiency, e.g. laser intensity. Besides this, soon it was found out that this technique provides the chance to improve the regularity of size and spatial ordering [Sta04].

Probably the first experiment demonstrating vertically aligned growth of InAs/GaAs quantum dots was reported by Xie *et al.* [Xie95] (see Fig. 6.1). Also, the so-called pairing probability, a measure to quantify the quality of the vertical alignment, was used there for the first time (see Sec. B.2). As commonly accepted, the vertical stacking of islands is induced by the strain field resulting from the buried quantum dot (QD) layers, which also gives rise to a lowering of the critical thickness, i.e., the transition point from the two-dimensional (2D) layer growth to the three-dimensional (3D) island growth, in the Stranski-Krastanov growth mode of the second and following layers, meaning that the transition from the flat 2D to the 3D growth occurs at earlier stages [Dun01]. Another stacking mode for a material system close to that examined here, was found recently. Wang *et al.* [Wan04] showed not only the well known correlated growth, but also were able to prepare a sample of InGaAs/GaAs quantum dots grown in the *anticorrelated* stacking mode (Fig. 6.2).

Also the island shape may be influenced by the underlying strain field, such that in the first layers one certain shape is favored while in all preceding layers another shape of the islands is dominant. For example in the SiGe material system a transition from dome shaped islands in the first, to pyramidal islands in the second layer was

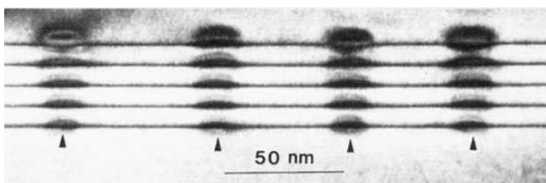
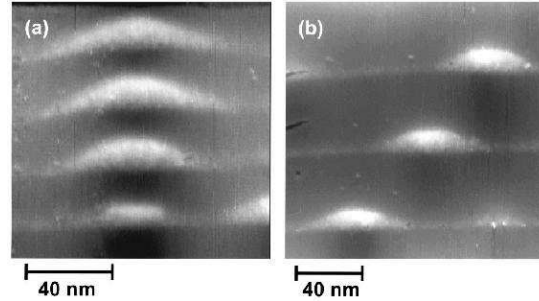


**Figure 6.1:** Transmission electron microscope (TEM) image of an InAs/GaAs quantum dot stack [Xie95].

**Figure 6.2:** Cross-sectional scanning tunneling microscopy (STM) images of the  $\text{In}_{0.5}\text{Ga}_{0.5}\text{As}$  QDs. (a) A column of correlated QDs and (b) an array of anticorrelated QDs [Wan04].



observed [Usa00].

The possibility to improve the ordering of nanostructures was reported in various articles and for various material systems. To give only a few examples: In [Tei96] it was shown that the regularity of SiGe/Ge multilayer improves. The PbSe/ $\text{Pb}_{1-x}\text{Eu}_x\text{Te}$  material system was investigated in [Raa03]. They observed for example, that an fcc-like stacking only occurs in certain temperature ranges and spacer layer thicknesses. The detailed tuning of properties by changing the spacer layer thickness was studied in [Spr00]. By changing this quantity it is possible to switch between three different stacking types. Also one can control the interdot spacing by changing only this single parameter. The above mentioned techniques are examples for using the strong elastic anisotropy of this particular material system to induce the desired degree and type of ordering.

Prepatterning methods are also very attractive for achieving a better control of island positioning. Before the structure may evolve self-organized the very first layer on which the further growth takes place is, mostly lithographically, manipulated. The subsequently grown layers on top of the prepatterned substrate evolve in the presence of a certain well defined surface curvature and/or surface stress. Lee *et al.* presented a surface strain engineering method applied to the  $\text{In}_x\text{Ga}_{1-x}\text{As}/\text{GaAs}$  system [Lee00; Lee01]. The patterning was done with optical holography on a photoresistive film. They showed that the unit cell dimensions, the orientation, and the number of quantum dots are tunable with the method introduced.

In [Kar04] a patterned structure was fabricated with electron-beam lithography and reactive ion etching on Si(001) substrates. After growing a Si spacer layer another Ge layer was overgrown. The Ge islands showed perfect vertical alignment.

All these effects are, however, *more or less* attributed to changes of the local strain field due to a buried layer of islands. But it should be underlined that the strain itself can *not* be the only driving force for all this. In [Pri01] it was shown that the minima of the surface strain induced by buried structures are too low to serve as nucleation sites. This fact and its impact on our results will be discussed further in the following investigations.

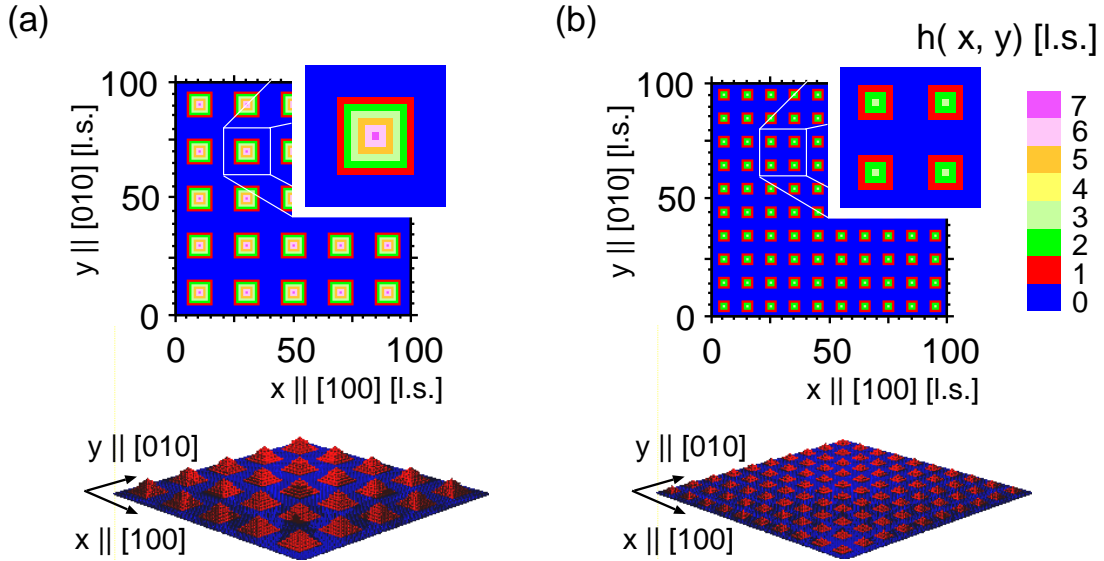


**Figure 6.3:** Sample structures used for the growth simulations of QD stacks on prepatterned substrate. The height profile  $h(x, y)$  (upper panel, the insets show an enlargement of the areas marked with white boxes) and a perspective view of the periodic arrays are shown (lower panel). The periodic arrays consist of  $5 \times 5/10 \times 10$  pyramids with baselengths of  $11/5$  l.s. and heights of  $7/3$  l.s. in (a)/(b), respectively.

## 6.1 Growth on prepatterned substrate

We start with growth simulations of stacked structures using a patterned substrate. As already mentioned, this technique also is commonly used in experiments [Kar04; Lee00]. The focus of our investigations is set on the widely used InAs/GaAs material system and all simulation parameters in Ch. 6) are chosen accordingly (cf. Tab. 2.1, p. 27).

For quantifying the spatial correlations of island positions in the subsequent grown structures, two measures are used in the following. Mostly the cross-correlation coefficient  $C(0)$  will be examined. The detailed derivation is shown in the appendix B.1 on pp. 109. It is derived from the height-height correlation function and directly connected to the rms-roughness. Moreover this measure is commonly used in the field of image recognition. The cross-correlation coefficient may have values  $C(0) \in [-1, 1]$  meaning

$$C(0) = \begin{cases} 1 & \text{correlation} \\ 0 & \text{random distribution} \\ -1 & \text{total anticorrelation} \end{cases} \quad (6.1)$$

The term ‘total anticorrelation’ differs from ‘anticorrelation’ used in the field of semiconductor QD growth and the reader should be warned not to mix them. In the first case one of the structures is the complete inverted image of the other, whereas in the

latter case islands on top are located in the space between the islands in the buried layer (Fig. B.1 in p. 111).

The second quantity is the pairing probability. For this also, a derivation can be found in the appendix B.2 on pp. 111. The advantage is that the full range from correlated over randomly distributed to anticorrelated growth is covered. On the other hand it is strongly sensitive to fluctuations in the island positions.

The very first test scenario, of course, should be a growth simulation where all possibly perturbing influences are switched off and only the influence of the strain field coming from the first layer(s), upon the growth of the next layers is studied. To achieve optimal lateral ordering a given periodic structure of islands is used as lowest layer. For a description of the simulation routine the reader is referred to Chapter 2 and in particular Sec. 2.4 on page 21.

In this section two samples are used as prepatterned surfaces. Each consists of a regular array of ( $5 \times 5/10 \times 10$ ) pyramids with a baselength of  $11/5$  l.s. and heights of  $7/3$  l.s (Fig. 6.3). This corresponds to a coverage in the first layer of about  $c = 30\%$ . The decision to choose pyramids and not other shapes, such as lenses or truncated pyramids, which are reported to occur in experiments [see e.g. Xu05] seems to be restrictive, but is more universal than one might expect at first glance. The resulting strain fields of such structures, provided that they have nearly the same volume, does not differ much, as was shown in Sec. 4.2.2.

### 6.1.1 Vertical correlated growth

The cross-correlation coefficient of simulated QD stacks averaged over five runs is shown in Fig. 6.4. Since it already could be expected that the incorporation of the strain field would not be sufficient to induce vertical ordering, the strength of the strain field was increased by a factor  $W$ , such that the total energy used in the Arrhenius term (Eq. (2.19), Eq. (2.20) on p. 22) becomes

$$E = E_s + E_b - W E_{str} \quad (6.2)$$

From experiments it is known that for small spacer layer thicknesses vertically correlated structures will be formed, and at some point a transition from correlated to anticorrelated growth is likely to occur. Our theory of the strain field gives the same predictions and moreover can support experimental findings on the detailed positions of quantum dots in the anticorrelated growth mode (Sec. 4.2.3). Obviously strain effects alone can not induce the vertical ordering in our model; not even for small spacers does vertical correlated growth occur (Fig. 6.4). But it is known that not only energetic strain effects are responsible for correlated growth. Therefore it is natural to introduce an additional factor that is attributed to effects which are not modeled within this work, such as surface reconstructions, morphological aspects in the spacer layer and/or the chemical composition, or kinetic effects during growth. From Fig. 6.4 one can see that a factor, which we will call strain weight, of  $W = 250$  is sufficient, since a vertical

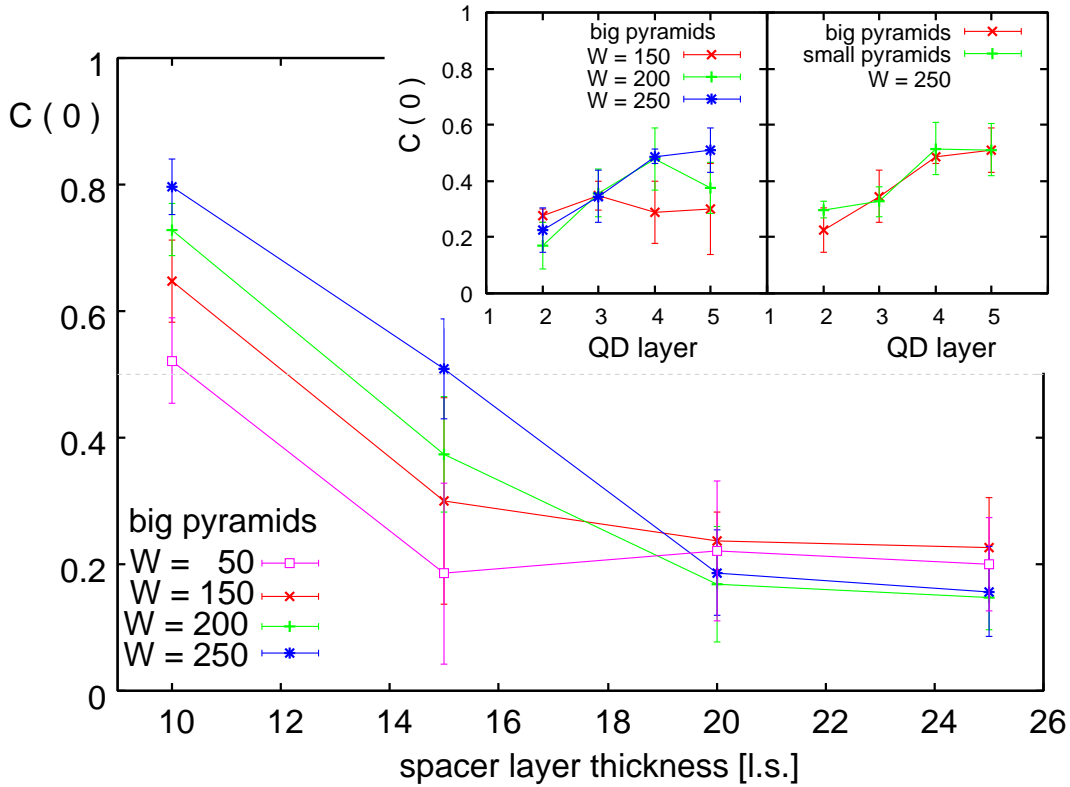


**Figure 6.4:** Cross-correlation coefficient  $C(0)$  of simulated quantum dot stacks in dependence of the spacer layer thickness with various values for the strain weight  $W$  (see text). First layer of the growth simulation is a prepatterned structure consisting of  $5 \times 5$  pyramids with a base length of 11 l.s. and a height of 7 l.s. Left inset: evolution in dependence of the layer number with fixed spacer layer thickness of  $d = 15$  l.s. Right inset: two different samples as first layers were used with  $d = 15$  l.s. and  $W = 250$  (see text). Parameters:  $T = 700$  K,  $c = 0.3\%$ ,  $F = 0.01$  ML/s  $100 \times 100$  l.s. simulation area, simulation time of 50 s for each QD layer. Average over five runs was taken. Error bars show the standard deviation. As a guide for the eye the value  $C(0) = 0.5$  is marked as a grey dotted line. Main figure:  $C(0)$  between the last (fifth) and preceding (forth) QD layer is shown. Insets:  $C(0)$  of the  $n$ th and  $(n - 1)$  layer is presented.

correlation of the islands should be visible if the spacer layer is about twice as thick as the height of the first layer (see Fig. 6.2). In our simulation, this is the case with a spacer layer thickness of  $d \approx 15$  l.s. At this value the cross-correlation coefficient  $C(0)$  of the structure grown with  $W = 250$  is  $C(0) \approx 0.5$ , indicating vertical correlation, whereas the samples grown with  $W = 150$  and  $W = 200$  are below this value. All further investigations such as the occurrence of the anticorrelated vertical stacking mode, support the choice of the strain weight  $W = 250$ .

Moreover, the evolution of the cross-correlation coefficient in dependence of the

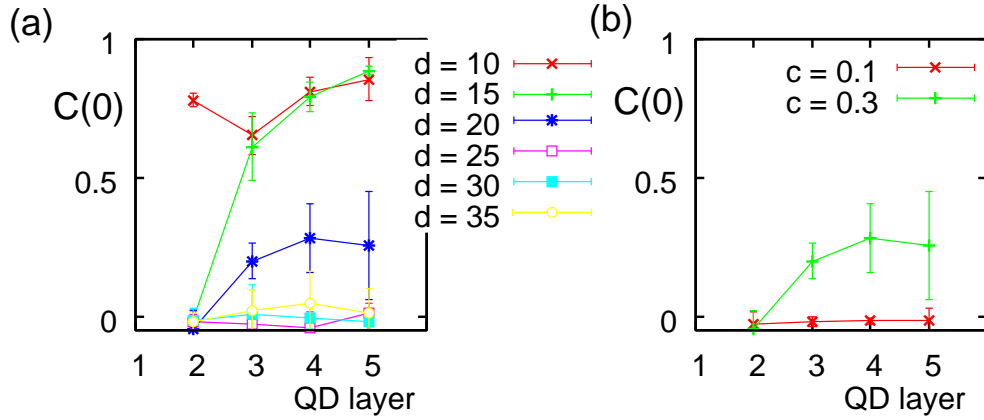


**Figure 6.5:** Cross-correlation coefficient  $C(0)$  of a quantum dot stack. First layer of the growth simulation is a prepatterned structure consisting of  $5 \times 5$  pyramids with a base length of 11 l.s. and a height of 7 l.s. Parameters:  $T = 700$  K,  $c = 0.3$  (a),  $F = 0.01$  ML/s, simulation area  $100 \times 100$  l.s., simulation time 50 s, spacer layer thickness  $d = 20$  l.s. (b),  $W = 250$ , average over five runs was taken.

sequence of QD layers is shown in the insets of Fig. 6.4. While for a strain weight of 250 the value of  $C(0)$  continuously increases, for  $W = 50$  and  $W = 150$  over the whole stack, almost no correlation could be observed. In the intermediate case of  $W = 200$  in the fourth layer a maximum is reached and the correlation drops down after that. An explanation is given below. The right inset shows the same quantities for fixed  $W$ . Two different samples were used as first prepatterned layers. One with small pyramids and another one with bigger ones (Fig. 6.3). Surprisingly the degree of vertical correlation is nearly the same for both structures, although one could expect that the bigger pyramids build up a strain field which is a bit stronger and therefore the degree of correlation should be higher in this sample, too. Also from simulations shown below it seems that the geometrical two-dimensional shape of the strain field together with the preferred island size, determined by the growth parameters like flux and temperature, competes with the strength of the strain field, which forces new islands to nucleate at certain positions. Lower absolute values of the strain field do not automatically lead to a lower degree of vertical stacking and vice versa.

In this sense the curve of the left inset in Fig. 6.4 for  $W = 200$  is an intermediate case, too. From the curves of each of the five individual runs (not shown) the possibility of the occurrence of a numerical error can be eliminated. For other values of  $W$  successively the preferred island size can be reached and the strain field is strong enough to give rise to nucleation centers above and the ordering on overall increases with increasing layer number *or* the strain field is too weak to induce vertical alignment. For a value of  $W = 200$  the behavior is different. While the strain field wins clearly up to the fourth layer on average, in some runs the stochastic nature of growth leads to fluctuations in the island positions, such that sometimes in the third, sometimes in the

second layer, the effect of strain induced ordering becomes of lower importance (since its absolute value is too weak to overcome the fluctuations) and finally the lateral fluctuations become predominant.

In Fig. 6.5 the cross-correlation coefficient  $C(0)$  of quantum dot stacks, grown on a prepatterned first layer, is shown. An average over five growth simulations was taken. For a fixed coverage the thickness  $d$  of the spacer layer was varied and vice versa. For a fixed spacer layer thickness this quantity is shown for two coverages  $c$ . It is obvious, and not surprising, that the degree of vertical alignment increases with decreasing spacer layer thickness. For thicknesses of  $d = 25$  l.s. and higher no correlations can be observed. In the cases of  $d = 15$  and  $d = 20$  l.s. the vertical correlation gets more pronounced with each subsequently grown layer. This feature also is known from experiments. But the curve for  $d = 10$  l.s. does not show a monotonic behavior. The second layer follows the spatial arrangement of the prepatterned first one. After that, the value of  $C(0)$  drops down and again increases with layer number four and five. The explanation for this is not too hard. The very first layer consists of optimal spatially arranged islands, which induce a regular array of nucleation sites in the second layer. Since the spacer layer thickness is in this case as thin as possible, the strength of the strain field is very strong, such that the nucleation of islands nearly follows the structure of the buried ones. But the word nearly must be underlined. In fact small deviations of island positions occur. So in the next layer the spatial arrangement does not follow the given pattern and the cross-correlation coefficient drops down. Moreover in this layer the ‘natural island size’ is achieved. The optimal arrangement in the very first layer was able to squeeze the next layer not only to a specific positioning but also to a certain island size. Due to small fluctuations in the second layer this ability is lost in the third layer. There, another (mean) island size dominates which is in fact a bit larger than the size of the pattern. In the preceding growth finally, this size ‘wins’ and the value of  $C(0)$  again increases, while the degree of optimal lateral spatial arrangement decreased.

With the above given explanation the other curves of Fig. 6.5 for  $d = 15$  and  $d = 20$  l.s. can be interpreted not only as simply an increased ordering in the subsequent grown layers. In fact this argument is doubtful with respect to the perfect laterally aligned first layer. Instead it turns out that layer by layer the sample enforces its own island size and the more this is achieved the better the degree of vertical correlations is.

The right panel of Fig. 6.5 shows simulations with two different coverages. For a low coverage of  $c = 10\%$  no correlations at all are to be seen. Since the island size increases with increasing coverage and the strength of the strain field is proportional to the volume of the given structure, it is clear that with increasing coverage (e.g.  $c = 30\%$ ) the influence of the strain field is increasing and therefore with increasing coverage the degree of vertical alignment is rising, too.

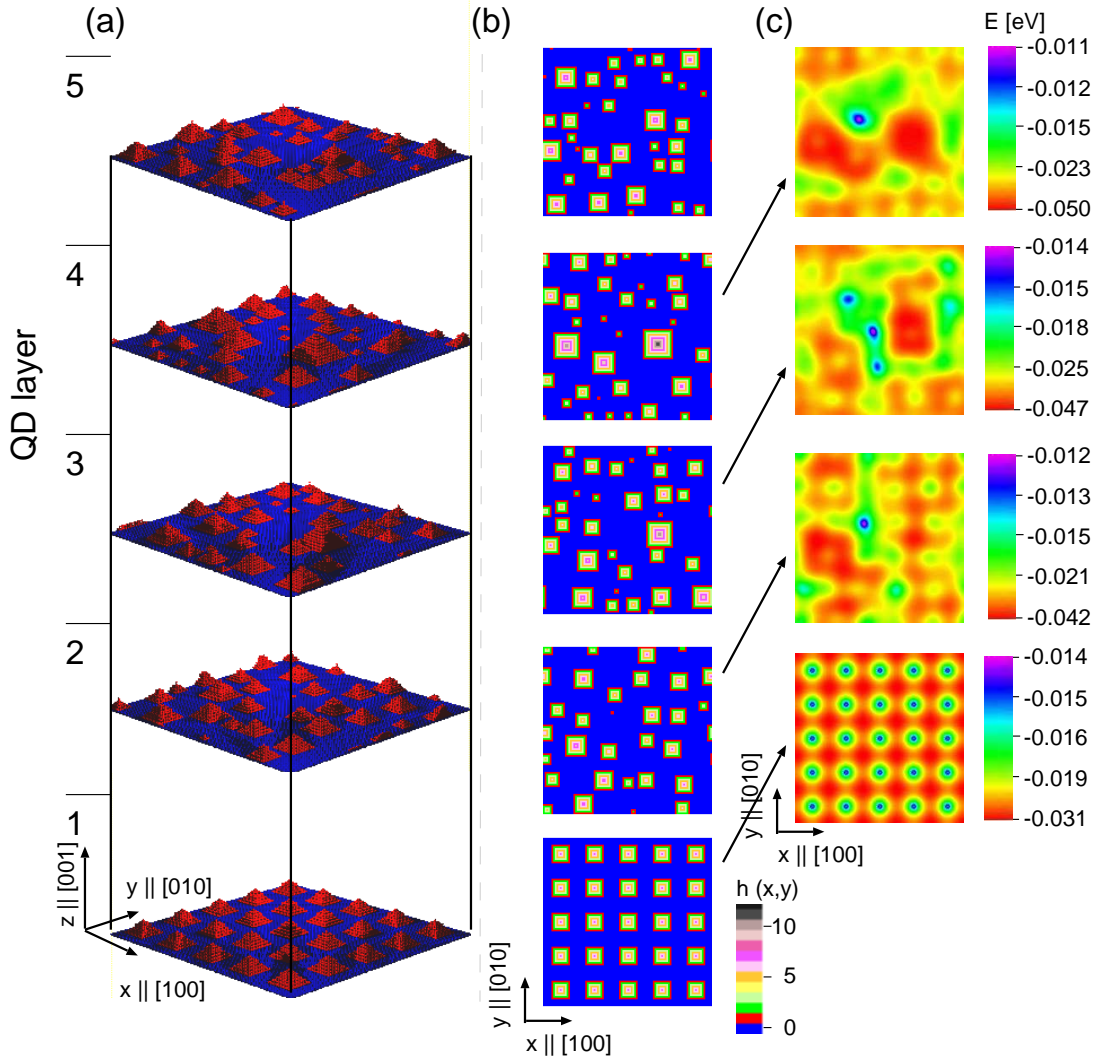


**Figure 6.6:** Simulations of quantum dot stacks in the anticorrelated growth mode. One example of a QD stack is shown in perspective views (a) and from the top (b). The strain fields generated by the previous grown QD layer ( $n - 1$ ), which is superposed in the growth simulation of the QD layer  $n$ , can be seen in (c). A cut through this sample along the  $[110]$ -direction is shown in Fig. 6.7. First layer of the growth simulation is a prepatterned structure consisting of  $5 \times 5$  pyramids with a base length of 11 l.s. and a height of 7 l.s. Parameters: Spacer 20 l.s.,  $T = 700\text{K}$ ,  $c = 0.3$ ,  $F = 0.01\text{ML/s}$ , simulation time 50 s,  $100 \times 100$  l.s. simulation area,  $W = 250$ .

### 6.1.2 Vertical anticorrelated growth

After examining the vertically correlated growth regime in the previous section, the next step is to focus on the anticorrelated stacking mode. As already shown in Chapter 4 in p. 55 and in particular in Sec. 4.2 we are able to examine the strain field of a

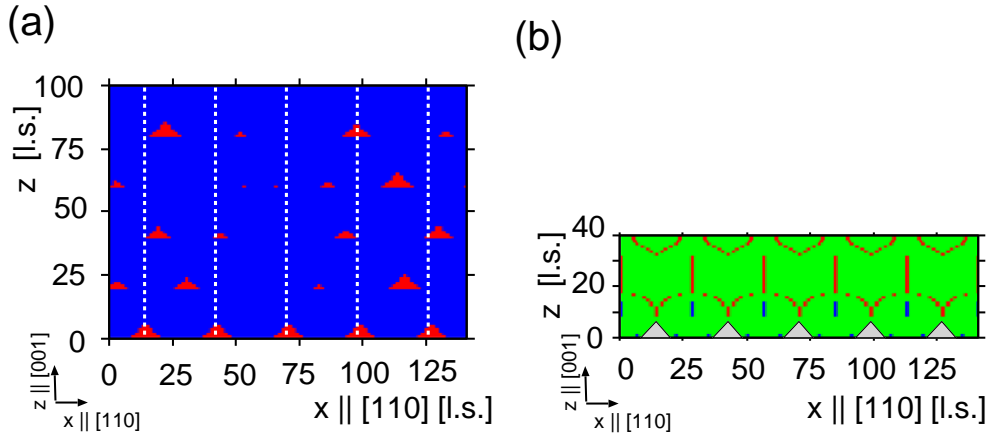


**Figure 6.7:** (a) Cut through a stacked quantum dot structure along the  $[110]$  direction. First layer of the growth simulation is a prepatterned structure consisting of  $5 \times 5$  pyramids with a base length of 11 l.s. and a height of 7 l.s. See also Fig. 6.6. Parameters: Spacer 20 l.s.,  $T = 700\text{K}$ ,  $c = 0.3$ ,  $F = 0.01\text{ML/s}$ , simulation time 50 s,  $100 \times 100$  l.s. simulation area,  $W = 250$ . The dotted lines are guides for the eye. (b) elastic strain field of the first layer. The minimum (maximum) of the elastic energy is shown in red (blue). The positions of the QDs are indicated by grey triangles.

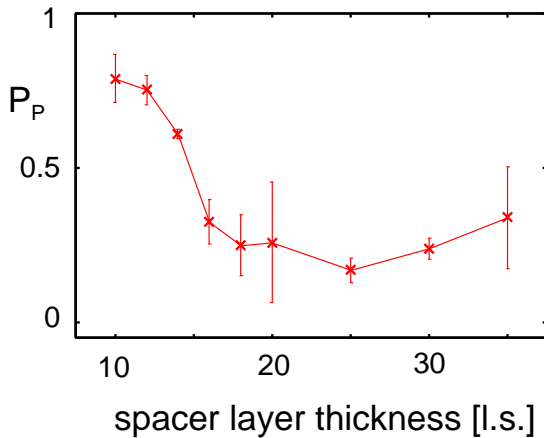
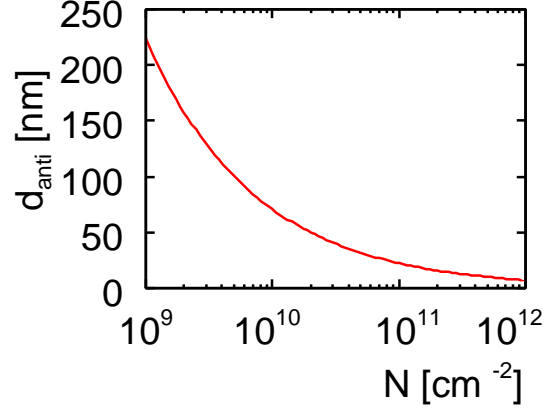


**Figure 6.8:** Pairing probability of a growth simulation with prepatterned substrate. First layer of the growth simulation is a prepatterned structure consisting of  $5 \times 5$  pyramids with a base length of 11 l.s. and a height of 7 l.s. Parameters:  $T = 700\text{K}$ ,  $c = 0.3$ ,  $F = 0.01\text{ML/s}$ ,  $100 \times 100$  l.s. simulation area, simulation time 50 s,  $W = 250$ .

given structure. This helps to forecast the alignment mode specifically if the first layer is known, as is in this section. From Fig. 6.7 (b) one can see that with this configuration for spacer layers  $d < 15$  l.s. correlated growth is likely to occur. For higher values of  $d$  a transition to anticorrelated stacking can be expected, which is dominant for example at  $d = 20$  l.s. While the anticorrelated mode should still be intact for  $d > 20$  l.s. up to  $d < 40$  l.s., we keep in mind that strain effects strongly decay with increasing distance from the source, and therefore at some point for the spacer layer thickness only random growth can be expected.

In Fig. 6.7 (a) one cut along the growth direction through a simulated quantum

**Figure 6.9:** Spacer layer thickness  $d_{\text{anti}}$  for anticorrelated growth of an optimal laterally arranged array of QDs in dependence of their density. Material parameters of GaAs were used. See Eq. (6.4).



dot stack is shown. It is easy to be seen that indeed most of the islands are vertically anticorrelated. To quantify this behavior in Fig. 6.8 the pairing probability  $P_p$  for different spacer layer thicknesses is shown. As explained in detail in the Appendix B.2

$$P_p = \begin{cases} 1 & \text{correlation} \\ 0.5 & \text{random distribution} \\ 0 & \text{anticorrelation} \end{cases} \quad (6.3)$$

Indeed as expected by inspecting the strain field in Fig. 6.7 (b), a transition from correlated growth up to spacer layer thicknesses of  $d \lesssim 13$  l.s. via randomly distributed island growth to anticorrelated growth for  $d < 30$  l.s. can be observed in Fig. 6.8. The degree of anticorrelation is however low, i.e.  $P_p > 0$ , caused by lateral fluctuations of the island positions and sizes. For  $d \gtrsim 30$  l.s. all (anti) correlation properties are lost.

At this point the reader is probably a bit surprised. As pointed out before, our grid is in the unit of the lattice constant of the parent material GaAs ( $a_{\text{GaAs}} = 0.565$  nm). So the transition point evaluated in this work is at approximately 8 nm, the vertical anticorrelated growth occurs at  $d \approx 11$  nm and the vertical alignment is completely lost for spacer layer thicknesses larger than  $d \approx 20$  nm. Other experimental results are different. For example, anticorrelated growth has been observed for spacer layer thicknesses of about  $d \approx 45$  nm by Wang *et al.*, using the same parent material system [Wan04]. This discrepancy, can be explained as follows: in the previous chapters it was proven that the propagation of the strain field in our model is computed accurately. The only point which influences the transition point and therefore might be responsible for this discrepancy is the lateral positioning of the islands. The island size only has an impact on the strength of the strain field. So, presuming a regular size and spatial distribution, the point that really matters turns out to be the island density. In the simulations shown, this quantity is for the array of small pyramids, which was used as first layer, in the order of  $10^{11} \text{ cm}^{-2}$ . The island density for the sample shown in [Wan04] is not given, but for MOCVD grown InAs/GaAs quantum dots this is typically of about  $10^{10} \text{ cm}^{-2}$  [Hei97a]. To quantify the consequences of the differences in the island

density, simple geometrical considerations will be carried out: we consider an array of quantum dots with a given density  $N$ . Presuming a regular lateral ordering such that the island positions are on a square quadratic mesh, the island-island distances can be easily calculated. The value of the material-dependent propagation direction of the strain field minima is  $\theta_{\min} = 45^\circ$  for GaAs as parent material (Sec. 4.2.3). The spacer layer thickness  $d_{\text{anti}}$ , where optimal anticorrelated growth is expected to occur can be computed by

$$d_{\text{anti}} = \frac{1}{\sqrt{2N} \tan \theta_{\min}}, \quad (6.4)$$

which is depicted in Fig. 6.9. In this simple picture for  $N = 3.510^{11} \text{ cm}^{-2}$  we gain  $d_{\text{anti}} \approx 12 \text{ nm}$  and for  $N = 2.510^{10} \text{ cm}^{-2}$  a value of  $d_{\text{anti}} \approx 45 \text{ nm}$ . This difference explains the deviation of the transition point from correlation to anticorrelation in experiment and our simulations.

### 6.1.3 2D to 3D transition

Experimentally it was reported that the transition point from flat, two-dimensional to three-dimensional island growth in quantum dot stacks occurs at earlier stages [Dun01], corresponding to a lower coverage. Previously it was shown that in our simulations for one layer of quantum dots at a temperature of  $T = 700 \text{ K}$  this transition takes place at coverages higher than 30% (Sec. 5.3.2, p. 81). For  $c = 30\%$  all atoms are located in the first monolayer (Fig. 5.4). This behavior changes if one investigates the growth of quantum dot stacks. In Fig. 6.10 the number of atoms in the first layer is shown for the second and the last (fifth) quantum dot sheet of a quantum dot stack in dependence of the spacer layer thickness  $d$ . In contrast to the simulation of individual, single layers in nearly all cases shown in Fig. 6.10, the value of the critical coverage  $c_c$  is below 30%. The reason is the additional strain field coming from the layers beneath the growth plane. So, with every additional quantum dot layer, the additional contributions of the strain field lead to a lowering of  $c_c$ . Of course this is only true up to a certain spacer layer thickness  $d$ . If  $d$  is too large the influence of the previously grown layers vanishes, namely for  $d > 16 \text{ l.s.}$ , and the value of  $c_c$  tends again to that of single quantum dot layers.

## 6.2 Growth on flat surfaces

After examining the growth properties of stacked structures with prepatterned substrate, here simulations which start ‘from scratch’ are discussed. Now already in the very first layer deviations from optimal lateral spatial arrangements occur. Therefore it is much harder to achieve optimal vertical ordering. In particular, in this setup we have not been able to identify anticorrelated stacking of quantum dots.

Improving the spatial ordering is possible, in principle, using a slightly modified kinetic Monte Carlo routine [Mei03a]. But it would require the consideration of, e.g.,

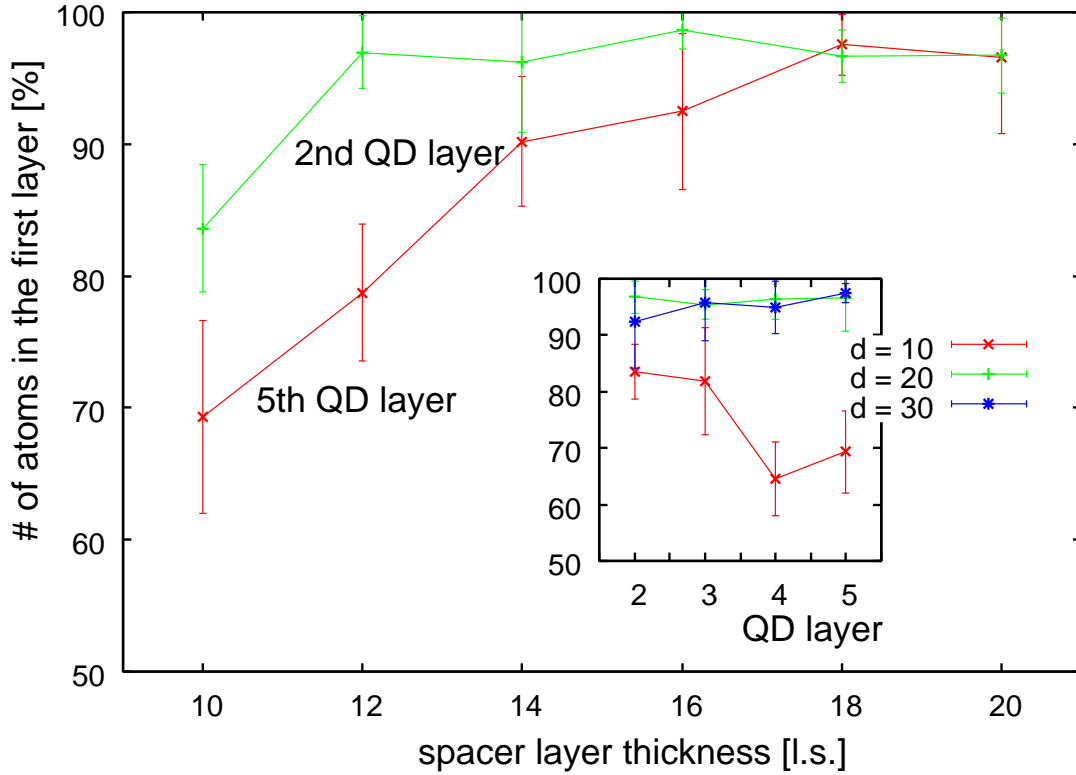


**Figure 6.10:** Percentage of atoms in the first layer in dependence of the spacer layer thickness  $d$  for the second and the fifth layer (sheet) of a quantum dot stack. Inset: the percentage of atoms in the first layer is shown for the four subsequent grown layers (sheets) of the quantum dot stack for different values of  $d$ . First layer of the growth simulation is a prepatterned structure consisting of  $5 \times 5$  pyramids with a base length of 11 l.s. and a height of 7 l.s. Parameters:  $T = 700\text{K}$ ,  $c = 0.3$ ,  $F = 0.01\text{ML/s}$   $100 \times 100$  l.s. simulation area, simulation time 50 s,  $W = 250$ . Average over five runs was taken.

binding bonds to next nearest neighbors, and with that the simulation would be computationally more expensive. Depending on the CPU and the growth parameters chosen (the temperature), the simulation of one QD layer needs a computation time of ten hours. As an example: in Fig. 6.11 (a), 12 data points are plotted, each representing the average over five runs. For calculating the values of this figure alone, a total computation time of about 25 days on one CPU (e.g. AMD Athlon MP 2000+) was needed. This short consideration might explain the necessity for using the simplest algorithm possible. In future works, the simulation of QD arrays taking into account effects leading to improved spatial ordering, would be challenging. Since the computational power steadily increases it seems to be a realistic task, moreover if one decides to use more efficient algorithms, such as the one introduced in Sec. 2.3.

Fig. 6.11 (a) shows the cross-correlation coefficient of quantum dot stacks. It turns

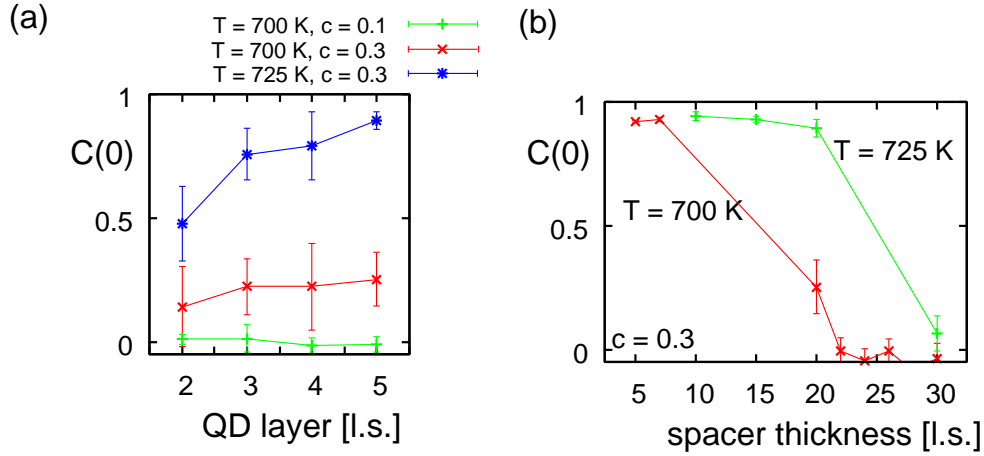


**Figure 6.11:** Cross-correlation coefficient  $C(0)$  of stacked QD structures.  $C(0)$  for subsequent QD layers is shown (a), spacer layer thickness  $d = 20$  l.s.  $C(0)$  only for the top layers are shown in (b). Parameters:  $F = 0.01\text{ML/s}$ ,  $100 \times 100$  l.s. simulation area, simulation time of 50 s per QD layer,  $W = 250$ . Average over 5 runs.

out that in certain parameter windows the vertical ordering improves for each layer successively. While for temperatures of  $T = 700$  K with a coverage of  $c = 10\%$  no influence of the stacking can be seen, the quantum dots grow at random positions. An increase of the coverage to  $c = 30\%$  induces a slight vertical stacking. The reason is again the island size which is increased with increasing coverage. Therefore, the strain field becomes stronger and can influence the adatom movements and nucleation processes in the second and higher layers. A further increase of the island size by increasing the temperature to a value of  $T = 725$  K does not only improve the vertical ordering, which again becomes better layer by layer, but also induces a more uniform stacking, which manifests itself in a lowering of the standard deviation.

The same trend can be observed in Fig. 6.11 (b). Here, only the value of  $C(0)$  is shown for the two last layers in dependence of the spacer layer thickness. While for  $T = 700$  K no vertical correlation is to be found, for spacer layer thicknesses larger than  $d > 20$ , and for  $T = 725$  K, the strain induced vertical ordering can be seen up to  $d \approx 25$ .

In Fig. 6.14 growth simulations of QD stacks consisting of a relatively large number of QD layers were performed. For spacer layer thicknesses of  $d = 25$  and  $d = 30$  l.s. no vertical correlations can be seen. In the case of  $d = 20$  l.s. for the first QD layers at least a slight vertical correlation can be observed, even if the degree of correlation is low, however. Obviously the value of correlation is too low to induce an increase of the vertical ordering in the following layers, instead the value of the cross-correlation coefficient continuously decreases with increasing layer number.

As an example which can be directly compared to experimental transmission electron microscopy (TEM) or scanning tunneling microscopy (STM) images (see

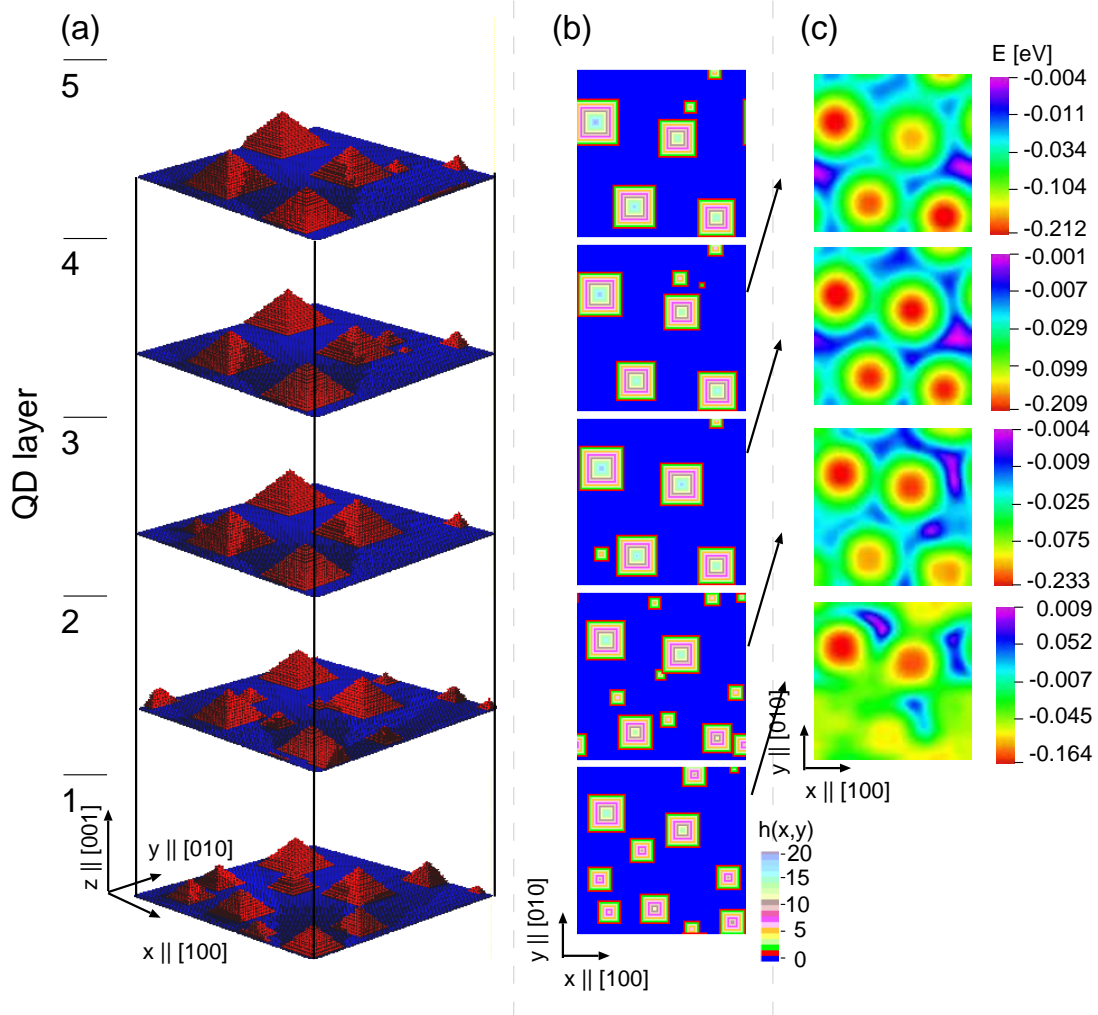


**Figure 6.12:** An example of a simulated vertically correlated QD stack. Perspective and top views of every layer are shown in (a) and (b) respectively. The strain fields generated by the previous grown QD layer ( $n - 1$ ), which is superposed in the growth simulation of the QD layer  $n$ , can be seen in (c). See Fig. 6.13. Parameters:  $d = 20$  l.s.,  $T = 725\text{K}$ ,  $c = 0.3$ ,  $F = 0.01\text{ML/s}$   $100 \times 100$  l.s. simulation area,  $W = 250$ .

(Fig. 6.15, Fig. 6.16, Fig. 6.1, and Fig. 6.2), a cut through the spacer layer of one of the grown samples along the  $[100]$ -direction is shown.

### 6.3 Summary

In this chapter the major issue of the thesis, as indicated by its title, was treated. The combination of a kinetic Monte Carlo scheme and a three-dimensional, anisotropic strain field model, was applied to investigations concerned with the self-organized

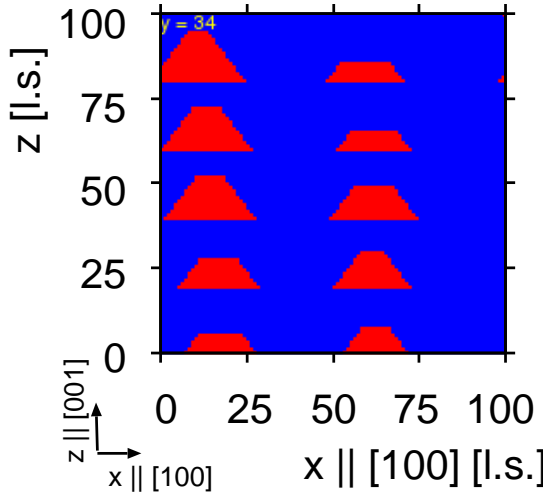


**Figure 6.13:** Cut through a stacked QD structure along the [100] direction. Figures of all layers of the QD stack are shown in Fig. 6.12. Parameters:  $d = 20$  l.s.,  $T = 725\text{K}$ ,  $c = 0.3$ ,  $F = 0.01\text{ML/s}$   $100 \times 100$  l.s. simulation area,  $W = 250$ .

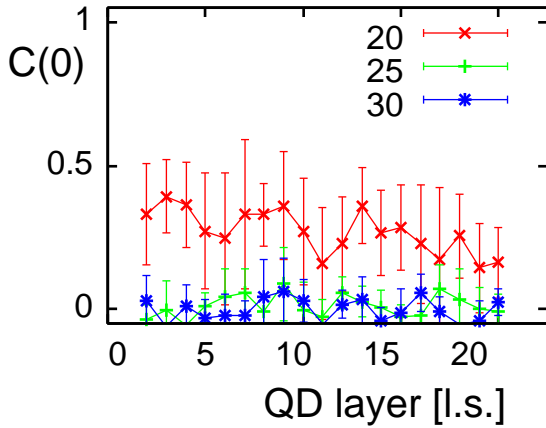


**Figure 6.14:** Cross-correlation coefficient  $C(0)$  of 20-layer QD stacks for different spacer layer thicknesses  $d$ . Parameters:  $T = 700\text{K}$ ,  $c = 0.3$ ,  $F = 0.01\text{ML/s}$   $100 \times 100$  l.s. simulation area,  $W = 250$ .

growth of arrays of QD stacks. Within our strain field model we were able to take into account the occurrence of both tensile and compressively strained regions. While the first lowers the diffusion barrier, the latter gives rise to favorable regions which might act as nucleation centers for impinging adatoms.

To simulate vertically correlated QDs it was necessary to amplify the strain field by a factor attributed to effects which are not explicitly modeled here, such as surface reconstructions, morphological aspects in the spacer layer and/or the chemical composition, or kinetic effects during growth.

Using prepatterned substrates, experimental findings could be proven. The degree of vertical correlation was investigated by measuring the cross-correlation coefficient and the pairing probability. The influence of various experimentally accessible parameters like the flux rate, coverage, temperature, and the thickness of the spacer layer was studied and discussed.

As requisite for vertical ordering effects, a combination of both high degree of lateral ordering in each sheet of QDs, and strain induced energy sinks (i.e. nucleation centers) of an appropriate lateral size and absolute value, is required.

**Figure 6.15:** Cross-sectional scanning tunneling microscopy image of a threefold QD stack, grown by metalorganic chemical vapor deposition. Material: InAs/GaAs. Taken from [Fle99].

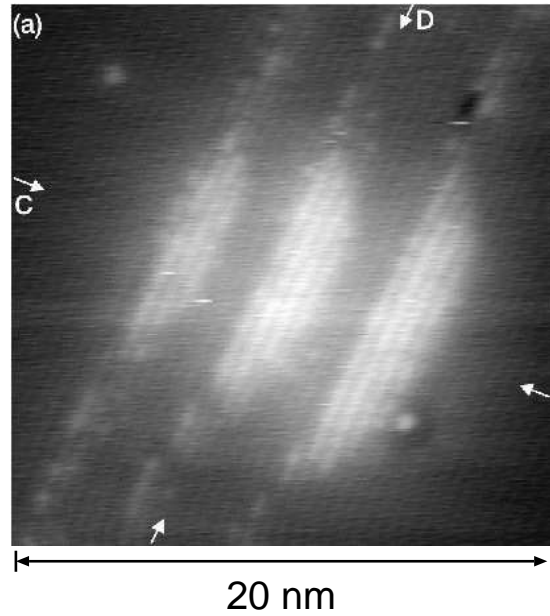
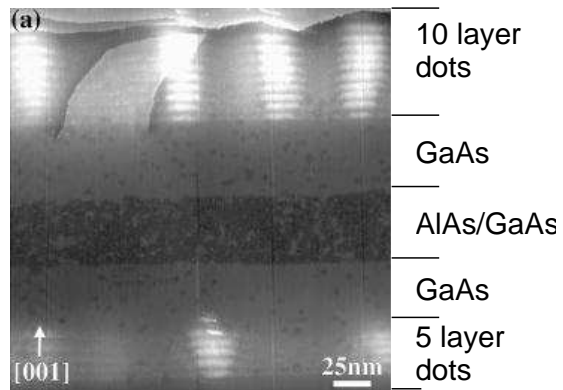


**Figure 6.16:** Cross-sectional scanning tunneling microscopy image of 10- and 5-layer stacks of MBE grown InAs/GaAs quantum dots. Material: InAs/GaAs. Taken from [Lit99].



By tuning the spacer layer thickness  $d$ , vertically anticorrelated structures can be grown. The particularly needed value of  $d$  can be forecast within our strain model for arbitrarily shaped arrays of QDs. In contrast to the vertically correlated regime, this growth mode occurs for larger values of  $d$ . Since with larger  $d$  the absolute value of the strain field decreases significantly the efficiency of strain mediated ordering effects decrease as well. Using prepatterned structures, however, we were able to show the transition from correlated to anticorrelated growth. The difference in the value of the transition point between theory and experiments could be attributed to differences in the QD density.

In the growth of QD stacks it was shown that the transition from two-dimensional growth to three-dimensional island formation in the subsequently grown QD layers occurs at earlier stages. This finding could be proven, too, and was examined in dependence of the spacer layer thickness.

---

Due to the low lateral regularity of QD arrays grown on flat surfaces, in our simulations the regime of vertical anticorrelation could not be observed and, in general, the degree of vertical correlation was low.



# Chapter 7

## Conclusions and Outlook

In this work the self-organized growth of semiconductor quantum dot stacks was studied by combining two powerful techniques. The first is a kinetic Monte Carlo scheme for modeling adatom diffusion and simulating the growth of quantum dot fundamentals. In the second, the anisotropic three-dimensional strain field was computed for arbitrarily shaped quantum dots in the framework of elasticity theory and only the material dependent elastic constants enter as input parameters. During the growth simulations both were taken self-consistently into account. The two-dimensional strain field of islands in the growing layer and the three-dimensional strain field resulting from the islands in all quantum dot layers beneath the growth plane.



A detailed derivation of the computationally efficient method for calculating the strain field of arbitrarily shaped islands was given and comparison with an atomistic approach [Ham06] for calculating the strain field and with other theoretical studies [Hol99] proved the correctness and exactness of our computations. It was shown that results of such calculations already offer insights into various aspects of the self-organized growth of vertically aligned nanostructures.

We investigated the three-dimensional strain field of various arrays of islands embedded in different semiconducting parent materials, and mainly focused on the vertical propagation of the strain field, in particular the propagation of the strain field minima which might serve as nucleation sites. It is known that the features of the strain field of one single inclusion, i.e. a quantum dot, are mainly governed by its volume and center of mass, and the elastic properties of the parent material. If one considers a periodic array of islands in contrast to one single inclusion, the inclination angle of the strain field minima decreases. This finding explains experimentally found vertical stacking positions [Wan04] in the InAs/GaAs material system. By further taking into account an arbitrarily shaped array of islands rather than calculating the strain field of point-like inclusions, leads to an extended region where the strain field minima are to be found directly above the islands. But the value of the spacer layer thickness for

which vertically anticorrelated growth is likely to occur remains unchanged. The investigation of various materials has shown that an increasing anisotropy ratio  $A$  leads to increasing inclination angle for the strain field minima, in general, and the transition point from correlated to anticorrelated positions of the strain field minima decreases while the region of transition is enlarged.



First we used the combination of the strain field with kinetic Monte Carlo simulations for investigations concerning growth kinetics of single quantum dot arrays before proceeding to the major topic—the growth of stacked quantum dot arrays. The influence of experimentally accessible parameters like the flux rate, the temperature and the coverage, agreed to both, experimental results and theoretical studies done previously in our group with a simplified anisotropic model [Mei01b], and an isotropic strain model [Mei03a], respectively.

In contrast to these investigations our kinetic Monte Carlo simulation routine was optimized for the purpose of the computationally expensive task of simulating the growth of quantum dot stacks. This led to a lower degree of spatial and size ordering of the quantum dot arrays as main difference in comparison with the earlier findings.

The main advantage of our model is, that not only the two-dimensional anisotropic strain can be calculated and self-consistently incorporated in the growth simulations, but rather a fully three-dimensional model capable of calculating the strain field of arbitrarily shaped islands was derived, which was used for the simulation of quantum dot stacks.



The use of a prepatterned surface as first layer for the growth of semiconductor quantum dot stacks can also be found in many experiments. This method offers the possibility to study the growth of islands under the influence of a well defined energy surface, i.e. the strain field of the prepatterned structure at the growth plane. Therefore, we have chosen two sample structures consisting of periodic arrays of islands, large pyramids and smaller pyramids. On these we carried out growth simulations of subsequent quantum dot layers.

It turned out that, as theoretically predicted [Pri01], the influence of the strain field is too low to induce vertical ordering of islands. Therefore an additional factor was introduced, attributed to effects which are not modeled within this work, such as surface reconstructions, morphological aspects in the spacer layer and/or the chemical composition, or kinetic effects during growth, was introduced. With this we were able to reproduce both vertical correlated and vertical anticorrelated growth of islands and showed the transition from one to the other for increasing spacer layer thicknesses. The transition point, however, was found to be at lower values for the spacer layer thickness than experimentally observed [Wan04]. We could explain this discrepancy by differences in the quantum dot density. The improvement of the vertical ordering

with increasing layer number could not be seen in our simulations. This might be due to stochastic fluctuations of the quantum dot positions.

The transition of two-dimensional to three-dimensional island growth in the subsequently grown quantum dot layers was investigated, too. In agreement with experiments we found the transition taking place at earlier stages of growth. Since for increasing spacer layer thickness the influence of the buried sheets becomes lower, the transition point increases up to the value found in the growth of single layers of quantum dots.



Simulating quantum dot stacks starting with initially flat surfaces resulted in structures exhibiting only low vertical alignment, in general. Only the correlated growth regime could be identified. It was found that as prerequisite for vertical alignment not only strain induced nucleation centers of a sufficient strength and lateral size are required. Moreover, a high degree of inherent spatial and size ordering in each quantum dot layer is necessary.



As a main contribution of this work the approach for modeling the three-dimensional anisotropic strain field has shown to give promising results. The implementation of this model into a kinetic Monte Carlo approach proved its capability to model structures of high experimental relevance. It turned out, however, that most of the computation time is needed for simulating the adatom movement. As a further improvement a more refined model for simulating the growth kinetics should be considered. More refined and improved concerning the computation time, and taking into account a higher number of relevant processes for island formation [Kra02b]. Since the latter raises even more the computational effort, the key point is the first. One possible approach, namely the adatom-density kinetic Monte Carlo method [Man03], was sketched within this thesis. The further development of this method and the implementation of the elastic strain field developed here, seems to be a challenging task.



# Appendix A

## Equivalence of strain field models

An approach—only applicable to two-dimensional problems—was suggested by Shchukin *et al.* [Shc99b] and used in [Mei01b]. Starting from the numerical solution of Green's tensor in  $k$ -space rules were obtained to calculate directly the tensor in real space. Having this, one can write down the strain tensor and the resulting Helmholtz free energy. Here, the equations are listed for a quick overview and direct comparison. The detailed calculation can be found elsewhere [Fel03].

The components of the Green's tensor are as follows:

$$G_{xx}(\mathbf{r}_{\parallel}; 0, 0) = \frac{1}{2\pi c_{44}} \frac{1}{r_{\parallel}} \left[ m_y^2 h_{11}(\mathbf{m}) + m_x m_y h_{12}(\mathbf{m}) + m_x m_y h_{21}(\mathbf{m}) + m_x^2 h_{22}(\mathbf{m}) \right], \quad (\text{A.1a})$$

$$G_{xy}(\mathbf{r}_{\parallel}; 0, 0) = \frac{1}{2\pi c_{44}} \frac{1}{r_{\parallel}} \left[ -m_x m_y h_{11}(\mathbf{m}) + m_y^2 h_{12}(\mathbf{m}) - m_x^2 h_{21}(\mathbf{m}) + m_x m_y h_{22}(\mathbf{m}) \right], \quad (\text{A.1b})$$

$$G_{yx}(\mathbf{r}_{\parallel}; 0, 0) = \frac{1}{2\pi c_{44}} \frac{1}{r_{\parallel}} \left[ -m_x m_y h_{11}(\mathbf{m}) - m_x^2 h_{12}(\mathbf{m}) + m_y^2 h_{21}(\mathbf{m}) + m_x m_y h_{22}(\mathbf{m}) \right], \quad (\text{A.1c})$$

$$G_{yy}(\mathbf{r}_{\parallel}; 0, 0) = \frac{1}{2\pi c_{44}} \frac{1}{r_{\parallel}} \left[ m_x^2 h_{11}(\mathbf{m}) - m_x m_y h_{12}(\mathbf{m}) - m_x m_y h_{21}(\mathbf{m}) + m_y^2 h_{22}(\mathbf{m}) \right]. \quad (\text{A.1d})$$

with  $\mathbf{r}_{\parallel}$  the in-plane vector between two elastic inclusions, i.e. two quantum dots, where the functions  $h_{ab}$  are defined by

$$h_{11}(\mathbf{m}) = \left[ A_{11} + 8B_{11} \left( m_x^2 m_y^2 - \frac{1}{8} \right) \right], \quad (\text{A.2a})$$

$$h_{12}(\mathbf{m}) = 4B_{12} m_x m_y (m_y^2 - m_x^2) \left[ 1 + 8C_{12} \left( m_x^2 m_y^2 - \frac{1}{8} \right) \right], \quad (\text{A.2b})$$

$$h_{21}(\mathbf{m}) = 4B_{21} m_x m_y (m_y^2 - m_x^2) \left[ 1 + 8C_{21} \left( m_x^2 m_y^2 - \frac{1}{8} \right) \right], \quad (\text{A.2c})$$

$$h_{22}(\mathbf{m}) = \left[ A_{22} + 8B_{22} \left( m_x^2 m_y^2 - \frac{1}{8} \right) \right]. \quad (\text{A.2d})$$

and  $\mathbf{m} = (m_x, m_y)$  is the normalized unit vector, e.g.,  $\mathbf{m} = (\cos(\psi), \sin(\psi))$ . From Eqs. (A.1a)–(A.2d) it follows, that

$$\nabla_i \nabla_j G_{ij}(r_{\parallel}, \psi) = \frac{1}{r_{\parallel}^3} \frac{1}{2\pi c_{44}} (A_{11} + 15B_{11} \cos(4\psi)) \quad (\text{A.3})$$

with  $c_{44}$  the elastic modulus, and the material parameters

$$\begin{aligned} A_{11} &= -0.9661, \\ A_{22} &= -1.1765, \\ B_{11} &= -0.0677, \\ B_{12} &= B_{21} = 0.0926, \text{ and} \\ C_{12} &= C_{21} = -0.0780 \end{aligned}$$

for GaAs.

This solution behaves qualitatively similar to the solution developed here (see, e.g., Sec. 3.4, Eq. (3.57)). Differences in the material dependent parameters come from different applied fitting schemes.

# Appendix B

## Data analysis

### B.1 Cross-correlation function

In the theory of surface growth several measures have been introduced to characterize the properties of the studied samples. Given a set of  $N$  discrete points at a site  $\mathbf{r}_i$  with  $i \in \{0, \dots, N\}$  with a certain height profile  $h(\mathbf{r}_i)$  one can describe the roughness and the height fluctuations using the height-height correlation function

$$C^{hh}(\rho) = \langle \langle [h(\mathbf{r}) - \bar{h}]^* [h(\mathbf{r} + \Delta) - \bar{h}] \rangle_{\mathbf{r}} \rangle_{|\Delta|=\rho} . \quad (\text{B.1})$$

Here,  $\bar{h}$  denotes the mean surface height, “\*” the complex conjugate, which should be applied to correlation functions of more general complex quantities, and  $\langle \cdot \rangle$  the ensemble average. Moreover the root mean square (rms) roughness

$$w_{rms} = \langle (h(\mathbf{r}) - \bar{h})^2 \rangle^{\frac{1}{2}} \quad (\text{B.2})$$

is a commonly used measure. It describes fluctuations of surface heights around an average surface height. The rms roughness is connected to the above defined height-height correlation function via

$$C^{hh}(0) = w_{rms}^2 . \quad (\text{B.3})$$

Normalizing the height-height correlation function by the factor  $w_{rms}^2$  yields the spatial auto-correlation function.

Since this work is concerned with aspects of correlation of *two different* surfaces, e.g. a buried quantum dot array and a sheet of quantum dots on the top, we have to extend the definition Eq. (B.1).

Defining in-plane vectors with zero  $z$ -component denoted with a  $\parallel$  as subscript and introducing the superscripts  $S$  and  $B$  referring to the surface and the buried plane we write down the definition of the spatial cross-correlation function:

$$C(\rho) = \left\langle \left\langle [h^S(\mathbf{r}_{\parallel}) - \bar{h}^S]^* [h^B(\mathbf{r}_{\parallel} + \Delta_{\parallel}) - \bar{h}^B] \right\rangle_{\mathbf{r}_{\parallel}} \right\rangle_{|\Delta_{\parallel}|=\rho} . \quad (\text{B.4})$$

Given two sets of square meshes<sup>1</sup>  $S$  and  $B$ , with  $N \times N$  points  $i, j \in \{0, \dots, N\}$  a height function  $h_{i,j}^{S,B} : S, B \rightarrow \mathbb{N}$  and periodic boundary conditions, the previously defined continuous cross-correlation function turns into a cross correlation matrix implied by the discretization

$$C_{ij} = \frac{1}{N^2} \sum_k^N \sum_l^N (h_{k,l}^S - \bar{h}^S) (h_{(k+i),(l+j)}^B - \bar{h}^B) \quad (\text{B.5})$$

All indices have to be taken modulo  $N$  due to the periodicity. From this the radially dependent one-dimensional function can be obtained via averaging over the angle at fixed  $|\Delta_{\parallel}| = \rho$ .

The implementation of this definition is straightforward. But it turns out, that using the Wiener-Khinchin theorem [Kam03] instead of summing up by using a bunch of ‘for-loops’ gives a much higher performance [Els05b]: on current computer systems this method is about ten times faster. The higher the number of data points, the more important this fact becomes. With  $H^{S,B}$  as the Fourier transform of the normalized height profile  $h^{S,B}$  with  $\bar{h}^{S,B} = 0$

$$C(\Delta_{\parallel}) = \int h^{S*}(\mathbf{r}_{\parallel}) h^B(\mathbf{r}_{\parallel} + \Delta_{\parallel}) d\mathbf{r}_{\parallel} \quad (\text{B.6})$$

$$= \frac{1}{2\pi} \int H^{S*}(\boldsymbol{\omega}) H^B(\boldsymbol{\omega}) \exp\{-i(\boldsymbol{\omega} \cdot \Delta_{\parallel})\} d\boldsymbol{\omega} \quad (\text{B.7})$$

This function is directly applicable to simulation results of this work, since it corresponds to a two-dimensional correlation function with periodic boundary conditions. A one-dimensional function can be obtained by averaging over the angle at fixed radius

$$C(\rho) = \frac{1}{2\pi} \int C(\rho \cos \varphi, \rho \sin \varphi) d\varphi. \quad (\text{B.8})$$

The Wiener-Khinchin theorem is of course applicable to the height-height correlation function (Eq. (B.1)) in this way, too. Setting  $h^{S,B} = h$  one will come to the more convenient form, where the correlation function is given by the Fourier transform of the spectral density function  $S(\boldsymbol{\omega}) = |H(\boldsymbol{\omega})|^2$ .

A direct measure of the correlation is given by the cross correlation coefficient, which gives

$$C(0) = \begin{cases} 1 & \text{correlation} \\ 0 & \text{random distribution} \\ -1 & \text{total anticorrelation} \end{cases} \quad (\text{B.9})$$

Here, ‘total anticorrelation’ does *not* mean ‘anticorrelation’ as used in the field of QD stack growth. Rather, this describes the behaviour if one compares an image with its negative. Vertical anticorrelation of QD stacks refers to a situation, where islands

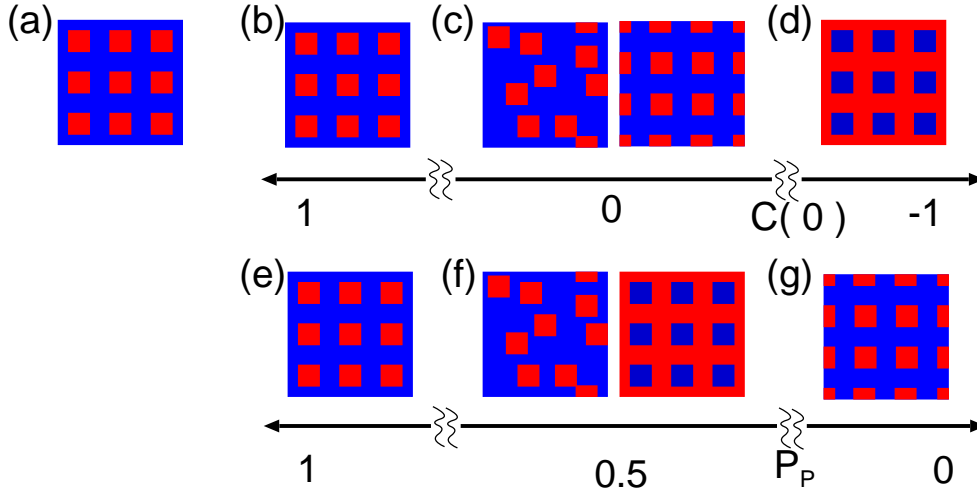


**Figure B.1:** Pairing probability and cross-correlation coefficient—the sketch illustrates the differences of the two quantities. In (a) the first layer is shown. Some possibilities for the second layer are given in (b–g) with the corresponding values for the cross-correlation coefficient  $C(0)$  (b–d) and the pairing probability  $P_p$  (e–g).

are growing at positions in between the islands of the layer beneath. Such a situation is depicted in Fig. B.1 with (a) as first and (g) as second QD layer.

An important feature of this function is the robustness against fluctuations. This is one of the reasons why in the field of image processing and analyzing this function is used often, e.g., for pattern recognition. On the other hand, anticorrelation, which is expected to occur in stacked structures, could not be detected using this quantity (Fig. B.1)

## B.2 Pairing probability

To quantify the degree of vertical correlations of stacked island structures the pairing probability  $P_p$  is often used [Xie95; Kie99; Gon01; Mei03b].

Denoting the distance of an island in one layer to the next island in the other layer by  $d'_{nn}$  and defining this measure in one layer to be  $d_{nn}$ , then geometrical considerations show, that the average of these two quantities  $\bar{d}'_{nn} = 0$  if the island positions coincide and  $\bar{d}'_{nn}/\bar{d}_{nn} = 1/\sqrt{2}$  if the positions in one layer are inbetween the one of the other layer. In order to have a pairing probability in the range of  $P_p \in [0, 1]$  we define it as

$$P_p = 1 - \sqrt{2} \frac{\bar{d}'_{nn}}{\bar{d}_{nn}} \quad (\text{B.10})$$

<sup>1</sup>in our case this can be identified with two lattices

which gives

$$P_p = \begin{cases} 1 & \text{correlation} \\ 0.5 & \text{random distribution} \\ 0 & \text{anticorrelation} \end{cases} \quad (\text{B.11})$$

Of course, the big advantage of this measure is the possibility to quantify all of the three growth regimes of interest with only one function. On the other hand it turns out that this function is very sensitive to deviations of the ‘optimal’ positions of the islands, if (due to fluctuations) some of the quantum dots are not positioned on the ideal square mesh, or even worse if the number of islands of the two layers differs. That is why often instead of the pairing probability the cross-correlation function is used, in particular in cases where only correlated or randomly distributed arrays of islands are expected. The cross-correlation function is not sensitive to fluctuations of the island positions, but also has its disadvantage: it is not capable of detecting anticorrelated growth. For an illustration of the differences of the two discussed quantities see Fig. B.1.

# Appendix C

## Numerical solution of the Green's tensor in $k$ -space

In the calculations concerned with the anisotropic strain field derived in Ch. 3 the dimensionless coefficients  $\alpha_s(\varphi)$  and  $r_s(\varphi)$  appeared, with  $\varphi$  the angle between  $\mathbf{k}_{\parallel}$  and the [100]-direction. Both play a crucial role in our calculations. In [Por77] the coefficients  $\alpha_s(\varphi)$  were introduced to give a solution of the Green's tensor, which can be numerically obtained. The latter coefficients, namely  $r_s(\varphi)$  are based on considerations in [Ipa93].

Here, the way how one obtains the above mentioned parameters is given.

At first let us define the following shorthands

$$\lambda = \sqrt{\frac{c_{11}}{c_{44}}} \quad \text{and} \quad \sigma = \frac{2c_{44} - (c_{11} - c_{12})}{c_{44}}$$

using the elastic constants  $c_{ij}$ . Then the solutions of

$$\begin{aligned} \alpha^6 - \left(3 + 2\sigma \frac{1 - \lambda^2}{\lambda^2} - \frac{\sigma^2}{\lambda^2}\right) \alpha^4 \\ + \left(3 + 2\sigma \frac{1 - \lambda^2}{\lambda^2} - \frac{\sigma^2}{\lambda^2} + \frac{\sigma}{2\lambda^2} \left(1 - \lambda^2 - 2\sigma \left(1 - 3\frac{\lambda^2}{4}\right) + \sigma^2\right) \sin(2\varphi)^2\right) \alpha^2 \\ - \left(1 + \frac{\sigma}{2\lambda^2} \left(1 - \lambda^2 - \frac{1}{2}\sigma\right) \sin(2\varphi)^2\right) \end{aligned} \quad (\text{C.1})$$

are defined as  $\alpha_s^2(\varphi)$ . Since Eq. (C.1) is a polynomial of sixth order there are six solutions in general, given by  $\pm\alpha_s^2(\varphi)$  with  $s \in 1, 2, 3$ . Let us further introduce 'shorthands', where integer indices are given modulo three, such that, e.g.,  $a_{2+2} = a_1$

$$\begin{aligned} b_j(\varphi) = -\frac{(\lambda^2 \alpha_{j+2}(\varphi)^2 - 1)(\sigma - 2 + \lambda^2 + \lambda^2 \alpha_{j+1}(\varphi)^2)}{\alpha_{j+1}(\varphi)(\sigma - 1 + \lambda^2)^2 (1 - \alpha_{j+2}(\varphi)^2 + \frac{1}{2}\sigma \sin(2\varphi)^2)} \\ + \frac{(\lambda^2 \alpha_{j+1}(\varphi)^2 - 1)(\sigma - 2 + \lambda^2 + \lambda^2 \alpha_{j+2}(\varphi)^2)}{\alpha_{j+2}(\varphi)(\sigma - 1 + \lambda^2)^2 (1 - \alpha_{j+1}(\varphi)^2 - \frac{1}{2}\sigma \sin(2\varphi)^2)} \end{aligned} \quad (\text{C.2})$$

$$s_j(\varphi) = \frac{(\lambda^2 \alpha_{j+2}(\varphi)^2 - 1)(\sigma - 2 + \lambda^2 + \lambda^2 \alpha_{j+1}(\varphi)^2)}{(\sigma - 1 + \lambda^2)^2 (1 - \alpha_{j+2}(\varphi)^2 - \frac{1}{2} \sigma \sin(2\varphi)^2)} - \frac{(\lambda^2 \alpha_{j+1}(\varphi)^2 - 1)(\sigma - 2 + \lambda^2 + \lambda^2 \alpha_{j+2}(\varphi)^2)}{(\sigma - 1 + \lambda^2)^2 (1 - \alpha_{j+1}(\varphi)^2 - \frac{1}{2} \sigma \sin(2\varphi)^2)} \quad (\text{C.3})$$

$$y_j(\varphi) = \frac{\alpha_{j+2}(\varphi) - \alpha_{j+1}(\varphi)}{\alpha_{j+2}(\varphi) \alpha_{j+1}(\varphi) (\sigma - 1 + \lambda^2)^2} \frac{(\sigma - 2 + \lambda^2 + \lambda^2 \alpha_{j+1}(\varphi)^2)}{(\sigma - 2 + \lambda^2 + \lambda^2 \alpha_{j+2}(\varphi)^2)} \quad (\text{C.4})$$

$$\tau(\varphi) = -\frac{1}{4} \sin(4\varphi) \quad (\text{C.5})$$

$$\Delta(\varphi) = \sum_{j=1}^3 \frac{\sigma - 2 + \lambda^2 + \lambda^2 \alpha_j(\varphi)^2}{\sigma - 1 + \lambda^2} b_j(\varphi) \quad (\text{C.6})$$

and finally

$$F_{jk}(\varphi) = \frac{\lambda^2 \alpha_j(\varphi)^2 - 1}{(\alpha_{k+2}(\varphi)^2 - \alpha_k(\varphi)^2)(\alpha_{k+1}(\varphi)^2 - \alpha_k(\varphi)^2) \Delta(\varphi)} \left( \alpha_k(\varphi) (1 - \lambda^2 \alpha_k(\varphi)^2) y_j(\varphi) + (s_j(\varphi) - \alpha_k(\varphi) b_j(\varphi)) \left( 1 - \alpha_k(\varphi)^2 - \frac{1}{2} \sigma \sin(2\varphi)^2 \right) (\sigma - 2 + \lambda^2 + \lambda^2 \alpha_k(\varphi)^2) \right). \quad (\text{C.7})$$

Since meanwhile the reader is convinced that the formulas are indeed lengthy, as an example we only give one component of the Green's tensor

$$\begin{aligned} \tilde{G}_{xx}(\mathbf{k}_{\parallel}; z, z') &= -\frac{1}{2\lambda^2} \sum_{j=1}^3 \frac{\exp\{-\alpha_j(\varphi)|z - z'|\}}{\alpha_j(\varphi)(\alpha_{j+2}(\varphi)^2 - \alpha_j(\varphi)^2)(\alpha_{j+1}(\varphi)^2 - \alpha_j(\varphi)^2)} \\ &\quad \left( 1 + \lambda^2 \alpha_j^2 \left( \alpha_j(\varphi)^2 - 1 - \frac{1}{\lambda^2} \right) + \frac{1}{2} \sigma (\lambda^2 \alpha_j(\varphi)^2 - 1) \sin(2\varphi)^2 \right) \\ &\quad - \frac{1}{2\lambda^2(\sigma - 1 + \lambda^2)} \sum_{j=1}^3 \left( \sum_{k=1}^3 \frac{F_{jk}(\varphi) \exp\{-\alpha_j(\varphi)z - \alpha_k(\varphi)z'\}}{\alpha_j(\varphi) \alpha_k(\varphi)} \right). \quad (\text{C.8}) \end{aligned}$$

In the last equations the remaining coefficient  $r_s$  will be shown:

$$r_s(\varphi) = \tilde{C}_s(\varphi) + \sum_{s'=1}^3 \tilde{D}_{s's}(\varphi) \quad (\text{C.9})$$

with

$$\tilde{C}_j(\varphi) = \frac{(1 - \alpha_j(\varphi)^2)^3 - \sigma \left\{ 2(1 - \alpha_j(\varphi)^2) \left( \frac{1}{4} \sin(2\varphi)^2 - \alpha_j(\varphi)^2 \right) + \frac{3}{4} \sigma \alpha_j(\varphi)^2 \sin(2\varphi)^2 \right\}}{\alpha_j(\varphi) (\alpha_j(\varphi)^2 - \alpha_{j+1}(\varphi)^2) (\alpha_j(\varphi)^2 - \alpha_{j+2}(\varphi)^2)} \quad (\text{C.10})$$

$$\tilde{D}_{jk}(\varphi) = \frac{(1 - (1 - \sigma)\alpha_j(\varphi)^2)(1 - (1 - \sigma)\alpha_k(\varphi)^2)F_{jk}(\varphi)}{(\lambda^2\alpha_j(\varphi)^2 - 1)(\lambda^2\alpha_k(\varphi)^2 - 1)(1 - \sigma - \lambda^2)\alpha_j(\varphi)\alpha_k(\varphi)}. \quad (\text{C.11})$$



# Appendix D

## Material parameters

### D.1 Fit parameters of strain field calculations

(a) Fit of Eq. (3.50a):

$$\begin{aligned} \alpha_s^{cs}(\varphi) &= A_s^\alpha + B_s^\alpha \cos 4\varphi \\ r_{1,2}^{cs}(\varphi) &= A_{1,2}^r + B_{1,2}^r \cos 4\varphi \\ \text{and } r_3^{cs} &= A_3^r + B_3^r \sin^2 4\varphi. \end{aligned}$$

<b>GaAs</b>			<b>Si</b>		
$c_{11} = 1.190, c_{12} = 0.538,$			$c_{11} = 1.6577, c_{12} = 0.6393,$		
$c_{44} = 0.595$			$c_{44} = 0.7962$		
(in units $10^{12}$ erg/cm <sup>3</sup> , [Hel75])			(in units $10^{12}$ erg/cm <sup>3</sup> , [Hel75])		
	Re	Im		Re	Im
$A_1^r$	-1.02295	-0.794448	$A_1^r$	-1.06763	-0.675733
$B_1^r$	-0.0687476	0.0444031	$B_1^r$	-0.0532454	0.0399429
$A_2^r$	-1.02295	0.794448	$A_2^r$	-1.06763	0.675733
$B_2^r$	-0.0687476	-0.0444031	$B_2^r$	-0.0532454	-0.0399429
$A_3^r$	-0.00227739		$A_3^r$	-0.00128753	
$B_3^r$	0.0715288		$B_3^r$	0.0600142	
$A_1^\alpha$	0.863938	0.542229	$A_1^\alpha$	0.899713	0.47181
$B_1^\alpha$	-0.0483097	0.0279395	$B_1^\alpha$	-0.0366019	0.0261152
$A_2^\alpha$	0.863938	-0.542229	$A_2^\alpha$	0.899713	-0.47181
$B_2^\alpha$	-0.0483097	-0.0279395	$B_2^\alpha$	-0.0366019	-0.0261152
$A_3^\alpha$	0.878689		$A_3^\alpha$	0.906383	
$B_3^\alpha$	0.130396		$B_3^\alpha$	0.100379	

<b>ZnSe</b>		
$c_{11} = 0.810, c_{12} = 0.488,$		
$c_{44} = 0.441$		
(in units $10^{12}$ erg/cm <sup>3</sup> , [Hel75])		
	Re	Im
$A_1^r$	-0.884468	-1.03673
$B_1^r$	-0.102303	0.0513749
$A_2^r$	-0.884468	1.03673
$B_2^r$	-0.102303	-0.0513749
$A_3^r$	-0.00519281	
$B_3^r$	0.0881922	
$A_1^\alpha$	0.772221	0.678001
$B_1^\alpha$	-0.0775023	0.0300962
$A_2^\alpha$	0.772221	-0.678001
$B_2^\alpha$	-0.0775023	-0.0300962
$A_3^\alpha$	0.816498	
$B_3^\alpha$	0.19902	

(b) Fit of Eq. (3.50b):

$$\alpha_s^{c8}(\varphi) = A_s^\alpha + B_s^\alpha \cos 4\varphi + C_s^\alpha \cos 8\varphi$$

$$r_s^{c8}(\varphi) = A_s^r + B_s^r \cos 4\varphi + C_s^r \cos 8\varphi$$

<b>GaAs</b>			<b>Si</b>		
$c_{11} = 1.190, c_{12} = 0.538,$			$c_{11} = 1.6577, c_{12} = 0.6393,$		
$c_{44} = 0.595$			$c_{44} = 0.7962$		
(in units $10^{12}$ erg/cm <sup>3</sup> , [Hel75])			(in units $10^{12}$ erg/cm <sup>3</sup> , [Hel75])		
	Re	Im		Re	Im
$A_1^r$	-1.02306	-0.794464	$A_1^r$	-1.06772	-0.675732
$B_1^r$	-0.068958	0.0443708	$B_1^r$	-0.0534194	0.0399457
$C_1^r$	0.0192571	0.00295655	$C_1^r$	0.0159162	-0.000252408
$A_2^r$	-1.02306	0.794464	$A_2^r$	-1.06772	0.675732
$B_2^r$	-0.068958	-0.0443708	$B_2^r$	-0.0534194	-0.0399457
$C_2^r$	0.0192571	-0.00295655	$C_2^r$	0.0159162	0.000252408
$A_3^r$	0.0334959		$A_3^r$	0.0287344	
$B_3^r$	-0.00162055		$B_3^r$	-0.00272642	
$C_3^r$	-0.0357467		$C_3^r$	-0.0299773	
$A_1^\alpha$	0.863917	0.54221	$A_1^\alpha$	0.899697	0.471798
$B_1^\alpha$	-0.0483518	0.0279011	$B_1^\alpha$	-0.0366351	0.0260898
$C_1^\alpha$	0.00385556	0.00351701	$C_1^\alpha$	0.0030364	0.00232567
$A_2^\alpha$	0.863917	-0.54221	$A_2^\alpha$	0.899697	-0.471798
$B_2^\alpha$	-0.0483518	-0.0279011	$B_2^\alpha$	-0.0366351	-0.0260898
$C_2^\alpha$	0.00385556	-0.00351701	$C_2^\alpha$	0.0030364	-0.00232567
$A_3^\alpha$	0.878738		$A_3^\alpha$	0.90642	
$B_3^\alpha$	0.130494		$B_3^\alpha$	0.100453	
$C_3^\alpha$	-0.00892244		$C_3^\alpha$	-0.00673949	

<b>ZnSe</b>		
$c_{11} = 0.810, c_{12} = 0.488,$		
$c_{44} = 0.441$		
(in units $10^{12}$ erg/cm <sup>3</sup> , [Hel75])		
	Re	Im
$A_1^r$	-0.884599	-1.0368
$B_1^r$	-0.102565	0.0512471
$C_1^r$	0.0239207	0.0116994
$A_2^r$	-0.884599	1.0368
$B_2^r$	-0.102565	-0.0512471
$C_2^r$	0.0239207	-0.0116994
$A_3^r$	0.0388848	
$B_3^r$	0.00338438	
$C_3^r$	-0.0441331	
$A_1^\alpha$	0.772189	0.677965
$B_1^\alpha$	-0.0775657	0.0300241
$C_1^\alpha$	0.00580473	0.00659529
$A_2^\alpha$	0.772189	-0.677965
$B_2^\alpha$	-0.0775657	-0.0300241
$C_2^\alpha$	0.00580473	-0.00659529
$A_3^\alpha$	0.81658	
$B_3^\alpha$	0.199185	
$C_3^\alpha$	-0.0150859	

(c) Fit of Eq. (3.50c):

$$\alpha_s^{c4}(\varphi) = A_s^\alpha + B_s^\alpha \cos 4\varphi$$

$$r_s^{c4}(\varphi) = A_s^r + B_s^r \cos 4\varphi$$

<b>GaAs</b>			<b>Si</b>		
$c_{11} = 1.190, c_{12} = 0.538,$			$c_{11} = 1.6577, c_{12} = 0.6393,$		
$c_{44} = 0.595$			$c_{44} = 0.7962$		
(in units $10^{12}$ erg/cm <sup>3</sup> , [Hel75])			(in units $10^{12}$ erg/cm <sup>3</sup> , [Hel75])		
	Re	Im		Re	Im
$A_1^r$	-1.02295	-0.794448	$A_1^r$	-1.06763	-0.675733
$B_1^r$	-0.0687476	0.0444031	$B_1^r$	-0.0532454	0.0399429
$A_2^r$	-1.02295	0.794448	$A_2^r$	-1.06763	0.675733
$B_2^r$	-0.0687476	-0.0444031	$B_2^r$	-0.0532454	-0.0399429
$A_3^r$	0.0333005		$A_3^r$	0.0285706	
$B_3^r$	-0.00201122		$B_3^r$	-0.00305404	
$A_1^\alpha$	0.863938	0.542229	$A_1^\alpha$	0.899713	0.47181
$B_1^\alpha$	-0.0483097	0.0279395	$B_1^\alpha$	-0.0366019	0.0261152
$A_2^\alpha$	0.863938	-0.542229	$A_2^\alpha$	0.899713	-0.47181
$B_2^\alpha$	-0.0483097	-0.0279395	$B_2^\alpha$	-0.0366019	-0.0261152
$A_3^\alpha$	0.878689		$A_3^\alpha$	0.906383	
$B_3^\alpha$	0.130396		$B_3^\alpha$	0.100379	

<b>ZnSe</b>		
$c_{11} = 0.810, c_{12} = 0.488,$		
$c_{44} = 0.441$		
(in units $10^{12}$ erg/cm <sup>3</sup> , [Hel75])		
	<b>Re</b>	<b>Im</b>
$A_1^r$	-0.884468	-1.03673
$B_1^r$	-0.102303	0.0513749
$A_2^r$	-0.884468	1.03673
$B_2^r$	-0.102303	-0.0513749
$A_3^r$	0.0386437	
$B_3^r$	0.00290205	
$A_1^\alpha$	0.772221	0.678001
$B_1^\alpha$	-0.0775023	0.0300962
$A_2^\alpha$	0.772221	-0.678001
$B_2^\alpha$	-0.0775023	-0.0300962
$A_3^\alpha$	0.816498	
$B_3^\alpha$	0.19902	

## D.2 Elastic parameters and lattice constants of selected materials

Here, a short table of selected semiconductor materials and some of their properties is given. Listed are the lattice constant  $a$ , the elastic constants  $c_{ij}$  and the anisotropy ratio  $A = 2c_{44}/(c_{11} - c_{12})$ . The values are taken from [Lid97; Hel75].

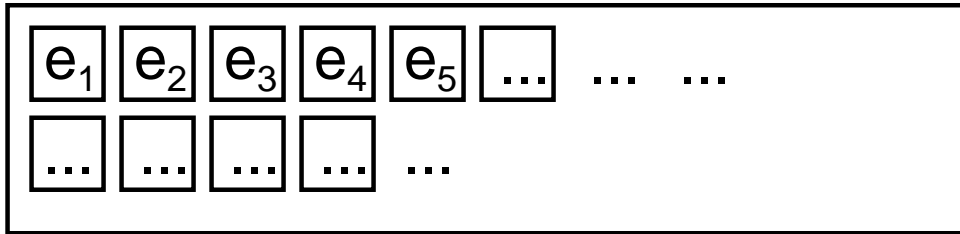
material	$a$ [nm]	$c_{11}$ [ $10^{11}$ erg/cm $^3$ ]	$c_{12}$ [ $10^{11}$ erg/cm $^3$ ]	$c_{44}$ [ $10^{11}$ erg/cm $^3$ ]	$A$
Si	0.5431	16.58	6.39	7.96	1.56
Ge	0.5658	12.85	4.83	6.68	1.66
AlP	0.5451	13.20	6.30	6.15	1.78
AlAs	0.5661	12.50	5.34	5.42	1.51
AlSb	0.6136	8.77	4.34	4.08	1.84
GaP	0.5451	14.12	6.25	7.05	1.79
GaAs	0.5653	11.81	5.32	5.94	1.83
GaSb	0.6095	8.84	4.03	4.32	1.79
InP	0.5869	10.22	5.76	4.60	2.06
InAs	0.6058	8.33	4.53	3.96	2.08
InSb	0.6479	6.58	3.57	2.98	1.98
ZnS	0.5420	10.32	6.46	4.62	2.39
ZnSe	0.5668	8.10	4.88	4.41	2.74
ZnTe	0.6103	7.13	4.07	3.12	2.04
CdTe	0.6480	5.35	3.68	1.99	2.39



# Appendix E

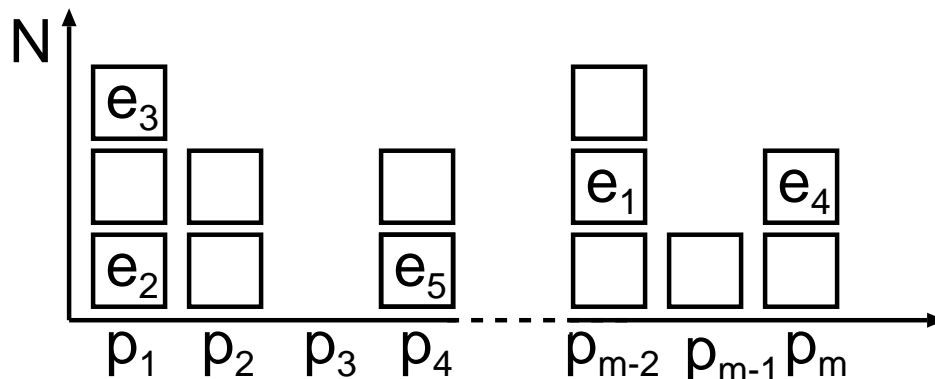
## Event selection in the kinetic Monte Carlo routine

To ensure high computational efficiency of the kinetic Monte Carlo routine (Sec. 2.4, p. 21) an appropriate algorithm for the selection of events, i.e., adatom movements, is necessary. In short this was discussed in Sec. 2.4.2. Here, a more illustrative sketch will be given. Consider a sample set with processes  $e_i$  each having certain probability according to the Arrhenius term (Eq. (2.19), p. 21).

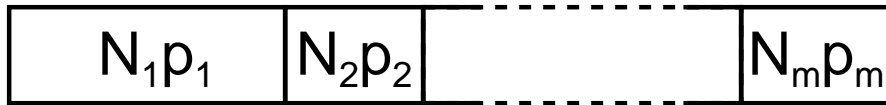


Then the algorithm is as follows:

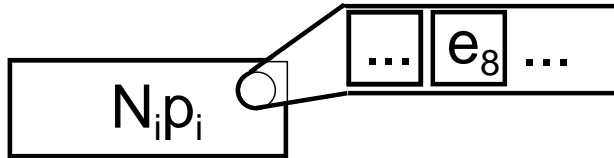
- (1) The sample set is sorted according to the probabilities  $p_j$ . Note that the differences of subsequent 'probability intervals'  $\Delta_{j,(j-1)} = p_j - p_{j-1}$  and  $\Delta_{(j+1),j} = p_{j+1} - p_j$  not necessarily have to be equal, i.e.,  $\Delta_{j,(j-1)} \neq \Delta_{(j+1),j}$ . In most approaches equally spaced intervals are chosen, in our kinetic Monte Carlo routine we have varied the value of  $\Delta_{j,(j-1)}$  as explained in detail in Sec. 2.4.2.



(2) classes are formed from the sorted sample set, which build up a probability-vector



(3) randomly one class is selected,



(4) randomly again one event from this class is selected, and is executed.



# List of Figures

1	Illustration of a nanocar. . . . .	xi
2	A gear chain with a mite approaching. . . . .	xii
1.1	Three-dimensional scanning tunneling microscopy (STM) image of an uncovered InAs QD grown on GaAs(001). [Már01] . . . . .	2
1.2	Scanning tunneling microscopy topograph of an Ge island during Si capping. [Ras01] . . . . .	2
1.3	Plan-view transmission electron microscopy image of InAs/GaAs quantum dots. [Bim96] . . . . .	3
1.4	Cross-sectional transmission electron microscopy images of (In,Ga)As/GaAs quantum dot stack. [Ma04] . . . . .	4
1.5	Overview cross-sectional scanning-tunneling microscopy image of a InAs/GaAs dot-stack layer and the surrounding buffer layers. [Fle99] . . . . .	4
2.1	Adatom-probability-KMC method. Surface before and after a collapse of the adatom density. [Man03] . . . . .	17
2.2	Island size distribution as obtained by KMC, AP-KMC and AD-KMC. [Man03] . . . . .	19
2.3	Comparison of the island shape in KMC and AD-KMC [Man03] . . . . .	20
2.4	Illustration of the binding energies in the kinetic Monte Carlo (KMC) simulation. . . . .	22
2.5	Illustration of the effect of strain on the equilibrium distance. . . . .	23
2.6	Illustration of the solid-on-solid model. . . . .	24
2.7	Illustration of the Schwöbel barrier. . . . .	24
2.8	Adaptive energy intervals. . . . .	26
2.9	Sketch of the growth method for simulating quantum dot stacks. . . . .	28
2.10	Simulations with an additional energy barrier. . . . .	29
3.1	Schematic illustration to the energy of elastic inclusions . . . . .	34
3.2	Illustration of the energy terms used in our calculations. . . . .	39
3.3	Illustration of the notation used. . . . .	40
3.4	Ratio between fit and exact numerical results. . . . .	44
3.5	Comparison of numerical and analytical results of the elastic energy density. . . . .	47
3.6	Elastic energy density as function of the spherical angle $\Theta$ . . . . .	47
3.7	Comparison of the strain tensor computed with the method developed in this work and an atomistic approach. . . . .	49
4.1	Elastic energy of a monolayer height island. . . . .	56

4.2	Illustration of the notation used. . . . .	57
4.3	Normalized elastic energy distribution on the surface of one quantum dot [Hol99]	57
4.4	Elastic energy distribution of a buried dot. . . . .	58
4.5	Elastic energy in the growth surface of various sample structures . . . . .	61
4.6	Elastic energy of a pyramid beneath the surface with respect to the orientation of its base. . . . .	62
4.7	Elastic energy of a buried platelet and a point defect. . . . .	63
4.8	Schematic illustration of the density plots in Fig. 4.9, Fig. 4.10. . . . .	64
4.9	Elastic energy of a single point-like quantum dot. . . . .	65
4.10	Elastic energy of a periodic array of point-like quantum dots. . . . .	66
4.11	Elastic energy of an array of point-like quantum dots with an additional array situated in the buffer layer. . . . .	67
4.12	Elastic energy of an array of point-like quantum dots for different parent materials. . . . .	67
4.13	Cross-sectional atomic force microscopy images of $\text{In}_{0.5}\text{Ga}_{0.5}\text{As}$ QD stacks. [Wan04] . . . . .	68
4.14	Cross-sectional scanning tunneling microscopy images of $\text{In}_{0.5}\text{Ga}_{0.5}\text{As}$ QDs. [Wan04] . . . . .	69
4.15	Elastic energy of an array of quantum dots of various shapes. . . . .	70
4.16	Elastic energy of stripe shaped islands. . . . .	72
4.17	Elastic energy of stripe shaped islands for different materials. . . . .	73
4.18	The interaction energy of a sheet of surface islands and a sheet of buried islands. Both sheets consist of identical one-dimensional arrays of infinitely elongated stripes. [Shc98b] . . . . .	73
5.1	Ostwald ripening vs. cooperative growth. . . . .	77
5.2	Results of the KMC simulation of quantum dot arrays. . . . .	80
5.3	Optimized spatial ordering [Mei03a]. . . . .	81
5.4	Number of atoms in the first monolayer vs. coverage. . . . .	82
5.5	Temporal evolution of island size distributions. . . . .	83
6.1	Transmission electron microscope (TEM) image of an $\text{InAs}/\text{GaAs}$ quantum dot stack [Xie95]. . . . .	85
6.2	Cross-sectional scanning tunneling microscopy (STM) images of the $\text{In}_{0.5}\text{Ga}_{0.5}\text{As}$ QDs. (a) A column of correlated QDs and (b) an array of anticorrelated QDs [Wan04]. . . . .	86
6.3	Sample structures used for the growth simulations of QD stacks on prepatterned substrate. . . . .	87
6.4	Cross-correlation coefficient of simulated quantum dot stacks using a prepatterned substrate. Influence of the strength of the strain field. . . . .	89
6.5	Cross-correlation coefficient of a quantum dot stack in dependence of the spacer layer thickness and the coverage. A prepatterned first layer was used. . . . .	90
6.6	Simulations of quantum dot stacks in the anticorrelated growth mode. . . . .	92
6.7	Simulations of quantum dot stacks in the anticorrelated growth mode. Cut along the plane spanned by the growth direction and the [110]-direction. . . . .	93
6.8	Spacer layer thickness vs. pairing probability on prepatterned substrate . . . . .	93

---

6.9	Spacer layer thickness $d_{\text{anti}}$ for anticorrelated growth of an optimal laterally arranged array of QDs in dependence of their density. Material parameters of GaAs were used. See Eq. (6.4). . . . .	94
6.10	Critical coverage. Percentage of atoms in the first layer in dependence of the spacer layer thickness of a quantum dot stack. . . . .	96
6.11	Cross-correlation coefficient of stacked QD structures. . . . .	97
6.12	An example of a simulated vertically correlated QD stack. . . . .	98
6.13	Simulation of vertical aligned QD stacks. Cut along the [100]-direction. . . . .	99
6.14	Cross-correlation coefficient of 20-layer QD stacks. . . . .	99
6.15	Scanning tunneling microscopy image of a threefold InAs/GaAs QD stack grown by MOCVD. [Fle99] . . . . .	100
6.16	Cross-sectional scanning tunneling microscopy image of InAs/GaAs QD stacks grown by MBE. [Lit99] . . . . .	100
B.1	Pairing probability and cross-correlation coefficient—the sketch illustrates the differences of the two quantities. . . . .	111



# Bibliography

- [Abs96] G. Abstreiter, P. Schittenhelm, C. Engel, E. Silveria, A. Zrenner, D. Meertens, and W. Jäger: *Growth and characterization of self-assembled Ge-rich islands on Si*. *Semicond. Sci. Technol.* **11**, 1521 (1996).
- [Ala02] T. Ala-Nissika, R. Ferrandos, and S. C. Ying: *Collective and single particle diffusion on surfaces*. *Adv. in Phys.* **51**, 949 (2002).
- [Ama95] J. G. Amar and F. Family: *Critical Cluster Size: Island Morphology and Size Distribution in Submonolayer Epitaxial Growth*. *Phys. Rev. Lett.* **74**, 2066 (1995).
- [Ama02] J. Amar, F. Family, and M. N. Popescu: *Kinetics of submonolayer epitaxial growth*. *Comp. Phys. Comm.* **146**, 1 (2002).
- [Bar95] A.-L. Barabási and H. E. Stanley: *Fractal concepts in surface growth* (Cambridge University Press, Cambridge, U.K., 1995).
- [Bel00] G. R. Bell, T. J. Krzyzewski, P. B. Joyce, and T. S. Jones: *Island size scaling for submonolayer growth of InAs on GaAs(001)-(2 × 4): Strain and surface reconstruction effects*. *Phys. Rev. B* **61**, R10551 (2000).
- [Ben96] B. R. Bennett, R. Magno, and B. V. Shanabrook: *Molecular beam epitaxial growth of InSb, GaSb and AlSb nanometer-scale dots on GaAs*. *Appl. Phys. Lett.* **68**, 505 (1996).
- [Bim96] D. Bimberg, N. N. Ledentsov, M. Grundmann, N. Kirstaedter, O. G. Schmidt, M. H. Mao, V. Ustinov, A. Egorov, A. Zhukov, P. Kop'ev, Z. Alferov, S. Ruvimov, U. Gösele, and J. Heydenreich: *InAs-GaAs quantum pyramid lasers: in situ growth, radiative lifetimes and polarization properties*. *Jpn. J. Appl. Phys.* **35**, 1311 (1996).
- [Bim99] D. Bimberg, M. Grundmann, and N. Ledentsov: *Quantum Dot Heterostructures* (John Wiley & Sons Ltd., New York, 1999).
- [Bin79] K. Binder: *Monte Carlo Methods in Statistical Physics* (Springer Verlag, Berlin, Heidelberg, New York, 1979).
- [Blo04] M. Block, R. Kunert, E. Schöll, T. Boeck, and T. Teubner: *Kinetic Monte Carlo simulation of formation of microstructures in liquid droplets*. *New J. Phys.* **6**, 166 (2004).

- [Boi98] G. Boisvert, N. Mousseau, and L. J. Lewis: *Surface diffusion coefficients by thermodynamic integration: Cu on Cu(100)*. Phys. Rev. B **58**, 12667 (1998).
- [Bor75] A. B. Bortz, M. H. Kalos, and J. L. Lebowitz: *A new algorithm for Monte Carlo simulations of Ising spin systems*. J. Comp. Phys. **17**, 10 (1975).
- [Bos99a] S. Bose and E. Schöll: *Kinetic Monte Carlo Simulation of the Nucleation of Self-Assembled Quantum Dots*. In *Proc. 24th International Conference on The Physics of Semiconductors (ICPS-24), Jerusalem, Israel*, edited by D. Gershoni (World Scientific, Singapore, 1999).
- [Bos99b] S. Bose and E. Schöll: *Optimization of the size distribution of self-organized quantum dots*. In *Proceedings of the 7<sup>th</sup> International Symposium on Nanostructure: Physics and Technology*, pp. 506–509 (Ioffe Institut, St. Petersburg, 1999).
- [Bos00] S. Bose: *Pattern formation at semiconductor interfaces and surfaces*. Ph.D. thesis, Technische Universität Berlin (2000).
- [Bru95] H. Brune, K. Bromann, H. Röder, K. Kern, J. Jacobsen, P. Stoltze, K. Jacobsen, and J. Nørskov: *Effect of strain on surface diffusion and nucleation*. Phys. Rev. B **52**, R14380 (1995).
- [Cao03] Y. G. Cao, M. H. Xie, Y. Liu, S. H. Xu, Y. F. Ng, H. S. Wu, and S. Y. Tong: *Scaling of three-dimensional InN islands grown on GaN(0001) by molecular-beam epitaxy*. Phys. Rev. B **68**, 161304 (2003).
- [Che04] V. Cherepanov, S. Filimonov, J. Myslivecek, and B. Voigtlander: *Scaling of submonolayer island sizes in surfactant-mediated epitaxy of semiconductors*. Phys. Rev. B **70**, 085401 (2004).
- [Chi90] T. H. Chiu and S. N. G. Chu: *Is the cation sticking coefficient unity in molecular beam epitaxy at low temperature?* Appl. Phys. Lett. **57**, 1425 (1990).
- [Cul02] A. G. Cullis, D. J. Norris, T. Walther, M. A. Migliorato, , and M. Hopkinson: *Stranski-Krastanow transition and epitaxial island growth*. Phys. Rev. B **66**, 081305 (2002).
- [Dun01] A. Dunbar, M. Halsall, P. Dawson, U. Bangert, M. Miura, and Y. Shiraki: *The effect of strain field seeding on the epitaxial growth of Ge islands on Si(001)*. Appl. Phys. Lett. **78**, 1658 (2001).
- [Dya02] M. I. Dyakonov: *Quantum computing: a view from the enemy camp*. In *Future Trends in Microelectronics. The nano Millenium*, edited by S. Luryi, J. Xu, and A. Zaslavsky, p. 307 (Wiley, New York, 2002). [Http://arxiv.org/abs/cond-mat/0110326](http://arxiv.org/abs/cond-mat/0110326).
- [Eag90] D. J. Eaglesham and M. Cerullo: *Dislocation-Free Stranski-Krastanow Growth of Ge on Si(100)*. Phys. Rev. Lett. **64**, 1943 (1990).

- [Edw82] S. F. Edwards and D. R. Wilkinson: *The Surface Statistics of a Granular Aggregate*. Proc. Roy. Soc. London, Ser. A **381**, 17 (1982).
- [Ehr66] G. Ehrlich and F. G. Hudda: *Atomic View of Surface Self-Diffusion: Tungsten on Tungsten*. J. Chem. Phys. **44**, 1039 (1966).
- [Eig90] D. M. Eigler and E. K. Schweizer: *Positioning single atoms with a scanning tunnelling microscope*. Nature **344**, 524 (1990).
- [Els03] F. Elsholz, M. Meixner, and E. Schöll: *Kinetic Monte Carlo simulation of self-organized pattern formation in thin film deposition*. Nucl. Instruments and Methods B **202C**, 249 (2003).
- [Els04] F. Elsholz, E. Schöll, and A. Rosenfeld: *Control of surface roughness in amorphous thin film growth*. Appl. Phys. Lett. **84**, 4167 (2004).
- [Els05a] F. Elsholz: *Kinetic Monte Carlo Simulations of Thin Film Growth*. Ph.D. thesis, TU Berlin (2005).
- [Els05b] F. Elsholz, E. Schöll, C. Scharfenorth, G. Seewald, H. J. Eichler, and A. Rosenfeld: *Roughness evolution in thin film growth of  $\text{SiO}_2$  and  $\text{Nb}_2\text{O}_5$* . J. Appl. Phys. **98**, 103516 (2005).
- [Esa74] L. Esaki and L. L. Chang: *New Transport Phenomenon in a Semiconductor Superlattice*. Phys. Rev. Lett. **33**, 495 (1974).
- [Eva90] J. W. Evans, D. E. Sanders, P. A. Thiel, and A. E. DePristo: *Low-temperature epitaxial growth of thin metal films*. Phys. Rev. B **41**, 5410 (1990).
- [Eva01] J. W. Evans and M. C. Bartelt: *Nucleation, adatom capture, and island size distributions: Unified scaling analysis for submonolayer deposition*. Phys. Rev. B **63**, 235408 (2001).
- [Eva02] J. W. Evans and M. C. Bartelt: *Island sizes and capture zone areas in submonolayer deposition: Scaling and factorization of the joint probability distribution*. Phys. Rev. B **66**, 235410 (2002).
- [Fel03] M. Felten: *Kinetische Monte-Carlo-Simulation von SiGe-Inselketten bei der Flüssigphasenepitaxie*. Master's thesis, TU Berlin (2003).
- [Fic91] K. Fichthorn and W. Weinberg: *Theoretical foundations of dynamical Monte Carlo simulations*. J. Chem. Phys. **95**, 1090 (1991).
- [Fla96] F. Flack, N. Samarth, V. Nikitin, P. A. Crowell, J. Shi, J. Levy, and D. D. Awschalom: *Near-field optical spectroscopy of localized excitons in strained CdSe quantum dots*. Phys. Rev. B **54**, R17312 (1996).

- [Fle99] O. Flebbe, H. Eisele, T. Kalka, F. Heinrichsdorff, A. Krost, D. Bimberg, , and M. Dähne-Prietsch: *Atomic structure of stacked InAs quantum dots grown by metal-organic chemical-vapor depostion*. Journal of Vacuum Science and Technology B **17**, 1639 (1999).
- [Fra49] F. C. Frank and J. H. van der Merwe: *One-dimensional dislocations. I. Static theory*. Proc. R. Soc. London, Ser. A **198**, 205 (1949).
- [Fra03] S. Franchi, G. Trevisi, L. Seravalli, and P. Frigeri: *Quantum dot nanostructures and molecular beam epitaxy*. Progress in Crystal Growth and Characterization of Materials **47**, 166 (2003).
- [Fre05] R. A. Freitas, Jr.: *Nanotechnology, nanomedicine and nanosurgery*. Int. J. Surg. **3**, 243 (2005).
- [Fro05] P. Fromherz: *The Neuron-Semiconductor Interface*. In *Bioelectronics - from Theory to Applications*, edited by I. Willner and E.Katz, pp. 339–394 (Wiley-VCH, Weinheim, 2005).
- [Gol85] L. Goldstein, F. Glas, J. Y. Marzin, M. N. Charasse, and G. L. Roux: *Growth by molecular beam epitaxy and charakterization of InAs/GaAs strained-layer superlattices*. Appl. Phys. Lett. **47**, 1099 (1985).
- [Gon98] A. R. Goni, M. Stroh, C. Thomsen, F. Heinrichsdorff, V. Turck, A. Krost, and D. Bimberg: *High-gain excitonic lasing from a single InAs monolayer in bulk GaAs*. Appl. Phys. Lett. **72**, 1433 (1998).
- [Gon01] J. C. Gonzalez, R. Magalhaes-Paniago, W. N. Rodrigues, A. Malachias, M. V. B. Moreira, A. G. de Oliveira, I. Mazzaro, C. Cusatis, T. H. Metzger, and J. Peisl: *X-ray determination of vertical ordering of InAs quantum dots in InAs/GaAs multilayers*. Appl. Phys. Lett. **78**, 1056 (2001).
- [Gro02] F. Grosse and M. F. Gyure: *Ab initio based modeling of III-V semiconductor surfaces: Thermodynamic equilibrium and growth kinetics on atomic scales*. Phys. Rev. B **66**, 075320 (2002).
- [Gyu98] M. F. Gyure, J. J. Zinck, C. Ratsch, and D. D. Vvedensky: *Unstable Growth on Rough Surfaces*. Phys. Rev. Lett. **81**, 4931 (1998).
- [Ham06] T. Hammerschmidt, P. Kratzer, and M. Scheffler: *Analytic Many-Body Potential for the Investigation of InAs/GaAs Surfaces and Nanostructures* (2006). In preparation.
- [Hän90] P. Hänggi, P. Talkner, and M. Borkovec: *Reaction-rate theory: fifty years after Kramers*. Rev. Mod. Phys. **62**, 251 (1990).
- [Han04] M. Hanke, M. Schmidbauer, D. Grigoriev, H. Raidt, P. Schafer, R. Kohler, A.-K. Gerlitzke, and H. Wawra: *SiGe/Si(001) Stranski-Krastanow islands by liquid-phase epitaxy: Diffuse x-ray scattering versus growth observations*. Phys. Rev. B **69**, 075317 (2004).

- [Hei97a] F. Heinrichsdorff, M.-H. Mao, N. Kirstaedter, A. Krost, D. Bimberg, A. O. Kosogov, and P. Werner: *Room-temperature continuous-wave lasing from stacked InAs/GaAs quantum dots grown by metalorganic chemical vapor deposition*. Appl. Phys. Lett. **71**, 22 (1997).
- [Hei97b] R. Heitz, T. R. Ramachandran, A. Kalburge, Q. Xie, I. Mukhametzhanov, P. Chen, and A. Madhukar: *Observation of Reentrant 2D to 3D Morphology Transition in Highly Strained Epitaxy: InAs on GaAs*. Phys. Rev. Lett. **78**, 4071 (1997).
- [Hel75] K. Hellwege and O. Madelung, eds.: *Landolt-Börnstein: Numerical Data and Functional Relationships in Science and Technology – New Series*, vol. III/7B1/II.1.1 (Springer, Berlin, Heidelberg, New York, 1975).
- [Hen03] G. Henkelman and H. Jónsson: *Multiple Time Scale Simulations of Metal Crystal Growth Reveal the Importance of Multiatom Surface Processes*. Phys. Rev. Lett. **90**, 116101 (2003).
- [Her04] M. Herman, W. Richter, and H. Sitter: *Epitaxy – Physical Foundation and Technical Implementation* (Springer-Verlag, Berlin, New York, 2004).
- [Hey01] C. Heyn: *Anisotropic island growth during submonolayer epitaxy*. Phys. Rev. B **63**, 033403 (2001).
- [Hey02] C. Heyn: *Stability of InAs quantum dots*. Phys. Rev. B **66**, 075307 (2002).
- [Hol99] V. Holý, G. Springholz, M. Pinczolit, and G. Bauer: *Strain induced vertical and lateral correlations in quantum dot superlattices*. Phys. Rev. Lett. **83**, 356 (1999).
- [Ipa93] I. P. Ipatova, V. G. Malyshkin, and V. A. Shchukin: *On spinodal decomposition in elastically anisotropic epitaxial films of III-V semiconductor alloys*. J. Appl. Phys. **74**, 7198 (1993).
- [Ipa98] I. P. Ipatova, V. G. Malyshkin, A. A. Maradudin, V. A. Shchukin, and R. F. Wallis: *Kinetic instability of semiconductor alloy growth*. Phys. Rev. B **57**, 12968 (1998).
- [Jes93] D. E. Jesson, S. J. Pennycook, J.-M. Baribeau, and D. C. Houghton: *Direct imaging of surface cusp evolution during strained-layer epitaxy and implications for strain relaxation*. Phys. Rev. Lett. **71**, 1744 (1993).
- [Joy99] B. A. Joyce, D. D. Vvedensky, G. R. Bell, J. G. Belk, M. Itoh, and T. S. Jones: *Nucleation and growth mechanisms during MBE of III-V compounds*. Mater. Sci. Eng. B **67**, 7 (1999).
- [Kam96] A. Y. Kaminskii and R. A. Suris: *Smoothing of crystal surfaces during growth interruption*. Appl. Surf. Sci. **104/105**, 312 (1996).
- [Kam03] N. G. van Kampen: *Stochastic Processes in Physics and Chemistry* (North-Holland, Amsterdam, 2003).

- [Kar86] M. Kardar, G. Parisi, and Y.-C. Zhang: *Dynamic scaling of growing interfaces*. Phys. Rev. Lett. **56**, 889 (1986).
- [Kar04] G. S. Kar, S. Kiravittaya, M. Stoffel, and O. G. Schmidt: *Material Distribution across the Interface of Random and Ordered Island Arrays*. Phys. Rev. Lett. **93**, 246103 (2004).
- [Kha83] A. G. Khachaturyan: *Theory of Structural Transformations in Solids* (Wiley, New York, 1983).
- [Kie99] O. Kienzle, F. Ernst, M. Ruhle, O. G. Schmidt, and K. Eberl: *Germanium “quantum dots” embedded in silicon: Quantitative study of self-alignment and coarsening*. Appl. Phys. Lett. **74**, 269 (1999).
- [Kle94] A. Kley and J. Neugebauer: *Atomic and electronic structure of the GaAs/ZnSe(001) interface*. Phys. Rev. B **50**, 8616 (1994).
- [Kle97] A. Kley, P. Ruggerone, and M. Scheffler: *Novel diffusion mechanism on the GaAs(001) surface: the role of adatom-dimer interaction*. Phys. Rev. Lett. **79**, 5278 (1997).
- [Kli90] K. von Klitzing: *Ten Years Quantum Hall Effect*. Festkörperprobleme - Advances in Solid State Physics **30**, 25 (1990).
- [Koh99] W. Kohn: *Nobel Lecture: Electronic structure of matter—wave functions and density functionals*. Rev. Mod. Phys. **71**, 1253 (1999).
- [Kov02] A. R. Kovsh, A. E. Zhukov, N. A. Maleev, S. S. Mikhrin, A. V. Vasil’ev, Y. M. Shernyakov, D. A. Livshits, M. V. Maximov, D. S. Sizov, N. V. Kryzhanovskaya, N. A. Pikhtin, V. A. Kapitonov, I. S. Tarasov, N. N. Ledentsov, V. M. Ustinov, J. S. Wang, L. Wei, G. Lin, and J. Y. Chi: *High power lasers based on submonolayer InAs-GaAs quantum dots and InGaAs quantum wells*. In *Proc. 10th International Symposium on Nanostructures: Physic and Technology* (Ioffe Institut, St. Petersburg, 2002).
- [Kra98] P. Kratzer, C. G. Morgan, and M. Scheffler: *Density functional theory studies on microscopic processes of GaAs growth*. Progr. Surf. Sci. **59**, 135 (1998).
- [Kra99] P. Kratzer, C. G. Morgan, and M. Scheffler: *Model for nucleation in GaAs homoepitaxy derived from first principles*. Phys. Rev. B **59**, 2790 (1999).
- [Kra02a] P. Kratzer, E. Penev, and M. Scheffler: *First-principles studies of kinetics in epitaxial growth of III-V semiconductors*. Appl. Phys. A **75**, 79 (2002).
- [Kra02b] P. Kratzer and M. Scheffler: *Reaction-Limited Island Nucleation in Molecular Beam Epitaxy of Compound Semiconductors*. Phys. Rev. Lett. **88**, 036102 (2002).
- [Kra05] B. Krause, T. H. Metzger, A. Rastelli, R. Songmuang, S. Kiravittaya, and O. G. Schmidt: *Shape, strain, and ordering of lateral InAs quantum dot molecules*. Phys. Rev. B **72**, 085339 (2005).

- [Kru93] J. Krug, M. Plischke, and M. Siegert: *Surface Diffusion Currents and the Universality Classes of Growth*. Phys. Rev. Lett. **70**, 3271 (1993).
- [Kru00] J. Krug, P. Politi, and T. Michely: *Island nucleation in the presence of step-edge barriers: Theory and applications*. Phys. Rev. B **61**, 14037 (2000).
- [Kru03] J. Krug: *Four Lectures on the Physics of Crystal Growth*. Physica A **313**, 47 (2003).
- [Krz02] T. J. Krzyzewski, P. B. Joyce, G. R. Bell, and T. S. Jones: *Scaling behavior in InAs/GaAs(001) quantum-dot formation*. Phys. Rev. B **66**, 201302 (2002).
- [Kun90] R. Kunkel, B. Poelsema, L. K. Verheij, and G. Comsa: *Reentrant Layer-by-Layer Growth during Molecular-Beam Epitaxy of Metal-on-Metal Substrates*. Phys. Rev. Lett. **65**, 733 (1990).
- [Kun00] R. Kunert: *Monte-Carlo-Simulation der Wachstumskinetik von Quantenpunkten im Nukleationsstadium*. Master's thesis, TU Berlin (2000).
- [Kun06] R. Kunert, E. Schöll, T. Hammerschmidt, and P. Kratzer: *Strain field calculations of quantum dots — a comparison study of two methods*. In *Proc. 28th International Conference on the Physics of Semiconductors (ICPS-28), Vienna 2006*, edited by W. Jantsch and F. Schaffler (Springer, Berlin, 2006). (in preparation).
- [Kur95] A. Kurtenbach, K. Eberl, and T. Shitara: *Nanoscale InP island embedded in InGaP*. Appl. Phys. Lett. **66**, 361 (1995).
- [Lan70] L. D. Landau and E. M. Lifshitz: *Theory of elasticity* (Pergamon, New York, 1970).
- [Lar04] M. I. Larsson, K. Cho, and B. M. Clemens: *Surface diffusion mechanisms for strain-induced self-assembly*. Phys. Rev. B **69**, 155426 (2004).
- [Led95] N. N. Ledentsov, M. Grundmann, N. Kirstaedter, J. Christen, R. Heitz, J. Böhrer, F. Heinrichsdorff, D. Bimberg, S. S. Ruvimov, P. Werner, U. Richter, U. Gösele, J. Heydenreich, V. M. Ustinov, A. Y. Egorov, M. V. Maximov, P. S. Kop'ev, and Z. I. Alferov: *Luminescence and Structural Properties of (In,Ga)As/GaAs Quantum Dots*. In *Proc. 22nd Int. Conf. Phys. Semicond., (ICPS-22), (Vancouver, Canada, 1994)*, edited by D. J. Lockwood (World Scientific, Singapore, 1995).
- [Led96] N. N. Ledentsov, M. Grundmann, N. Kirstaedter, O. Schmidt, R. Heitz, J. Böhrer, D. Bimberg, V. Ustinov, V. Shchukin, A. Egorov, A. Zhukov, S. Zaitsev, Z. A. P.S. Kop'ev, S. Ruvimov, P. Werner, U. Gösele, and J. Heydenreich: *Ordered Arrays of Quantum Dots: Formation, Electronic Spectra, Relaxing Phenomena, Lasing*. Sol. State El. **40**, 785 (1996).
- [Lee00] H. Lee, J. A. Johnson, J. S. Speck, and P. M. Petroff: *Controlled ordering and positioning of InAs self-assembled quantum dots*. J. Vac. Sci. Technol. B **18**, 2193 (2000).

- [Lee01] H. Lee, J. A. Johnson, M. Y. He, J. S. Speck, and P. M. Petroff: *Strain-engineered self-assembled semiconductor quantum dot lattices*. Appl. Phys. Lett. **78**, 105 (2001).
- [Lid97] D. R. Lide, ed.: *Handbook of chemistry and physics* (CRC Press LLC, 1997).
- [Lit99] B. Lita, R. S. Goldman, J. D. Phillips, and P. K. Bhattacharya: *Nanometer-scale studies of vertical organization and evolution of stacked self-assembled InAs/GaAs quantum dots*. Appl. Phys. Lett. **74**, 2824 (1999).
- [Liu99] F. Liu, S. E. Davenport, H. M. Evans, and M. G. Lagally: *Self-Organized Replication of 3D Coherent Island Size and Shape in Multilayer Heteroepitaxial Films*. Phys. Rev. Lett. **82**, 2528 (1999).
- [Liu01] B.-G. Liu and E. Schöll: *Strained growth in surfactant mediated heteroepitaxy*. Vacuum **61**, 145 (2001).
- [Ma04] W. Q. Ma, M. L. Hussein, J. L. Shultz, G. J. Salamo, T. D. Mishima, and M. B. Johnson: *Enhancing the in-plane spatial ordering of quantum dots*. Phys. Rev. B **69**, 233312 (2004).
- [Mad83] A. Madhukar: *Far from equilibrium vapour phase growth of lattice matched III-IV compound semiconductor interfaces: Some basic concepts and Monte Carlo computer simulations*. Surf. Sci. **132**, 344 (1983).
- [Man03] L. Mandreoli, J. Neugebauer, R. Kunert, and E. Schöll: *Adatom Density kinetic Monte Carlo: A hybrid approach to perform epitaxial growth simulations*. Phys. Rev. B **68**, 155429 (2003).
- [Már01] J. Márquez, L. Geelhaar, and K. Jacobi: *Atomically resolved structure of InAs quantum dots*. Appl. Phys. Lett. **78**, 2309 (2001).
- [Mei01a] M. Meixner, R. Kunert, S. Bose, E. Schöll, V. A. Shchukin, D. Bimberg, E. Penev, and P. Kratzer: *Monte Carlo simulation of the self-organized growth of quantum dots with anisotropic surface diffusion*. In *Proc. 25th International Conference on the Physics of Semiconductors (ICPS-25), Osaka 2000*, edited by N. Miura and T. Ando, p. 381 (Springer, Berlin, 2001).
- [Mei01b] M. Meixner, E. Schöll, M. Schmidbauer, H. Raidt, and R. Köhler: *Formation of Island Chains in SiGe/Si Heteroepitaxy by Elastic Anisotropy – A Monte Carlo Study*. Phys. Rev. B **64**, 245307 (2001).
- [Mei01c] M. Meixner, E. Schöll, V. A. Shchukin, and D. Bimberg: *Self-assembled quantum dots: Crossover from kinetically controlled to thermodynamically limited growth*. Phys. Rev. Lett. **87**, 236101 (2001). Ibid **88**, 059901 (2002).
- [Mei02a] M. Meixner: *Simulation of self-organized growth kinetics of quantum dots*. Ph.D. thesis, TU Berlin (2002).

- [Mei02b] M. Meixner, R. Kunert, E. Schöll, V. A. Shchukin, and D. Bimberg: *Monte-Carlo simulation of self-organized quantum dot structures: crossover from kinetics to thermodynamics*. In *Proceedings of the 10<sup>th</sup> International Symposium on Nanostructures: Physics and Technology*, p. 12 (Ioffe Institute, St. Petersburg, 2002).
- [Mei03a] M. Meixner, R. Kunert, and E. Schöll: *Control of strain-mediated growth kinetics of self-assembled semiconductor quantum dots*. *Phys. Rev. B* **67**, 195301 (2003).
- [Mei03b] M. Meixner and E. Schöll: *Kinetically enhanced correlation and anticorrelation effects in self-organized quantum dot stacks*. *Phys. Rev. B* **67**, 121202 (2003).
- [Mic04] T. Michely and J. Krug: *Islands, Mounds and Atoms* (Springer, Berlin, 2004), 1 edn.
- [Mo90] Y.-W. Mo, D. E. Savage, B. S. Swartzentruber, and M. G. Lagally: *Kinetic pathway in Stranski-Krastanov growth of Ge on Si(001)*. *Phys. Rev. Lett.* **65**, 1020 (1990).
- [Moi94] J. M. Moison, F. Houzay, F. Barthe, L. Leprince, E. André, and O. Vatel: *Self-organized growth of regular nanometer-scale InAs dots on GaAs*. *Appl. Phys. Lett.* **64**, 196 (1994).
- [Mon01] F. Montalenti and A. F. Voter: *Normal-incidence steering effect in crystal growth: Ag/Ag(100)*. *Phys. Rev. B* **64**, 081401(R) (2001).
- [Moo96] R. L. Moon: *MOVPE: is there any other technology for optoelectronics?* *J. Crystal Growth* **170**, 1 (1996).
- [Mul96a] P. A. Mulheran and J. A. Blackman: *Capture zones and scaling in homogeneous thin-film growth*. *Phys. Rev. B* **53**, 10261 (1996).
- [Mül96b] P. Müller and R. Kern: *The physical origin of the two-dimensional towards three-dimensional coherent epitaxial Stranski-Krastanov transition*. *Appl. Surf. Sci.* **102**, 6 (1996).
- [New99] M. E. J. Newman and T. Barkema: *Monte Carlo Methods in Statistical Physics* (Oxford University Press, Oxford, 1999).
- [Nur01] L. Nurminen, A. Kuronen, and K. Kaski: *Kinetic Monte Carlo simulation of nucleation on patterned substrates*. *Phys. Rev. B* **63**, 035407 (2001).
- [Nöt94] R. Nötzel, J. Temmyo, and T. Tamamura: *Self-organized growth of strained InGaAs quantum disks*. *Nature* **368**, 131 (1994).
- [Ohn99] K. Ohno, K. Esfarjani, and Y. Kawazoe: *Computational Materials Science* (Springer, 1999).
- [Par94] R. G. Parr and W. Yang: *Density-functional theory of atoms and molecules* (Oxford University Press, 1994).

- [Pat03] F. Patella, S. Nufri, F. Arciprete, M. Fanfoni, E. Placidi, A. Sgarlata, and A. Balzarotti: *Tracing the two- to three-dimensional transition in the InAs/GaAs(001) heteroepitaxial growth*. Phys. Rev. B **67**, 205308 (2003).
- [Pen01] E. Penev, P. Kratzer, and M. Scheffler: *Effect of strain on surface diffusion in semiconductor heteroepitaxy*. Phys. Rev. B **64**, 085401 (2001).
- [Pen02] E. Penev: *On the Theory of Surface Diffusion in InAs/GaAs(001) Heteroepitaxy*. Ph.D. thesis, TU Berlin (2002).
- [Pim98] A. Pimpinelli and J. Villain: *Physics of Crystal Growth* (Cambridge University Press, Cambridge, 1998).
- [Pop99] J. A. Pople: *Nobel Lecture: Quantum chemical models*. Rev. Mod. Phys. **71**, 1267 (1999).
- [Por77] K. Portz and A. A. Maradudin: *Surface contribution on the low-temperature specific heat of a cubic crystal*. Phys. Rev. B **16**, 3535 (1977).
- [Pre92] W. H. Press, B. P. Flannery, S. A. Teukolsky, and W. T. Vetterling: *Numerical Recipes in C (2nd ed.)* (Cambridge University Press, Cambridge, 1992).
- [Pri95] C. Priester and M. Lannoo: *Origin of Self-Assembled Quantum Dots in Highly Mismatched Heteroepitaxy*. Phys. Rev. Lett. **75**, 93 (1995).
- [Pri01] C. Priester: *Modified two-dimensional to three-dimensional growth transition process in multistacked self-organized quantum dots*. Phys. Rev. B **63**, 153303 (2001).
- [Pry98] C. Pryor, J. Kim, L. W. Wang, A. J. Williamson, and A. Zunger: *Comparison of two methods for describing the strain profiles in quantum dots*. J. Appl. Phys. **83**, 2548 (1998).
- [Raa03] A. Raab, R. T. Lechner, and G. Springholz: *Growth temperature and coverage dependence of vertical and lateral ordering in self-assembled PbSe quantum-dot superlattices*. Phys. Rev. B **67**, 165321 (2003).
- [Ras01] A. Rastelli, M. Kummer, and H. von Känel: *Reversible Shape Evolution of Ge Islands on Si(001)*. Phys. Rev. Lett. **87**, 256101 (2001).
- [Rat94] C. Ratsch, A. Zangwill, and P. Šmilauer: *Scaling of Heteroepitaxial Island Sizes*. Surf. Sci. Lett. **314**, L937 (1994).
- [Rat97] C. Ratsch, A. P. Seitsonen, and M. Scheffler: *Strain dependence of surface diffusion: Ag(111) and Pt(111)*. Phys. Rev. B **55**, 6750 (1997).
- [Reg05] B. C. Regan, S. Aloni, K. Jensen, R. O. Ritchie, and A. Zettl: *Nanocrystal-Powered Nanomotor*. Nano Lett. **5**, 1730 (2005).
- [Rei04] S. Reich, C. Thomsen, and J. Maultzsch: *Carbon Nanotubes: Basic Concepts and Physical Principles* (Wiley-VCH, Weinheim, 2004).

- [Rob02] S. W. Robey: *Kinetic instabilities during plasma etching of GaAs(001)*. Phys. Rev. B **65**, 115306 (2002).
- [Rug97] P. Ruggerone, C. Ratsch, and M. Scheffler: *Density-Functional Theory of epitaxial growth of metals*. In *The Chemical Physics of Solid Surfaces*, vol. 8, p. 490 (Elsevier, Amsterdam, 1997).
- [Saa74] A. S. Saada: *Elasticity - Theory and applications* (Pergamon, New York, 1974).
- [Sch66] R. L. Schwoebel and E. J. Shipsey: *Step motion on crystal surfaces*. J. Appl. Phys. **37**, 3682 (1966).
- [Sch95] M. Schroeder and D. E. Wolf: *Magic islands and submonolayer scaling in molecular beam epitaxy*. Phys. Rev. Lett. **74**, 2062 (1995).
- [Sch97] M. Schroeder and D. E. Wolf: *Diffusion on strained surfaces*. Surf. Sci. **375**, 129 (1997).
- [Sch98a] M. Schmidbauer, T. Wiebach, H. Raidt, M. Hanke, R. Köhler, and H. Wawra: *Ordering of self-assembled  $Si_{1-x}Ge_x$  islands studied by grazing incidence small-angle x-ray scattering and atomic force microscopy*. Phys. Rev. B **58**, 10523 (1998).
- [Sch98b] E. Schöll and S. Bose: *Kinetic Monte Carlo Simulation of the Nucleation Stage of the Self-organized Growth of Quantum Dots*. Sol. State El. **42**, 1587 (1998).
- [Sch01] E. Schöll: *Nonlinear spatio-temporal dynamics and chaos in semiconductors* (Cambridge University Press, Cambridge, 2001). Nonlinear Science Series, Vol. 10.
- [Ser04] R. F. Service: *Nanotoxicology: Nanotechnology Grows Up*. Science **304**, 1732 (2004).
- [Shc95a] V. A. Shchukin, A. J. Borovkov, N. N. Ledentsov, and D. Bimberg: *Tuning and breakdown of faceting under externally applied stress*. Phys. Rev. B **51**, 10104 (1995).
- [Shc95b] V. A. Shchukin, N. N. Ledentsov, P. S. Kop'ev, and D. Bimberg: *Spontaneous ordering of arrays of coherent strained islands*. Phys. Rev. Lett. **75**, 2968 (1995).
- [Shc98a] V. A. Shchukin and D. Bimberg: *Strain-driven self-organisation of nanostructures on semiconductor surfaces*. Appl. Phys. A **67**, 687 (1998).
- [Shc98b] V. A. Shchukin, D. Bimberg, V. G. Malyshkin, and N. N. Ledentsov: *Vertical correlations and anticorrelations in multisheet arrays of two-dimensional islands*. Phys. Rev. B **57**, 12262 (1998).
- [Shc99a] V. Shchukin and D. Bimberg: *Spontaneous ordering of nanostructures on crystal surfaces*. Rev. Mod. Phys. **71**, 1125 (1999).

- [Shc99b] V. A. Shchukin: *Green's tensor in elastically anisotropic cubic crystals*. Private communication (1999).
- [Shc03] V. A. Shchukin and J. Tersoff: *Strain-dependent chemical potential*. private communication (2003).
- [Shc04] V. A. Shchukin, N. N. Ledentsov, and D. Bimberg: *Epitaxy of Nanostructures* (Springer, Berlin, 2004).
- [Shi92] T. Shitara, D. D. Vvedensky, M. R. Wilby, J. Zhang, J. H. Neave, and B. A. Joyce: *Step-density variations and reflection high-energy electron-diffraction intensity oscillations during epitaxial growth on vicinal GaAs(001)*. Phys. Rev. B **46**, 6815 (1992).
- [Shi96] L. E. Shilkrot and D. J. Srolovitz: *Adatom-step interactions: Atomistic simulations and elastic models*. Phys. Rev. B **55**, 4737 (1996).
- [Shi01] A. J. Shields, M. P. O'Sullivan, I. Farrer, D. A. Ritchie, M. L. Leadbeater, N. K. Patel, R. A. Hogg, C. E. Norman, N. J. Curson, and M. Pepper: *Single Photon Detection with a Quantum Dot Transistor*. Jpn. J. Appl. Phys. **40**, 2058 (2001).
- [Shi05a] F. Shi, Y. Shim, and J. G. Amar: *Island-size distribution and capture numbers in three-dimensional nucleation: Comparison with mean-field behavior*. Phys. Rev. B **71**, 245411 (2005).
- [Shi05b] Y. Shim and J. G. Amar: *Rigorous synchronous relaxation algorithm for parallel kinetic Monte Carlo simulations of thin film growth*. Phys. Rev. B **71**, 115436 (2005).
- [Shi05c] Y. Shirai, A. J. Osgood, Y. Zhao, K. F. Kelly, and J. M. Tour: *Directional Control in Thermally Driven Single-Molecule Nanocars*. Nano Lett. **5**, 2330 (2005).
- [Šmi93] P. Šmilauer and D. Vvedensky: *Step-edge barriers on GaAs(001)*. Phys. Rev. B **48**, 17603 (1993).
- [Šmi99] P. Šmilauer, M. Rost, and J. Krug: *Fast coarsening in unstable epitaxy with desorption*. Phys. Rev. E **59**, R6263 (1999).
- [Spr00] G. Springholz, M. Pinczolits, P. Mayer, V. Holy, G. Bauer, H. Kang, and L. Salamanca-Riba: *Tuning of Vertical and Lateral Correlations in Self-Organized PbSe/Pb<sub>1-x</sub>Eu<sub>x</sub>Te Quantum Dot Superlattices*. Phys. Rev. Lett. **84**, 4669 (2000).
- [Sta04] J. Stangl, V. Holý, and G. Bauer: *Structural properties of self-organized semiconductor nanostructures*. Rev. Mod. Phys. **76**, 725 (2004).
- [Sta05] C. Stampfl and A. J. Freeman: *Stable and metastable structures of the multiphase tantalum nitride system*. Phys. Rev. B **71**, 024111 (2005).

- [Ste96] E. Steimetz, J.-T. Zettler, F. Schienle, T. Trepk, T. Wethkamp, W. Richter, and I. Sieber: *In-situ Monitoring of InAs-on-GaAs Quantum Dot Formation in MOVPE by Reflectance-Anisotropy-Spectroscopy and Ellipsometry*. Appl. Surf. Science **107**, 203 (1996).
- [Ste06] G. Stegemann: *Noise-induced Dynamics in the Double Barrier Resonant Tunneling Diode*. Ph.D. thesis, Technische Universität Berlin (2006).
- [Sto99] H. L. Stormer: *Nobel Lecture: The fractional quantum Hall effect*. Rev. Mod. Phys. **71**, 875 (1999).
- [Str39] I. N. Stranski and L. Krastanow: *Sitzungsberichte der Akademie der Wissenschaften in Wien*. Akad. Wiss. Lit. Mainz Math.-Natur. Kl. IIb **146**, 797 (1939).
- [Tei96] C. Teichert, M. G. Lagally, L. J. Peticolas, J. C. Bean, and J. Tersoff: *Stress-induced self-organization of nanoscale structures in SiGe/Si multilayer films*. Phys. Rev. B **53**, 16334 (1996).
- [Ter96] J. Tersoff, C. Teichert, and M. G. Lagally: *Self-Organization in Growth of Quantum Dot Superlattices*. Phys. Rev. Lett. **76**, 1675 (1996).
- [Tsa99] A. F. Tsatsulnikov, B. V. Volovik, N. N. Ledentsov, M. V. Maximov, A. Y. Egorov, A. R. Kovsh, V. M. Ustinov, A. E. Zhukov, P. S. Kop'ev, Z. I. Alferov, I. A. Kozin, M. V. Belousov, I. P. Soshnikov, P. Werner, D. Litvinov, U. Fischer, A. Rosenauer, and D. Gerthsen: *Lasing in structures with InAs quantum dots in an (Al,Ga)As matrix grown by submonolayer deposition*. J. Electron. Mat. **28**, 537 (1999).
- [Tsu82] D. C. Tsui, H. L. Stormer, and A. C. Gossard: *Two-Dimensional Magnetotransport in the Extreme Quantum Limit*. Phys. Rev. Lett. **48**, 1559 (1982).
- [Usa00] N. Usami, Y. Araki, Y. Ito, M. Miura, and Y. Shiraki: *Modification of the growth mode of Ge on Si by buried Ge islands*. Appl. Phys. Lett. **76**, 3723 (2000).
- [Ven84] J. A. Venables, G. D. Spiller, and M. Hanbücken: *Nucleation and growth of thin films*. Rep. Prog. Phys. **47**, 399 (1984).
- [Vil91] J. Villain: *Continuum models of crystal growth from atomic beams with and without desorption*. J. Phys. I **1**, 19 (1991).
- [Vol26] M. Volmer and A. Weber: *Novel growth mechanism in heteroepitaxial semiconductor growth*. Z. Phys. Chem. **119**, 277 (1926).
- [Vot02] A. F. Voter, F. Montalenti, and T. C. Germann: *Extending the time scale in atomistic simulation of materials*. Annu. Rev. Mat. Res. **32**, 321 (2002).
- [Vve00] D. D. Vvedensky: *Scaling functions for island-size distributions*. Phys. Rev. B **62**, 15435 (2000).
- [Wan99a] L. G. Wang, P. Kratzer, and M. Scheffler: *Size, shape and stability of InAs quantum dots on the GaAs(001) substrate*. Phys. Rev. Lett. **82** (1999). Submitted.

- [Wan99b] L. G. Wang, P. Kratzer, M. Scheffler, and N. Moll: *Formation and stability of self-assembled coherent islands in highly mismatched heteroepitaxy*. Phys. Rev. Lett. **82**, 4042 (1999).
- [Wan00] L. G. Wang, P. Kratzer, N. Moll, and M. Scheffler: *Size, shape, and stability of InAs quantum dots on the GaAs(001) substrate*. Phys. Rev. B **62**, 1897 (2000).
- [Wan04] X.-D. Wang, N. Liu, C. K. Shih, S. Govindaraju, and A. L. Holmes, Jr.: *Spatial correlation-anticorrelation in strain-driven self-assembled InGaAs quantum dots*. Appl. Phys. Lett. **85**, 1356 (2004).
- [Xie95] Q. Xie, A. Madhukar, P. Chen, and N. P. Kobayashi: *Vertically self-Organized InAs Quantum Box Islands on GaAs(100)*. Phys. Rev. Lett. **75**, 2542 (1995).
- [Xu05] M. C. Xu, Y. Temko, T. Suzuki, and K. Jacobi: *Shape transition of InAs quantum dots on GaAs(001)*. J. Appl. Phys. **98**, 083525 (2005).
- [Yus97] G. Yusa and H. Sakaki: *Trapping of photogenerated carriers by InAs quantum dots and persistent photoconductivity in novel GaAs/n-AlGaAs field-effect transistor*. Appl. Phys. Lett. **70**, 345 (1997).
- [Zyw99] T. K. Zywiec, J. Neugebauer, and M. Scheffler: *The adsorption of oxygen at GaN surfaces*. Appl. Phys. Lett. **74**, 1695 (1999).